3-2021

Safe Spacecraft Rendezvous and Proximity Operations via Reachability Analysis

Paul A. Grossi

Safe Spacecraft Rendezvous and Proximity Operations via Reachability Analysis

THESIS

Paul A. Grossi, Captain, USSF

AFIT-ENY-MS-21-M-302

DEPARTMENT OF THE AIR FORCE
AIR UNIVERSITY

AIR FORCE INSTITUTE OF TECHNOLOGY

Wright-Patterson Air Force Base, Ohio

AFIT-ENY-MS-21-M-302

SAFE SPACECRAFT RENDEZVOUS AND PROXIMITY OPERATIONS VIA REACHABILITY ANALYSIS

THESIS

Presented to the Faculty

Department of Aeronautics & Astronautics

Graduate School of Engineering and Management

Air Force Institute of Technology

Air University

Air Education and Training Command

in Partial Fulfillment of the Requirements for the

Degree of Master of Aeronautical Engineering

Paul A. Grossi, BS, Mechanical Engineering

Captain, USSF

March 25, 2021

AFIT-ENY-MS-21-M-302

SAFE SPACECRAFT RENDEZVOUS AND PROXIMITY OPERATIONS VIA REACHABILITY ANALYSIS

THESIS

Paul A. Grossi, BS, Mechanical Engineering
Captain, USSF

Committee Membership:

Major Costantinos Zagaris, PhD
Chair

Lieutenant Colonel Kirk Johnson, PhD
Member

Major Joshuah Hess, PhD
Member

Adedeji B. Badiru, PhD
Dean, Graduate School of Engineering and Management

Abstract

The rapid expansion of the utilization of space by nations and industry has presented new challenges and opportunities to operate efficiently and responsibly. Many current and future operations require precise and safe rendezvous and proximity operations (RPO) with a guarantee of the feasibility of the rendezvous maneuver. Reachability analysis is the process of computing the set of states that can be reached given all admissible controls and can be a valuable component in an autonomous mission planning system if conducted efficiently. In the current research, reachability analysis is used with several relative motion models to show that all ranges of orbits can be computed in milliseconds, and that it is a feasible approach for on-board autonomous mission planning. Reachability analysis is then combined with an Artificial Potential Function (APF) derived guidance control law to conduct safe spacecraft rendezvous between a deputy in a Natural Motion Circumnavigation (NMC) relative orbit around a chief while avoiding obstacles. While the APF employed in this research requires improvements for trajectory computation, this research demonstrates the feasibility of combining reachability analysis with an APF for safe, on-board, autonomous mission planning.

To my grandparents, whose kindness, generosity, and laughter live on.

Acknowledgements

I would foremost like to express my gratitude to my advisor, Major Costantinos Zagaris for your support and guidance throughout the entire process and as my research goals evolved considerably along the way. I would also like to thank Major Joshuah Hess for his enthusiastic love for all RPO related topics. Your dedication and willingness to join our video calls at midnight on Saturdays to offer help with our work goes above and beyond. My appreciation extends as well to Lt Col Kirk Johnson for serving on my committee and providing valuable insights to refine this research.

I owe much of my affinity for engineering to Mr. K, mentor and friend, who has shown me from a young age how any problem can be tackled with a bit of resourcefulness, ingenuity, duct tape, and perseverance. Thank you to my "quaranteam" who helped keep me relatively sane through a pandemic and Master's program.

Of course, thank you to Mom, Dad, and my brothers, whose love and support is endless and energizing. Lastly, to my wife, for always believing in me and never giving up on encouraging me, and to my cats and dog for always keeping me company as I worked late into the night.

Paul A. Grossi

Table of Contents

Page

List of Figures

List of Tables

SAFE SPACECRAFT RENDEZVOUS AND PROXIMITY OPERATIONS VIA REACHABILITY ANALYSIS

I. Introduction

1.1 Motivation and Background

Spaceflight has long relied on spacecraft rendezvous and proximity operations (RPO) to perform docking, servicing, and inspection between spacecraft [4, 5]. Missions are being executed in increasingly complex, congested, and competitive environments. Mission planning for RPO requires the system to know information about its current states, operational constraints, and destination (final condition). Spacecraft have limited maneuverability based on orbit, available fuel, control thrusters, mission requirements, and required or available time to maneuver. Conventionally, human-in-the-loop mission planning consists of calculating and validating a required maneuver while considering all the applicable mission constraints [6]. For systems commanded and controlled from planners on the ground, the newly planned mission is then transmitted to the spacecraft to be performed in an open loop system. For manned missions, the maneuver is carried out manually. Although the Russian Space Agency developed an automated rendezvous and docking capability early on, the United States did not have this capability even through the Space Shuttle missions. At least as late as 1998, NASA did not have a serious program in progress to develop automated rendezvous capability [6]. In the space environment of the preceding decades, where orbits were less congested, large maneuvering operations were less prominent because spacecraft were parked in their mission orbits that were simple to

maintain throughout their lifecycle.

Increased maneuverability, along with evolving strategies for operating in space, are enabling the transferring of spacecraft between orbits [7, 5], performing rendezvous operations, performing inspection missions within a certain proximity of the inspected spacecraft, avoiding conjunctions with other spacecraft or debris, or refueling vehicles that would otherwise be nearing end-of-life due to lack of available fuel [8, 9]. Today's congested and dynamic environment is driving the need for autonomous mission planning and execution with cooperative (i.e. stabilized), noncooperative (i.e. nonstabilized), and uncooperative (i.e. evasive) targets [6].

1.2 Problem Statement

This research implements a system to drive a deputy spacecraft from an initial condition to rendezvous with a chief spacecraft while safely navigating around obstacles or keep-out zones (KOZ) to be adaptable as a safe, on-board, autonomous controller. On-board, autonomous rendezvous operations require knowledge of the physical space surrounding the spacecraft, a target state, and a controller to navigate the spacecraft from its current state to the target state while avoiding all non-permissible states. In a dynamic environment where all variables are not necessarily controllable or known, such as spacecraft in orbit, a spacecraft may have sensors to search its surrounding area for obstacles it must avoid. The safety aspect of the methodology developed in this research refers to collision and KOZ avoidance.

Given control limitations, disturbances, and a deterministic period of time, it is logical that a spacecraft can only reach a certain set of states from its current state, known as a "reach set". Reachability analysis is used to calculate such a reach set. Reachability analysis is useful in spacecraft mission planning as a means to verify the target positions can be reached within the required mission limits, such as

maneuvering time or fuel consumption [10]. In this research, reachability analysis is used to eliminate an assumption that all obstacles and KOZs are known *a priori* and must be discovered in real time. The reach set computed is useful for determining how far spacecraft sensors must look to identify obstacles. Only obstacles detected within the reach set *a posteriori* are activated in the guidance planning computation. The reach set calculation also provides a method to verify that the planned trajectory is feasible. For these benefits to be trustworthy and valid, a degree of confidence in the accuracy of the reach set must be established depending on the method used to calculate the reach set. As such, several relative motion dynamics models are tested with reachability analysis and analyzed for validity.

While the reach set identifies the nearest obstacles and feasible future states, an artificial potential function (APF) is utilized to calculate the control required for the rendezvous mission. An attractive APF is designed as a paraboloid with the global minimum residing at the target location, in this case the chief spacecraft. A repulsive APF is used for the obstacles, where a large spike located at each obstacle is intended to drive the spacecraft away from that location. The combined attractive and repulsive APF drives the deputy towards the rendezvous location at the global minimum while avoiding the known obstacles.

1.2.1 Research Questions

The following questions are posed in this research to address the problem statement:

1. How do relative motion models impact the reach set solution?

2. How can reachability analysis be utilized to support safe, on-board, autonomous mission planning?

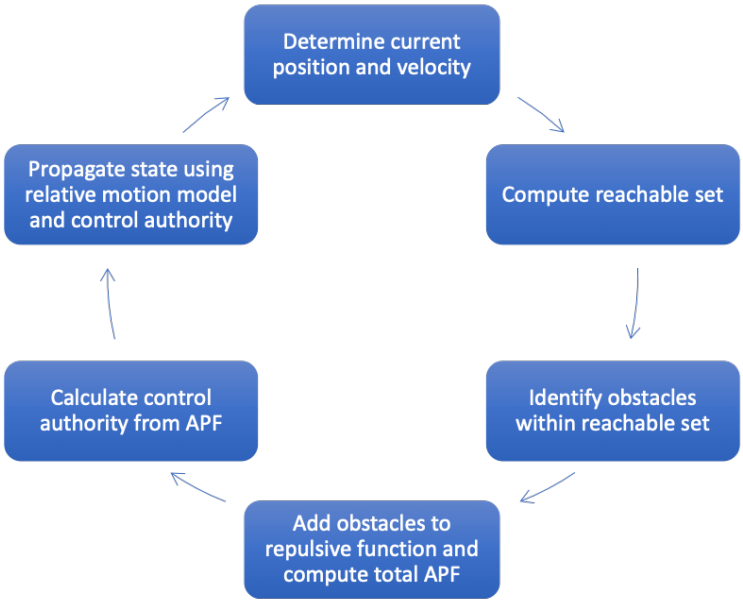

Figure 1.1. Flow chart of guidance methodology

3. Is the speed of detecting obstacles *a posteriori* with reachability analysis viable to support mission planning while considering obstacle and KOZ avoidance?

1.2.2 Research Scope and Assumptions

The following tasks are defined to support achieving the research objectives:

1. Conduct a survey of relative motion models comparing reach sets.
2. Implement reachability analysis and identify nearest obstacles.
3. Formulate APF to achieve guidance algorithm.

The first task aims at identifying the impact various relative motion models have on the reach set solution. Reachability analysis is conducted and compared across a range of orbits for several relative motion models. The second task implements a methodology for ensuring safe autonomous guidance in the presence of obstacles or keep-out zones. This helps define the APF in the third task which is used, in this research, for guiding a deputy spacecraft to rendezvous with a chief spacecraft.

The main assumptions that apply in this research are:

1. Unless otherwise noted, the orbital motion of the chief and deputy spacecraft and obstacles are defined as Keplerian restricted two-body motion, whereby they are modeled as point masses and perturbing forces and torques are ignored.

2. The deputy spacecraft has complete knowledge of its relative state, the chief's orbit, and the size and states of identified obstacles.

3. The deputy's relative orbital motion is modeled with linear relative motion models with assumptions unique to each model, as described in Sections 2.1.5 through 2.1.8.

4. The reach sets are ellipsoidal in 3-D subspace.

Additional assumptions apply to specific parts of this research and are detailed in later sections, as appropriate.

1.3 Organization of the Thesis

This thesis investigates methods for enabling on-board, autonomous rendezvous and proximity operations (RPO) with collision avoidance techniques for maneuvering spacecraft. This chapter has introduced the research motivation, some background on various RPO methods, and defines the research hypothesis. Chapter II presents a survey of literature on spacecraft relative motion models, methods for conducting reachability analysis, and artificial potential functions. Chapter III details the development of the reachability analysis method used, how the reach sets of various relative motion models will be compared, the development of the APF, and how the reach set and the APF are integrated to create a controller capable of collision avoidance and guidance. Chapter IV presents the results of the principles from Chapter III

applied to a spacecraft maneuvering and rendezvousing with another spacecraft with collision avoidance measures employed. Conclusions on the accuracy and viability of this method are discussed in Chapter V.

Math notation in this research utilizes bold text for vectors and matrices, and non-bolded variables are scalars. Dot notation above a variable represents time derivatives.

II. Literature Review

Limited on-board computational power of spacecraft necessitates efficient, accurate, and safe computational techniques. Automated spacecraft RPO will need to balance the precision of a computationally expensive exact relative motion model with the speed and efficiency offered by simpler, linearized relative motion models that have limitations to their range of applicability. This chapter details the existing relevant literature on various approaches to autonomous spacecraft RPO and maneuvering. The concluding sections of this chapter explain the various applications of the foundational concepts utilized in this research: reachability analysis and artificial potential functions.

2.1 Spacecraft Relative Motion Models

2.1.1 Reference Frames

Orbital characteristics can be defined by several different coordinate systems. Alfriend, et al. [11] provide definitions for the following inertial and relative coordinate systems often relevant in orbital mechanics. Inertial reference frames are useful for an object's position and velocity. A heliocentric coordinate system is an inertial reference frame centered at the Sun and may be useful in defining the Earth's position in its orbit or compared to other bodies orbiting the Sun. The $\hat{x}$ unit vector is positioned from the center of the Sun along the vernal equinox, which is the date that marks the first day of spring where daytime and nighttime are the same length. Celestially, this is where the Sun crosses the equatorial plane of the Earth moving northward. The $\hat{z}$ unit vector is defined normal to the ecliptic plane, which is the mean plane made by the Earth's orbit around the Sun, and points towards celestial north. The $\hat{y}$ unit vector is positioned to complete the right-handed coordinate system. Shown

in Figure 2.1, the Earth-Centered Inertial (ECI), or geocentric coordinate system, is an inertial reference frame often used when describing the position of a spacecraft. The ECI reference frame also defines the $\hat{x}$ unit vector along the vernal equinox. The $\hat{z}$ unit vector is defined normal to the Earth's equatorial plane pointing towards the geographic north pole. The $\hat{y}$ unit vector is positioned to complete the right-handed coordinate system. The ECI reference frame is the foundation of the orbital regimes studied in this research.

A relative reference frame is convenient when defining the motion of a spacecraft with respect to another spacecraft. This research employs a local-vertical, local-horizontal (LVLH) relative reference frame which is centered at a defined spacecraft and rotates with the spacecraft's orbital motion shown in Figure 2.2. This relative reference frame is also referred to as the relative Hill frame [12]. The spacecraft used to define center of the reference frame is called the chief. The $\hat{x}$ unit vector is positioned radially outward from center of the Earth through the chief and is aptly referred to as the radial direction. The $\hat{z}$ unit vector is perpendicular to the fundamental plane of the chief's orbit where the positive direction is the instantaneous angular momentum vector, and is referred to as the cross-track direction. The $\hat{y}$ unit vector is positioned to complete the right-handed coordinate system, and is referred to as the in-track direction. Other spacecraft in proximity to the chief and defined in the relative Hill frame are called deputies in this research.

Accurately describing the motion of a spacecraft can be a challenging endeavour. The Nonlinear Equations of Relative Motion (NERMs), about to be described in Sections 2.1.2 and 2.1.3 from Alfriend, et al. [11, 13], are a 10-dimensional system of nonlinear differential equations typically solved with numerical integration.

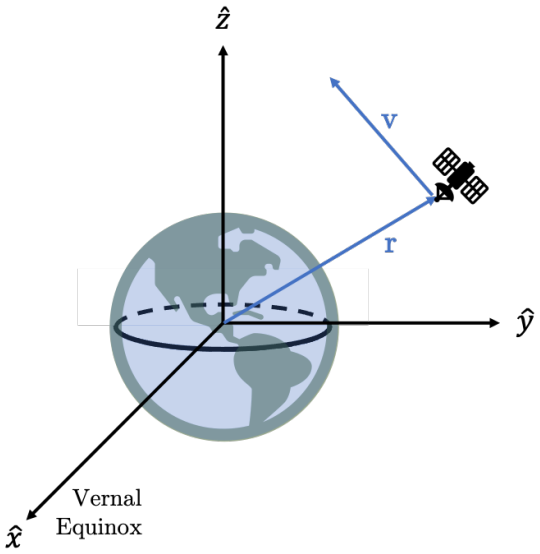

Figure 2.1. Earth-Centered Inertial (ECI) reference frame with position r and velocity v vectors shown

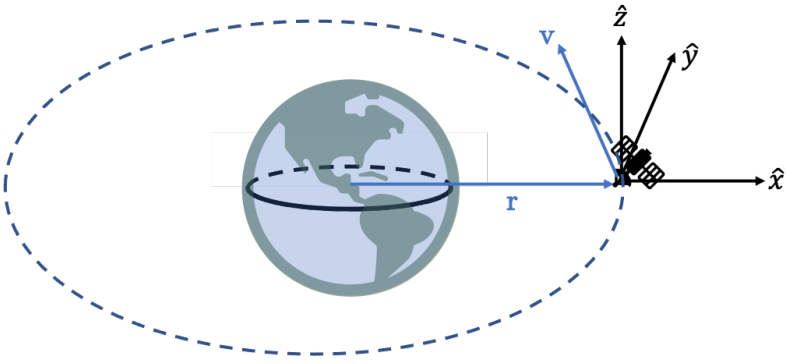

Figure 2.2. Local-Vertical, Local-Horizontal (LVLH) reference frame with position r and velocity v vectors shown

2.1.2 The Keplerian Two-Body Problem

The Keplerian two-body problem describes the effect of the gravitational forces two bodies exert on each other. This system is also known as the restricted two-body problem because the shape of the bodies are neglected such that no gravitational torques are imposed on the bodies by the inter-gravitational forces. Several assumptions apply to this system [11]:

1. Gravity is the only force, internal or external, exerted on the bodies.
2. Both bodies are spherical or point masses.
3. The orbiting body's mass (m) is much smaller compared to the primary body's mass (M).
4. Gravitational forces are Newtonian, thus directly proportional to the masses of the objects and inversely proportional to the square of the distance between the objects.

From these assumptions, the Keplerian two-body inertial equations of motion for a spacecraft are

$$\ddot{\boldsymbol{r}} + \frac{\mu}{r^3}\boldsymbol{r} = 0 \tag{2.1}$$

where

$$\mu = G(M + m) \tag{2.2}$$

and $\boldsymbol{r}$ is the position vector of the objects in the inertial reference frame.

From the third assumption above, the mass of the spacecraft is negligible, thus Equation 2.2 is reduced to Earth's gravitational constant (G) multiplied by Earth's mass (M) to produce Earth's gravitational parameter, $\mu = 398600.4418$ km^3/s^2. The

magnitude of the position vector, or orbital radius r, is defined by the classical orbital elements (COE) in Equations 2.3 and 2.4, respectively, where a is the semi-major axis of the orbit, e is the eccentricity, and ν is the true anomaly. The subscript c refers to the chief spacecraft and the subscript d refers to the deputy spacecraft.

$$r_c = ||\boldsymbol{r}_c|| = \frac{a_c(1-e_c^2)}{1+e_c\cos\nu_c} \tag{2.3}$$

$$r_d = ||\boldsymbol{r}_d|| = \frac{a_d(1-e_d^2)}{1+e_d\cos\nu_d} \tag{2.4}$$

2.1.3 Relative Orbital Dynamics

Describing relative orbits may be more useful and intuitive than trying to interpret inertial orbit parameters. Defining the relative position between spacecraft is as simple as taking the difference of the inertial position vectors from Equations 2.3 and 2.4

$$\boldsymbol{\rho} = \boldsymbol{r}_d - \boldsymbol{r}_c \ . \tag{2.5}$$

With the orbital position vectors of the chief ($\boldsymbol{r}_c$) and deputy ($\boldsymbol{r}_d$) being defined in the inertial frame, the relative acceleration can be calculated by directly differentiating the inertial position vectors twice and expanded with the inertial equations of motion from Equation 2.1 to produce

$$\begin{aligned} \ddot{\boldsymbol{\rho}} &= \ddot{\boldsymbol{r}}_d - \ddot{\boldsymbol{r}}_c \\ &= -\frac{\mu}{r_d^3}\boldsymbol{r_d} + \frac{\mu}{r_c^3}\boldsymbol{r_c} \\ &= -\frac{\mu}{||\boldsymbol{r}_c+\boldsymbol{\rho}||^3}(\boldsymbol{r}_c+\boldsymbol{\rho}) + \frac{\mu}{r_c^3}\boldsymbol{r_c} \ . \end{aligned} \tag{2.6}$$

These inertial equations of motion, expressed in the ECI reference frame, provide

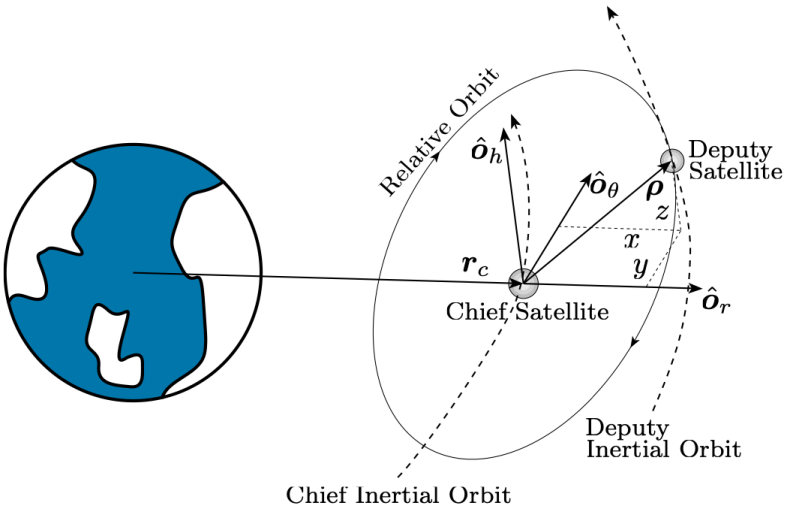

Figure 2.3. Parameterizations of chief and deputy inertial and relative orbits [1]

limited usefulness when analyzing the relative motion of two bodies such as a deputy to a chief. Resolving Equation 2.6 in the relative Hill frame allow the calculation of the relative position and velocity of the deputy spacecraft with respect to the chief spacecraft throughout the entire orbit. The conversion from the ECI reference frame ($\mathcal{I}$) to the relative Hill frame ($\mathcal{L}$) requires a rotation matrix $[R^{\mathcal{LI}}]$ and the transport theorem.

Recall from Section 2.1.1, the radial $\hat{x}$ unit vector in the relative Hill frame ($\hat{\boldsymbol{o}}_r$ in Figure 2.3) is a positive vector from the center of the inertial reference frame to the chief spacecraft, the cross-track $\hat{z}$ unit vector in the relative Hill frame ($\hat{\boldsymbol{o}}_h$ in Figure 2.3) is in the direction of the instantaneous angular momentum, and the in-track $\hat{y}$ unit vector completes the right-handed orthonormal coordinate system ($\hat{\boldsymbol{o}}_\theta$ in Figure 2.3). Therefore, the rotation matrix $[R^{\mathcal{LI}}]$ can be built from Equation 2.7,

$$[R^{\mathcal{LI}}] = \begin{bmatrix} \hat{x} & \hat{y} & \hat{z} \end{bmatrix}^T \tag{2.7}$$

where

$$\hat{x} = \frac{\boldsymbol{r}_c}{||\boldsymbol{r}_c||} \qquad \hat{z} = \frac{\boldsymbol{h}_c}{||\boldsymbol{h}_c||} \qquad \hat{y} = \hat{z} \times \hat{x}$$

$$\boldsymbol{h}_c = \frac{\boldsymbol{r}_c \times \boldsymbol{v}_c}{||\boldsymbol{r}_c \times \boldsymbol{v}_c||} \ .$$

Therefore, the relative position vector of the deputy with respect to the chief resolved in the relative Hill frame is shown in Equation 2.8 where the pre-superscripts denote the coordinate frames for which each variable is resolved: $\mathcal{I}$ is the inertial reference frame and $\mathcal{L}$ is the relative Hill frame,

$$^{\mathcal{L}}\boldsymbol{\rho} = [R^{\mathcal{LI}}]\,^{\mathcal{I}}\boldsymbol{\rho} \ . \tag{2.8}$$

To obtain the relative acceleration, the inertial relative position $^{\mathcal{I}}\boldsymbol{\rho}$ is differentiated with respect to time twice while taking care to employ the transport theorem since it shall be expressed in the non-inertial relative Hill reference frame to obtain the relative acceleration represented in the inertial frame,

$$^{\mathcal{I}}\ddot{\boldsymbol{\rho}} = {}^{\mathcal{L}}\ddot{\boldsymbol{\rho}} + 2\boldsymbol{\omega}^{\mathcal{LI}} \times {}^{\mathcal{L}}\dot{\boldsymbol{\rho}} + \dot{\boldsymbol{\omega}}^{\mathcal{LI}} \times {}^{\mathcal{L}}\boldsymbol{\rho} + \boldsymbol{\omega}^{\mathcal{LI}} \times (\boldsymbol{\omega}^{\mathcal{LI}} \times {}^{\mathcal{L}}\boldsymbol{\rho}) \tag{2.9}$$

where

$$\boldsymbol{\omega}^{\mathcal{LI}} = \begin{bmatrix} 0 & 0 & \dot{\theta}_c \end{bmatrix}^T \qquad {}^{\mathcal{L}}\boldsymbol{\rho} = \begin{bmatrix} x & y & z \end{bmatrix}^T \ ,$$

$\boldsymbol{\omega}^{\mathcal{LI}}$ is the angular velocity vector of the relative Hill frame $\mathcal{L}$ relative to the ECI reference frame $\mathcal{I}$, $\dot{\theta}_c = \dot{\omega} + \dot{\nu}$ and is the argument of true latitude time rate of change, $\dot{\omega}$ is the time rate of change of the argument of perigee, $\dot{\nu}$ is the time rate of change of the true anomaly, and x, y, and z are the radial, in-track, and cross-track positions expressed in the relative Hill frame. The chief's relative position can be expressed in the relative Hill frame as

$$\boldsymbol{r}_c = \begin{bmatrix} r_c & 0 & 0 \end{bmatrix}^T \ . \tag{2.10}$$

Substituting Equation 2.6 into Equation 2.9 gives rise to of the 10-dimensional

nonlinear equations of relative motion, referred to as the NERMs.

$$\begin{aligned}
\ddot{x} - 2\dot{\theta}_c\dot{y} - \ddot{\theta}_c y - \dot{\theta}_c^2 x &= -\frac{\mu(r_c + x)}{r_d^3} + \frac{\mu}{r_c^2} + a_x \\
\ddot{y} - 2\dot{\theta}_c\dot{x} + \ddot{\theta}_c x - \dot{\theta}_c^2 y &= -\frac{\mu y}{r_d^3} + a_y \\
\ddot{z} &= -\frac{\mu z}{r_d^3} + a_z
\end{aligned} \tag{2.11}$$

where

$$\begin{aligned}
p_c &= a_c(1 - e_c^2) \\
\dot{r}_c &= \dot{\theta}_c \frac{p_c e_c \sin\theta_c}{(1 + e_c\cos\theta_c)^2} \\
\ddot{r}_c &= r_c \dot{\theta_c}^2 - \frac{\mu}{r_c^2} \\
\dot{\theta}_c &= \frac{\sqrt{\mu p_c}}{r_c^2} \\
\ddot{\theta}_c &= -\frac{2\dot{r}_c\dot{\theta}_c}{r_c} \\
r_d &= \sqrt{(r_c + x)^2 + y^2 + z^2}
\end{aligned}$$

The NERMs describe the exact relative motion of a deputy spacecraft with respect to a chief spacecraft for an unperturbed orbit. The terms a_x, a_y, and a_z are additional accelerations that can model control forces or disturbances.

2.1.4 Linearized Relative Equations of Motion

In the pursuit of advancing spacecraft maneuverability models, many models have been developed that offer degrees of efficiency and accuracy in predicting spacecraft position and velocity through its orbit. These models are linearized versions of the NERMs derived in Section 2.1.3 employing various assumptions with regard to orbital eccentricity, perturbations, and the dynamical state representation [14]. These models offer a simpler and computationally efficient way to propagate the relative motion dynamics compared to numerical integration of the NERMs [14].

Sullivan [14] provides a survey of spacecraft relative motion dynamics models and demonstrates the error produced by several linearized dynamics models for a variety of orbital setups. Among the dynamics models evaluated are Clohessy-Wiltshire (CW) [12], Schweighart-Sedwick (SS) [15], Yamanaka-Ankersen (YA) [16], and Gim-Alfriend (GA) [17]. Sullivan demonstrates the effects of eccentricity and perturbations on the orbital trajectory computed by each algorithm and provides a relative state error estimate compared to the nonlinear equations of relative motion.

The orbits studied by Sullivan are in low Earth orbit (LEO) with a 750 km altitude, with eccentricities varying from 0.0001 to 0.7, and with interspacecraft separation varying from 2 m to 250 km. LEO is chosen to demonstrate the influence J_2 perturbation has on each model's ability to accurately propagate the relative motion. Similarly, ranging the eccentricity from nearly circular (0.0001) to highly elliptical (0.7) adequately demonstrates each model's ability to accurately propagate the relative motion. The interspacecraft separation challenges each model's applicable linearization region based on its simplifying assumptions and relative motion state parameterization methodology. Depending on the parameterization methodology, many linearized relative motion models experience singularities based on the position, shape or applied time horizon. Sullivan's research shows some models can vary by orders of magnitude between each other and the truth model. It demonstrates the importance of understanding the orbital environment, the accuracy or precision requirements, and the duration for which the relative motion dynamics are being studied [14].

2.1.5 Clohessy-Wiltshire Relative Motion Model

The Clohessy-Wilshire (CW) relative motion model [12] is a set of first-order relative motion equations that has been broadly used for modeling spacecraft RPO

[14, 18]. The National Aeronautics and Space Administration (NASA) has demonstrated RPO stemming from the CW model with missions ranging from Gemini [19] to the Space Shuttle [20], and with its Automated Rendezvous and Capture (AR&C) capability development program that began around the early 2000s [21]. The CW model is valid for spacecraft operating in close-proximity about circular reference orbits and can be expressed in many forms, making it a flexible and often used model for modeling relative motion dynamics. The CW model is comprised of a set of ordinary differential equations (ODEs) that yield a closed-form solution. The closed-form solution can be expressed as a state transition matrix (STM), which is utilized for the computation in this research.

The main assumptions made by the CW model are: the chief reference orbit is circular, there are no perturbations on the orbital motion, and the orbital relative coordinates (i.e. the distances x, y, and z from the chief reference orbit expressed in the relative Hill frame) are small compared to the chief radius r_c. Applying these assumptions to the NERMs expressed in Equation 2.11, the forced relative motion dynamics are given in terms of x, y, and z in the relative Hill frame, the control or disturbance accelerations dynamics a_x, a_y, and a_z, and the mean motion n of the chief reference orbit, [12]

$$\begin{aligned} \ddot{x} &= 2n\dot{y} + 3n^2 x + a_x \\ \ddot{y} &= -2n\dot{x} + a_y \\ \ddot{z} &= -n^2 z + a_z \end{aligned} \tag{2.12}$$

where

$$n = \sqrt{\frac{\mu}{a_c^3}} \, . \tag{2.13}$$

For the unforced equations of motion, where there are no external forces on the deputy spacecraft, $a_x = a_y = a_z = 0$. It should be noted that the cross-track dynamics

(z) are decoupled from the radial (x) and in-track (y) dynamics. Non-zero cross-track motion is considered out-of-plane motion while zero cross-track motion is considered in-plane motion [22]. The unforced motion, closed-form solution is [12]

$$
\begin{aligned}
x(t) &= \left[4x_0 + \frac{2\dot{y}_0}{n}\right] + \frac{\dot{x}_0}{n}\sin(nt) - \left[3x_0 + \frac{2\dot{y}_0}{n}\right]\cos(nt) \\
y(t) &= \left(-\left[6nx_0 + 3\dot{y}_0\right]t + \left[y_0 - \frac{2\dot{x}_0}{n}\right]\right) + \left[6x_0 + \frac{4\dot{y}_0}{n}\right]\sin(nt) + \frac{2\dot{x}_0}{n}\cos(nt) \\
z(t) &= \frac{\dot{z}_0}{n}\sin(nt) + z_0\cos(nt) \\
\dot{x}(t) &= \dot{x}_0\cos nt + \left[3x_0 n + 2\dot{y}_0\right]\sin nt \\
\dot{y}(t) &= -\left[6nx_0 + 3\dot{y}_0\right] + \left[6x_0 n + 4\dot{y}_0\right]\cos nt - 2\dot{x}_0\sin nt \\
\dot{z}(t) &= \dot{z}_0\cos nt - z_0 n\sin nt\ .
\end{aligned}
\tag{2.14}
$$

The CW equations of motion in Equation 2.12 can be written in state-space representation as [23]

$$
\dot{\boldsymbol{x}} = \begin{bmatrix}
0 & 0 & 0 & 1 & 0 & 0 \\
0 & 0 & 0 & 0 & 1 & 0 \\
0 & 0 & 0 & 0 & 0 & 1 \\
3n^2 & 0 & 0 & 0 & 2n & 0 \\
0 & 0 & 0 & -2n & 0 & 0 \\
0 & 0 & -n^2 & 0 & 0 & 0
\end{bmatrix} \boldsymbol{x} \tag{2.15}
$$

where $\boldsymbol{x}$ is composed of the relative position and relative velocity components, $\boldsymbol{x} = [x\ y\ z\ \dot{x}\ \dot{y}\ \dot{z}]^T$.

The state transition matrix form propagates the unforced current relative position forward a predetermined time Δt [23],

$$\boldsymbol{x}(t) = \boldsymbol{\Phi}(\Delta t)\boldsymbol{x}(t_0),\ \boldsymbol{x} = [x\ y\ z\ \dot{x}\ \dot{y}\ \dot{z}]^T \tag{2.16}$$

where

$$\boldsymbol{\Phi}(t) = \begin{bmatrix} 4-3\cos nt & 0 & 0 & \frac{1}{n}\sin nt & \frac{2}{n}(1-\cos nt) & 0 \\ 6(\sin nt - nt) & 1 & 0 & \frac{2}{n}(\cos nt - 1) & \frac{1}{n}(4\sin nt - 3nt) & 0 \\ 0 & 0 & \cos nt & 0 & 0 & \frac{1}{n}\sin nt \\ 3n\sin nt & 0 & 0 & \cos nt & 2\sin nt & 0 \\ 6n(\cos nt - 1) & 0 & 0 & -2\sin nt & 4\cos nt - 3 & 0 \\ 0 & 0 & -n\sin nt & 0 & 0 & \cos nt \end{bmatrix}.$$

The efficiency and vast applicability of the CW equations offer a strong foundation for the development of mission planning tools or on-board guidance capabilities [9].

2.1.6 Schweighart-Sedwick Relative Motion Model

The Schweighart-Sedwick (SS) relative motion model is an extension of the CW model with the addition of the J_2 perturbative force [24], which is the force that accounts for the fact that the Earth is not perfectly spherical. Instead, the Earth is oblate, or flattened at the north and south poles [25]. The SS model is an effective and efficient system of linear, constant coefficient, differential equations that can be solved analytically to describe the relative motion of spacecraft [24] while incorporating the effects of J_2 perturbative force.

The governing assumptions applied to the derivation of the SS model are the use of the time averaged effect of the gradient of the J_2 potential, $\nabla \boldsymbol{J}_2 \boldsymbol{r}_{ref}$, for the in-track motion and mean variations in orbital elements for the cross-track motion [15]. Other assumptions employed are

- A constant radius reference orbit linearizes the gravitational terms with respect

to the reference orbit.

- Equal period of the chief and deputy orbits eliminates in-track secular drift.
- The normal component of the J_2 potential is solely responsible for drift in the right ascension of the ascending node (RAAN) which eliminates nodal drift.
- Within a cluster of spacecraft, there are small differences in RAAN for each spacecraft, therefore higher order terms describing the intersection of orbital planes can be omitted.
- The J_2 potential is symmetric at the equator, therefore the system is initialized t_0 when crossing the equator.

The SS ordinary differential equations of motion are [15]

$$\begin{aligned} \ddot{x} - 2(nc)\dot{y} - (5c^2 - 2)n^2 x &= -3n^2 J_2 \frac{R_e^2}{r_{ref}} \\ &\quad \times \left[\frac{1}{2} - \frac{3\sin^2(kt)}{2} - \frac{1 + 3\cos(2i_{ref})}{8}\right] \\ \ddot{y} + 2(nc)\dot{x} &= -3n^2 J_2 \frac{R_e^2}{r_{ref}} \sin^2(i_{ref}) \sin(kt)\cos(kt) \\ \ddot{z} + q^2 z &= 2lq\cos(qt + \phi) \end{aligned} \tag{2.17}$$

where s, c, n, k, q, and l are defined in [15].

The following closed-form solution of the SS equations of motion can be formulated when specific initial conditions $\dot{x}_0$ and $\dot{y}_0$ are chosen to remove any secular motion or constant offset terms [15]

$$\begin{aligned} x &= (x_0 - \alpha)\cos(nt\sqrt{1-s}) + \frac{\sqrt{1-s}}{2\sqrt{1+s}} y_0 \sin(nt\sqrt{1-s}) + \alpha\cos(2kt) \\ y &= -\frac{2\sqrt{1+s}}{\sqrt{1-s}}(x_0 - \alpha)\sin(nt\sqrt{1-s}) + y_0\cos(nt\sqrt{1-s}) + \beta\sin(2kt) \\ z &= (lt + m)\sin(qt + \phi) \end{aligned} \tag{2.18}$$

where α, β, $\dot{x}_0$, and $\dot{y}_0$ are defined in [15].

Similarly to the CW model, the cross-track motion of the SS model is decoupled from the radial and in-track motion. Instead, the motion described is a tumbling effect around the $\hat{z}$ axis [15]. The SS model is able to incorporate the J_2, thereby allowing for longer applicability, as there is no unbounded linearization error from assuming no perturbations that exists in the CW model.

2.1.7 Yamanaka-Ankersen Relative Motion Model

The CW and SS models are both limited by their linearization assumptions to circular reference orbit applications. However, spacecraft orbits are not limited to circular orbits, therefore a relative motion model is required to provide accurate RPO capabilities for elliptical orbits. The Yamanaka-Ankersen (YA) relative motion model provides a state transition matrix valid for all orbital eccentricities $0 \leq e < 1$ [16].

The YA relative motion model makes the assumption that the distance between the chief and deputy spacecraft is much smaller than the chief's orbital radius. However, YA differs from CW and SS in that instead of using time t as the independent variable for state propagation, the true anomaly ν of the chief spacecraft is used [16]. The YA model, derived from Tschauner-Hempel [26], also does not suffer from singularities, such as the singularity for circular orbits $e = 0$ that hampers the Tschauner-Hempel solution.

The YA model begins with the Tschauner-Hempel equations,

$$\begin{aligned} \tilde{x}'' - 2\tilde{y}' - \frac{3}{1 + e\cos\nu}\tilde{x} &= 0 \\ \tilde{y}'' + 2\tilde{x}' &= 0 \\ \tilde{z}'' + \tilde{z}' &= 0 \end{aligned} \tag{2.19}$$

where the primes indicate derivatives with respect to true anomaly ν and e is the

chief's orbital eccentricity [27]. In solving the homogeneous second-order differential equation, the YA model introduces an integral $J(t)$,

$$J(t) = \int_{\nu_0}^{\nu} \frac{d\tau}{p(\tau)^2} = k^2(t - t_0) \tag{2.20}$$

where $p \equiv 1 + e\cos\nu$ and $k \equiv \mu/h^{3/2}$ [16], which is responsible for eliminating the singularity exhibited at $e = 0$ by the Tschauner-Hempel equations [28].

For the full derivation of the YA relative motion model STM, the reader is encouraged to explore the original paper by Yamanaka and Ankersen [16]. Interestingly, when $e = 0$ in the YA STM, the CW equations can be recovered, therefore the CW model can be viewed as a special case of the YA model [16, 28].

2.1.8 Gim-Alfriend Relative Motion Model

Combining the benefits of the SS model, which can accurately represent relative motion with J_2 perturbations, and the YA model, which can accurately represent the relative motion of elliptical reference orbits, has been the focus of much research. The Gim-Alfriend (GA) model achieves this in a form for directly propagating the relative states via an STM instead of solving complex relative motion differential equations [17]. The GA model has been employed by NASA in several proximity operations demonstrations [14].

Despite requiring nine pages of appendices in Gim and Alfriend's original paper detailing the relative motion model, the STM can be solved analytically with both mean and osculating elements [17]. The model is a geometric method to propagate relative motion dynamics that can be both eccentric and subject to J_2 perturbations. The element set $\boldsymbol{e} = [a\ \theta\ i\ q_1\ q_2\ \Omega]^T$ is used, where a is the semi-major axis, i is the orbital inclination, θ is the argument of latitude, $q_1 = e\cos\omega$, $q_2 = e\sin\omega$, Ω is the RAAN, e is the eccentricity, and ω is the argument of perigee. This element

set avoids singularities during circular orbits, where true anomaly and argument of perigee are undefined [29].

The implementation of the GA model starts with a state in the relative Hill reference frame. First, the relative Hill frame states are transformed to mean orbital elements followed by a transformation to relative osculating elements, the states are propagated from time t_0 to t, then the osculating states are transformed back to the relative Hill reference frame [17]. Expressed in the unforced STM form,

$$\begin{aligned} \boldsymbol{x}(t) &= \boldsymbol{\Phi}(t, t_0)\boldsymbol{x}(t_0) \\ \boldsymbol{x}(t) &= \{\boldsymbol{A}(t) + \alpha\boldsymbol{B}(t)\}\, \boldsymbol{D}(t)\bar{\boldsymbol{\phi}}_{\bar{e}}(t, t_0)\boldsymbol{D}^{-1}(t_0)\, \{\boldsymbol{A}(t_0) + \alpha\boldsymbol{B}(t_0)\}^{-1}\, \boldsymbol{x}(t_0) \end{aligned} \tag{2.21}$$

where $\{\boldsymbol{A}(t_0) + \alpha\boldsymbol{B}(t_0)\}^{-1}$ transforms the relative Hill states to mean orbital element differences, $\boldsymbol{D}^{-1}(t_0)$ transforms to relative osculating elements, $\bar{\boldsymbol{\phi}}_{\bar{e}}(t, t_0)$ propogates the state forward, $\boldsymbol{D}(t)$ transforms from osculating elements back to the mean orbital elements, and $\{\boldsymbol{A}(t) + \alpha\boldsymbol{B}(t)\}$ transforms back to the relative Hill states.

The GA model assumptions require close proximity between the chief and deputy spacecrafts and the J_2 potential is the only perturbation on the system [29], however the GA model is adaptable for other perturbations [17].

2.1.9 Relative Orbital Elements

The CW equations are parameterized in the relative Hill reference frame based on the orbital mean motion n, relative radial x, in-track y, and cross-track z position and velocities, and the time t from some epoch time t_0. In 2004, Lovell [2] introduced relative orbit elements (ROE) that describe the geometry of a deputy's relative orbit in the relative Hill reference frame, shown in Figure 2.4, based on the relative orbit radius a_e, radial displacement x_d, in-track displacement y_d, angle from the relative orbit perigee β, maximum out-of-plane simple harmonic oscillation displacement z_{max},

and phase angle Ψ.

The unforced relative position and velocity components of the deputy in the relative Hill reference frame expressed in terms of the ROEs is

$$\begin{aligned} x &= -\frac{a_e}{2}\cos\beta + x_d \\ y &= a_e \sin\beta + y_d \\ z &= z_{max}\sin\Psi \\ \dot{x} &= \frac{a_e}{2} n \sin\beta \\ \dot{y} &= a_e n \cos\beta - \frac{3}{2} n x_d \\ \dot{z} &= z_{max} n \cos\Psi \ . \end{aligned} \tag{2.22}$$

Lovell [2] also expressed the ROEs in a form that allows for evolution with time,

$$\begin{aligned} a_e &= a_{e0} \\ x_d &= x_{d0} \\ y_d &= y_{d0} - \frac{3}{2} n x_{d0} t = y_{d0} - \frac{3}{2} n x_d t \\ \beta &= \beta_0 + nt \\ z_{max} &= z_{max0} \\ \Psi &= \Psi_0 + nt \ . \end{aligned} \tag{2.23}$$

Equation 2.23 is analogous to the unforced motion, closed-form solution expressed in Equation 2.14. The relative orbit representation in terms of the ROE provides insight into the geometrical features of a deputy's relative orbit around a chief that can be valuable when conducting formation design. Notably, the relative motion of the deputy with respect to the chief at any time is, when projected in-plane, an instantaneous 2×1 ellipse centered at (x_d, y_d, 0) drifting in the in-track direction at the rate of $-\frac{3}{2} n x_d$. When $x_d > 0$, the deputy will drift in the negative in-track direction. This

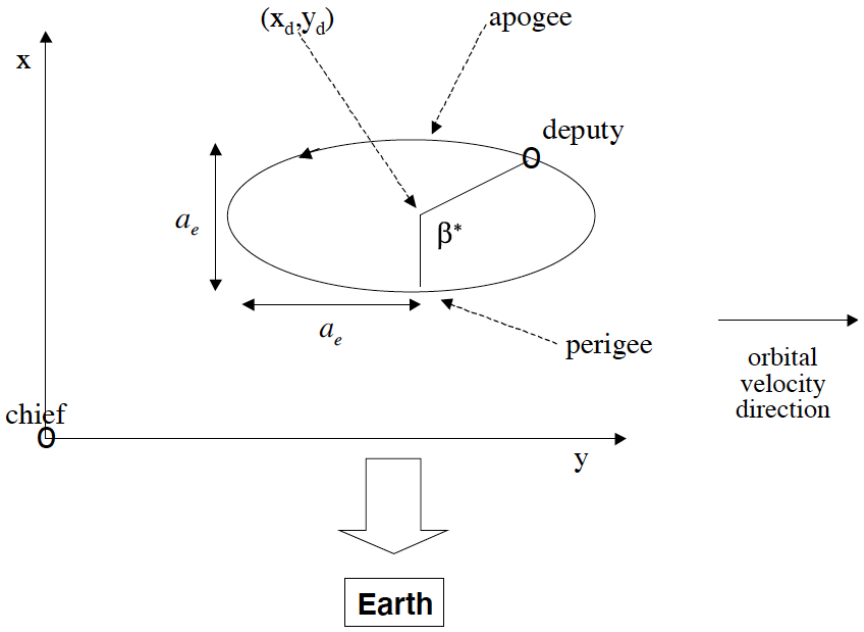

Figure 2.4. Planar projection of relative motion trajectory with ROE labeled [2]

drift can be negated with $y_0 = -2nx_0$, producing Natural Motion Circumnavigation (NMC), and is the scenario applied in this research. $\beta = 0$ corresponds to the perigee location of the chief orbit. Finally, the projection of the relative orbit onto the chief's orbital plane creates a 2×1 ellipse.

2.2 Control Methodologies

There are many approaches available to calculate control laws for RPO missions such as impulsive control approximation with linearized relative motion models, optimal control through Linear Quadratic Regulator, nonlinear control, impulsive, and robust control [30, 31]. For spacecraft with missions requiring formations, formation maintenance is necessary to correct for atmospheric drag, J_2 perturbations, or other disturbances. Control methodologies can be continuous, such as a linear quadratic regulator, while others involve impulsive control thrusts that are assumed instantaneous and must occur at precise timing and magnitude to effectively maneuver the

spacecraft as desired. Minimizing fuel consumption, limitations in control authority such as the amount and direction of thrusters, frequency and duration of control thrusts, and mission objectives must all be considered when determining a particular control approach [31].

2.2.1 Impulsive Maneuvers

Impulsive control input are assumed to occur instantaneously. The impulsive maneuver assumption is useful and valid for longer maneuvers, such as transferring spacecraft between orbits using the Hohmann transfer [32] method. The Hohmann transfer is the energy optimal way to perform transfers between coplanar orbits when assuming a long maneuver and impulsive thrusts [33], where thrusters produce high thrust for a short duration and then coast for a long time.

For close proximity impulsive maneuvering, the relative Hill frame can be useful for targeting [23]. Utilizing the Clohessy-Wiltshire relative orbital dynamics model from Section 2.1.5, this method calculates the required velocity change (Δv) to maneuver the spacecraft to a specific future state. This control technique is impulsive and requires the control input to be applied at specific times to achieve the desired maneuver [31]. CW targeting can be effective for modeling interceptions, where only a specific position is desired and thus an initial burn is conducted to put the spacecraft on a trajectory to reach that position. Two burns, one burn Δv_1 at the beginning to target a desired position, and a second burn Δv_2 can be conducted at the final destination to match velocities for a rendezvous operation. This is referred to as a two-impulse linear rendezvous [23].

From the STM form of the CW equations in Equation 2.16, $\boldsymbol{x}$ can be expressed

as $\boldsymbol{x} = [\boldsymbol{r}\ \boldsymbol{v}]^T$ and $\boldsymbol{\Phi}(t)$ can be divided into the subpartitions

$$\boldsymbol{\Phi}(t) = \begin{bmatrix} \boldsymbol{\Phi}_{rr} & \boldsymbol{\Phi}_{rv} \\ \boldsymbol{\Phi}_{vr} & \boldsymbol{\Phi}_{vv} \end{bmatrix} \tag{2.24}$$

therefore the relative dynamics can be represented as

$$\begin{bmatrix} \boldsymbol{r}(t) \\ \boldsymbol{v}(t) \end{bmatrix} = \begin{bmatrix} \boldsymbol{\Phi}_{rr} & \boldsymbol{\Phi}_{rv} \\ \boldsymbol{\Phi}_{vr} & \boldsymbol{\Phi}_{vv} \end{bmatrix} \begin{bmatrix} \boldsymbol{r}(t_0) \\ \boldsymbol{v}(t_0) \end{bmatrix} \ . \tag{2.25}$$

With a burn Δv_1 applied at t_0, $\boldsymbol{v}(t_0)$ becomes $\boldsymbol{v}(t_0) + \Delta\boldsymbol{v}_1$, thus Equation 2.25 can be written in algebraic form

$$\begin{aligned} \boldsymbol{r}(t) &= \boldsymbol{\Phi}_{rr}\boldsymbol{r}(t_0) + \boldsymbol{\Phi}_{rv}(\boldsymbol{v}(t_0) + \Delta\boldsymbol{v}_1) \\ \boldsymbol{v}(t) &= \boldsymbol{\Phi}_{vr}\boldsymbol{r}(t_0) + \boldsymbol{\Phi}_{vv}(\boldsymbol{v}(t_0) + \Delta\boldsymbol{v}_1) \end{aligned} \tag{2.26}$$

and the change in velocity required for the burn can now be calculated by re-arranging $\boldsymbol{r}(t)$, where $\boldsymbol{r}(t)$ is the desired position vector, as [33]

$$\Delta\boldsymbol{v}_1 = \boldsymbol{\Phi}_{rv}^{-1}\left[\boldsymbol{r}(t) - \boldsymbol{\Phi}_{rr}\boldsymbol{r}(t_0)\right] - \boldsymbol{v}(t_0) \ . \tag{2.27}$$

$\Delta\boldsymbol{v}_1$ will target a desired position in order to intercept the object at that position. For rendezvous operations, collisions are undesirable so the relative velocity must be nullified such that $\boldsymbol{v}(t) + \Delta\boldsymbol{v}_2 = 0$. Therefore, by substituting $\boldsymbol{v}(t) + \Delta\boldsymbol{v}_2 = 0$ into $\boldsymbol{v}(t)$ from Equation 2.26 and solving for $\Delta\boldsymbol{v}_2$, the change in velocity required is

$$\Delta\boldsymbol{v}_2 = -\left[\boldsymbol{\Phi}_{vr}\boldsymbol{r}(t_0) + \boldsymbol{\Phi}_{vv}(\boldsymbol{v}(t_0) + \Delta\boldsymbol{v}_1\right] \ , \tag{2.28}$$

where $\Delta\boldsymbol{v}_1$ is given by Equation 2.27.

It should be noted that there exist times where the subpartition $\mathbf{\Phi}_{rv}$ in the CW STM is not invertible, thus making it impossible to calculate the maneuver burns required to accomplish the targeting mission with the CW STM [34].

2.2.2 Optimal Control

Optimization has applications relevant to nearly any field and spacecraft maneuvering is no exception. Optimization problems entail minimizing or maximizing a given cost functional to achieve a desired requirement. For control problems, cost functionals often require minimizing maneuvering time or control effort. Optimal control is applied in an open-loop system where there are decision variables the solver adjusts in order to minimize the cost functional. A notional representation of a cost functional is below, where $\boldsymbol{x}$ is the system states, t_0 and t_f are the initial and final times, respectively, $\boldsymbol{u}$ is the system control input, J represents the terminal cost of optimization problem, and $\mathcal{L}$ is the running cost of the optimization problem, [35]

$$\min_{t_0,t_f,\boldsymbol{x}(t),\boldsymbol{u}(t)} \quad J(t_0,t_f,\boldsymbol{x}(t_0),\boldsymbol{x}(t_f)) + \int_{t_0}^{t_f} \mathcal{L}(\tau,\boldsymbol{x}(\tau),\boldsymbol{u}(\tau))d\tau \tag{2.29}$$

subject to the system dynamics

$$\dot{\boldsymbol{x}}(t) = \boldsymbol{f}(t,\boldsymbol{x}(t),\boldsymbol{u}(t)) \tag{2.30}$$

subject to the path constraints

$$\boldsymbol{h}(t,\boldsymbol{x}(t),\boldsymbol{u}(t)) \leq 0 \tag{2.31}$$

subject to the boundary constraints

$$\boldsymbol{g}(t_0,t_f,\boldsymbol{x}(t_0),\boldsymbol{x}(t_f)) \leq 0 \tag{2.32}$$

and with bounds on the states, control, time, and initial and final conditions

$$\begin{aligned} \boldsymbol{x}_{min} \leq & \boldsymbol{x}(t) \leq \boldsymbol{x}_{max} \\ \boldsymbol{u}_{min} \leq & \boldsymbol{u}(t) \leq \boldsymbol{u}_{max} \\ t_{min} \leq t_0 < t_f \leq & t_{max} \\ \boldsymbol{x}_{0,min} \leq & \boldsymbol{x}(t_0) \leq \boldsymbol{x}_{0,max} \\ \boldsymbol{x}_{f,min} \leq & \boldsymbol{x}(t_f) \leq \boldsymbol{x}_{f,max} \ . \end{aligned} \tag{2.33}$$

These equations are for a continuous system; however they can easily be adapted for a discrete system. An optimal control policy for RPO missions would utilize the NERMs as the system dynamics for the translational motion. Examples of path constraints may be a specific rendezvous approach vector, a particular path required for inspecting another object, KOZs around other objects, or avoiding the sun vector. Boundary requirements are limits of acceptable values for each condition such as not exceeding a 100 m radius around the initial condition. The remaining bounds on state, control, time, and initial and final conditions are specific to the mission and spacecraft capabilities. Real world optimal control problems are difficult or impossible to solve analytically if employing non-linear dynamics and constraints, but they can be solved numerically with approximation methods, however non-convex optimization problems may be susceptible to local minima.

Walsh and Peck provide a survey of methods for control-optimizing orbital transfer maneuvers [36]. Among the methods, Lawden provided an early approach for optimal control based orbital maneuvering in 1953 with the "Primer Vector" that provided minimum control in two and three dimensions [37, 36]. Prussing minimized the Hamiltonian that is deduced from Pontryagin's Maximum Principle for fixed final time optimal control problems [38]. In 2006, Palmer presented an analytic approach for optimal transfers between orbits for spacecraft formations [39].

Ortolano [40] developed an optimal control algorithm utilizing convex optimization theory for RPO trajectory planning and ensuring global optimality. Irvin compared the performance of optimal control policies with discrete trajectory solutions versus continuous-thrust solutions, concluding that there is a high dependence on the initial and final conditions of the optimal control problem for discrete trajectories to outperform continuous-control trajectories [41]. George [22] utilized optimal control theory in combination with reinforcement learning for fuel-optimal trajectory generation and demonstrated potential for creating robust controllers for autonomous spacecraft using neural networks.

The linear quadratic regulator (LQR) method is a special case of optimal control that computes the state feedback control gain matrix for minimum control optimization problems with full state feedback [42]. The general form of the quadratic cost function is

$$J = \int_0^\infty (\boldsymbol{x}^T \boldsymbol{Q} \boldsymbol{x} + \boldsymbol{u}^T \boldsymbol{R} \boldsymbol{u}) dt \tag{2.34}$$

subject to linear system dynamics

$$\dot{\boldsymbol{x}}(t) = \boldsymbol{f}(t, \boldsymbol{x}(t), \boldsymbol{u}(t)) \tag{2.35}$$

where the feedback control law is

$$\boldsymbol{u} = -\boldsymbol{K} \boldsymbol{x} \tag{2.36}$$

where the objective is, through chosen gain matrices $\boldsymbol{Q}$ (positive-definite or positive semi-definite) and $\boldsymbol{R}$ (positive definite), to minimize the cost function by finding the optimal feedback matrix $\boldsymbol{K}$ where [42]

$$\boldsymbol{K} = \boldsymbol{R}^{-1} \boldsymbol{B} \boldsymbol{P} \tag{2.37}$$

and is computed by the stabilizing solution of the Algebraic Riccati Equation (ARE)

$$\boldsymbol{P}\boldsymbol{A} + \boldsymbol{A}^T\boldsymbol{P} - \boldsymbol{P}\boldsymbol{B}\boldsymbol{R}^{-1}\boldsymbol{B}^T\boldsymbol{P} + \boldsymbol{Q} = 0 \ . \tag{2.38}$$

The gain matrix $\boldsymbol{Q}$ determines the weighting of the state regulation error while gain matrix $\boldsymbol{R}$ determines the weighting of the control effort. That is, a larger $\boldsymbol{Q}$ will yield a faster convergence to the goal with more control expenditure because minimizing the error in the feedback state is more important. A larger $\boldsymbol{R}$ will emphasize control efficiency and result in a longer convergence time to the goal. Given the algebraic computation of the LQR, it is quite efficient when compared to other optimal control methods [43]. LQR controllers, however, are only valid for linear systems. Real-world systems are typically non-linear and must be linearized when applying LQR controllers. Additionally, the gain matrices $\boldsymbol{Q}$ and $\boldsymbol{R}$ require tuning to achieve the desired result such as more control and faster convergence, or vice versa. Since LQR is a feedback controller, the states must be measurable in order to minimize the phase error in the feedback loop.

For some spacecraft rendezvous problems, the above constraints of LQR controllers can be met. Yang [44] showed LQR's usefulness compared to a proportional-derivative control design for attitude control of spacecraft. Bevilacqua [45] utilized the LQR in conjunction with an artifical potential function for multiple spacecraft control where the LQR optimized fuel consumption and the artificial potential function was employed for collision avoidance measures while accounting for local minima traps. Guarnaccia, et al. [46] demonstrated a real time, LQR-based sub-optimal approach for combined translational and rotational spacecraft control.

2.2.3 Artificial Potential Functions

Artificial potential functions (APFs) are widely used in autonomous vehicles such as robotics and spacecraft, often implemented to target a desired location while avoiding undesirable locations [47, 45, 48, 49]. When APFs are utilized for an object, such as a spacecraft, it behaves as if it is in a "field of forces", as it was described by Khatib [47], who first introduced the use of artificial potential functions in robotics. An attractive force is located at the target location, "pulling" the spacecraft towards the target following the gradient of the gravitational potential, while repulsive forces represent any obstacles that must be avoided, such as other spacecraft or keep-out zones, "push" the spacecraft away from those locations with larger gravitational potentials. The combination of these forces produce the APF with a global minimum at the target which the spacecraft will follow to achieve its target location while maintaining collision avoidance requirements, shown in Figure 2.5.

Computational simplicity is where APFs thrive. The attractive and repulsive functions are analytical expressions that yield a scalar and are described in further detail in Chapter III. Thus, they can be computed easily. This attribute allows for real-time computation of the potential field from information known *a priori*, as first introduced for spacecraft applications by Lopez and McInnes [50], or gathered real-

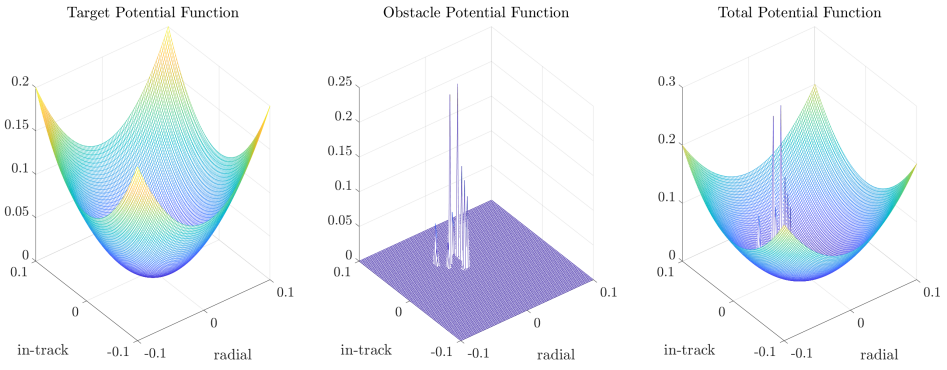

Figure 2.5. Construction of an Artifical Potential Function

time from on-board sensors [51].

A drawback to implementing APFs for deriving guidance control laws is the existence of local minima. Local minima are created when obstacles are in close proximity to each other. The high potential areas created by the obstacles can combine to trap the spacecraft in the local minima. Several methods, such as applying "escape forces" [52, 53], have been explored to overcome the local minima problem. Defining obstacle repulsive functions as sharp spires instead of wide rolling hills is one method to mitigate this local minima problem.

Applications of APFs for autonomous maneuvering have been extensively researched. In 2007, Badawy and McInnes introduced a method of robotic path planning that leverages a hyperboloid potential function, in contrast to a parabolic potential function. The hyperboloid potential function provides the benefit of a constant gradient far from the global minimum that incorporates a parabolic shape at the global minimum to avoid a singularity [54]. Muñoz applied APFs in the spacecraft RPO domain in 2011, where various methodologies were applied for improving the convergence likelihood of close-range rendezvous operations [55]. Fields developed a continuous control APF by relating the system's velocity to the negative of the potential function's gradient and explored methods of increasing optimality by utilizing the control law derived from the continuous control APF as the cost function to be minimized in the optimal control problem. However, the computational expense proved non-advantageous compared to more traditional optimal control approaches [49].

In this research, an APF is utilized to generate the control law based on the computed reach set to maneuver a deputy spacecraft in an NMC orbit to a rendezvous with the chief spacecraft at the origin of the relative orbit while avoiding obstacles.

2.3 Reachability Analysis

Reachability analysis can be a valuable component in the autonomous mission planning system if conducted efficiently. Reachability analysis is the process of computing the set of states that can be reached given all possible controls. Forward reachability consists of computing all possible end states in a finite time interval given a known initial condition. Forward reachability analysis can be defined as, adapted from [56, 10],

> *The set of final states x_f achievable in time t_f or less by a dynamical system, in the form of a differential equation*
>
> $$\dot{x} = f(x, v) \ ,$$
>
> *starting at an initial state x_0 at t_0, with a set of admissible m-dimensional control input $\boldsymbol{u}(t) \in \mathcal{U} \subset \mathbb{R}^m$.*

Backward reachability consists of computing all possible initial conditions that can reach a particular end state or states given a finite time interval.

> *The set of initial states x_0 that in time t_f or less by a dynamical system, in the form of a differential equation*
>
> $$\dot{x} = f(x, v) \ ,$$
>
> *can reach a final state x_f at t_f, with a set of admissible m-dimensional control input $\boldsymbol{u}(t) \in \mathcal{U} \subset \mathbb{R}^m$.*

From the mission planning and verification perspective, reachability analysis can provide the reach sets for spacecraft under continuous thrust maneuvers with long intervals between observations [57]. This can be helpful for recovering position tracking of a spacecraft if it is being tracked but the tracking capability is lost, because a known reach set region becomes the search area for re-acquisition. With formations,

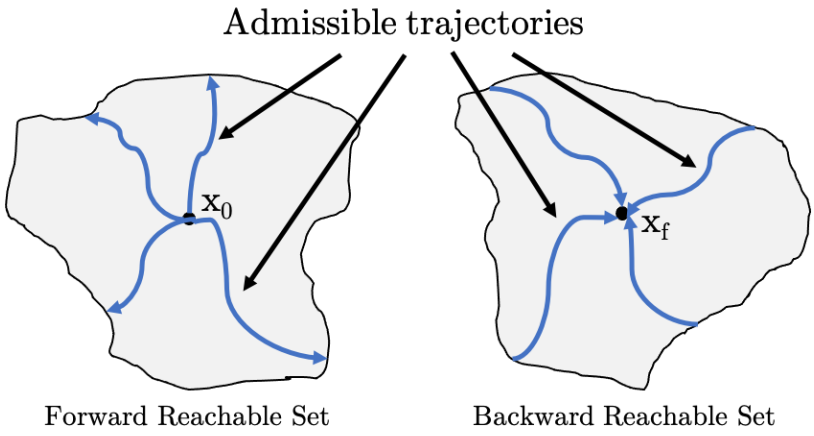

Figure 2.6. Notional representations of forward and backward reach sets

reachability analysis can aid in modeling the extent to which a formation geometry can be changed given time and control constraints [57]. Collision avoidance has also been demonstrated in the case of an air traffic control differential game [58]. Implementing autonomous guidance, navigation, and control algorithms can be aided by first identifying whether a certain maneuver is feasible or not, that is ensuring it can actually be accomplished given the system constraints [10].

Exact reachability analysis entails solving a Hamilton-Jacobi-Bellman (HJB) partial differential equation (PDE) with non-linear dynamics and is often intractable for real-world systems. Exact reachability analysis suffers from the "curse of dimensionality." HJB reachability computational complexity scales exponentially with respect to the number of dimensions, as shown in Figure 2.7. 1D and 2D reach sets can be computed very quickly with little random access memory (RAM) usage. 3D reach sets can take minutes to hours while 4D reach sets can take many hours with many gigabytes of RAM usage. At 5D and 6D, computational and space complexity make the computation intractable [3].

In a robotics application, "warm starting" the reachability analysis has demonstrated significant computational improvement in compute time by initializing the

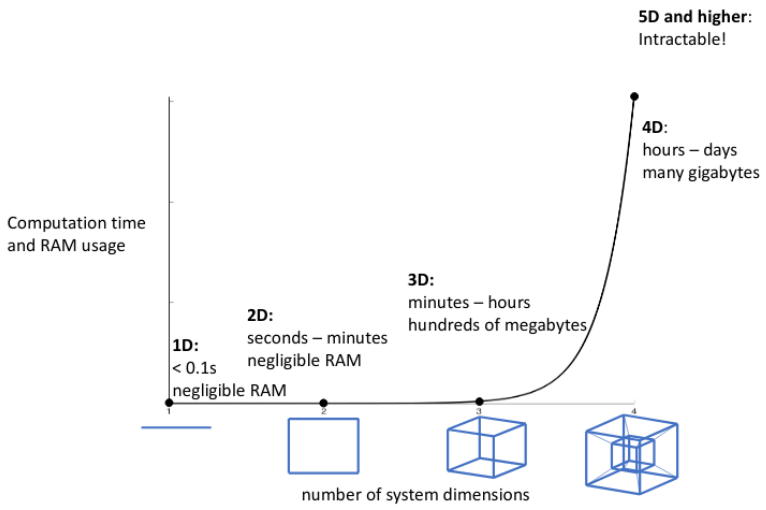

Figure 2.7. Illustration of computational complexity of HJB reachability (reproduced from Chen [3])

next reachability computation with the previous time step's solution and only performing the computation on the new positions within an agent's sensor [59]. The Parallel Interval Reachability Kernel (PIRK) is a tool to efficiently compute approximate reach sets by leveraging parallel computing on high-performance computing platforms which can support state dimensions up to 4 billion [60].

Geometric approximation is another method employed to conduct reachability analysis on higher dimensional systems without the computational and space complexity of exact reachability analysis. Many analytical approaches have been developed that leverage geometric polytopes or ellipsoids to approximate the reach set [61, 62]. These methods are readily leveraged in problems such as safety verification or trajectory verification as they over-approximate the reach set, thus ensuring all safe trajectories are accounted for [62].

Reachability analysis has been applied to collision avoidance or control verification problems for robotics, autonomous cars, and unmanned aerial vehicles [63, 64, 65, 66, 67]. In the space domain, in 2021, Marsillach applied reachability analysis in the form of ellipsoidal approximation for the purposes of telescope tasking [68]. Reachability

analysis is used to compute the reach set of states within a specified amount of time in order to pair spacecraft with telescopes via a tasking algorithm. Allen, et al. utilized a classification machine learning algorithm to identify reach states for a deep-space spacecraft, however misclassifications may occur which may not be acceptable for a specific mission [69].

Reachability analysis is being leveraged more recently for spacecraft RPO trajectory planning. Reachability analysis was studied for Space Domain Awareness in 2007 by Holzinger and Scheeres in RPO and formation flying missions for considerations regarding control authority characterization, correlating object detection with trajectory planning, and "stuck" thrusters in 2 degrees of freedom dynamics where cross-track motion was ignored [70]. Holzinger and Sheeres found approximating the reach set with ellipsoidal reach set approximation diverges from the exact reach set solution after a period of time. Zagaris and Romano performed reachability analysis for a RPO and docking of a deputy spacecraft to a tumbling object, where the feasibility of docking was analyzed given variations in the rotational velocity of the tumbling object [10, 71, 72]. A stochastic reachability method was developed for spacecraft RPO with an open-loop controller, as a constrained optimization problem, however they were unsuccessful implementing a state-based feedback controller [73]. Recently, Zagaris and Hess demonstrated a computationally efficient method for computing reach sets for spacecraft relative motion given single impulse maneuvers utilizing an analytical STM to propagate relative motion and ellipsoidal reach set approximation [74].

The ellipsoidal reach set approximation approach was published by Kurzhanskiy and Varaiya [61] and implemented as a MATLAB® toolbox. Kurzhanskiy and Varaiya's method implements ellipsoidal calculus [75] for continuous-time, discrete-time, and linear systems with disturbances on both open- and closed-loop reach sets.

Ellipsoidal reach set approximation provides several benefits compared to other methods, such as the exact HJB computational method:

- Computational complexity grows quadratically by state dimensionality and linearly by number of time steps.
- The exact reach set can be represented by computing the intersections of external and internal ellipsoids.
- Specific external or internal ellipsoids can be extracted if beneficial, such as a particular volume, diameter, or ellipsoid eigenvectors, etc.
- The control can be modeled as simple analytical expressions.

The ellipsoid, as defined by Kurzhanskiy and Varaiya [61], has a center $\boldsymbol{q}$ and a positive definite or positive semi-definite shape matrix $\boldsymbol{Q}$,

$$\mathcal{E}(\boldsymbol{q}, \boldsymbol{Q}) = \{\boldsymbol{x} \in \boldsymbol{R}^n | \langle (\boldsymbol{x} - \boldsymbol{q}), \boldsymbol{Q}^{-1}(\boldsymbol{x} - \boldsymbol{q}) \rangle \leq 1\} \ . \tag{2.39}$$

The process of calculating an ellipsoidal approximation of a reach set utilizes the following operations on ellipsoids that are integral to ellipsoidal calculus:

- Affine transformation
- Geometric sums of a finite number of ellipsoids
- Geometric difference of two ellipsoids
- Intersections of a finite number of ellipsoids

The methods used for affine transformations, geometric sums, and intersections of ellipsoids are detailed here for their direct relation to the methodology described in Section 3.2 for computing reach set approximations in this research.

Affine transformations are useful for projections, where a higher dimensional system such as a three-dimensional ellipsoid is projected onto two dimensions. For higher dimensional systems, such as a six state relative motion model ($\boldsymbol{x} = [x\ y\ z\ \dot{x}\ \dot{y}\ \dot{z}]^T$), it may be useful to project the resulting ellipsoid into two or three dimensions for visualizations on plots. Affine transformations preserve the ellipsoidal geometry.

Geometric sum operations on ellipsoids generally do not yield an ellipsoid. However, the geometric sum of the two ellipsoids can be approximated as an ellipsoid. An external ellipsoidal approximation completely contains the geometric sum of each ellipsoid $1 \cdots k$, defined as

$$\mathcal{E}(\boldsymbol{q}_1, \boldsymbol{Q}_1) \oplus \cdots \oplus \mathcal{E}(\boldsymbol{q}_k, \boldsymbol{Q}_k) \subseteq \mathcal{E}(\boldsymbol{q}, \boldsymbol{Q}_{\boldsymbol{l}}^+) \tag{2.40}$$

and with support functions

$$\rho(\pm\boldsymbol{l} \mid \mathcal{E}(\boldsymbol{q}_1, \boldsymbol{Q}_1)) \oplus \cdots \oplus \rho(\pm\boldsymbol{l} | \mathcal{E}(\boldsymbol{q}_k, \boldsymbol{Q}_k)) = \rho(\pm\boldsymbol{l} \mid \mathcal{E}(\boldsymbol{q}, \boldsymbol{Q}_{\boldsymbol{l}}^+)) \tag{2.41}$$

where $\boldsymbol{l}$ is a nonzero vector in $\boldsymbol{R}^n$, and center $\boldsymbol{q}$ is $\boldsymbol{q}_1 + \cdots + \boldsymbol{q}_k$. The shape matrix of the external approximation of the geometric sum of ellipsoids is

$$\boldsymbol{Q}_{\boldsymbol{l}}^+ = \left(\langle \boldsymbol{l}, \boldsymbol{Q}_1 \boldsymbol{l}\rangle^{\frac{1}{2}} + \cdots + \langle \boldsymbol{l}, \boldsymbol{Q}_k \boldsymbol{l}\rangle^{\frac{1}{2}}\right)\left(\frac{1}{\langle \boldsymbol{l}, \boldsymbol{Q}_1 \boldsymbol{l}\rangle^{\frac{1}{2}}}\boldsymbol{Q}_1 + \cdots + \frac{1}{\langle \boldsymbol{l}, \boldsymbol{Q}_k \boldsymbol{l}\rangle^{\frac{1}{2}}}\boldsymbol{Q}_k\right) \tag{2.42}$$

where $\boldsymbol{l}$ is the direction along which the approximation is tight.

Like the geometric sum of ellipsoids, the intersection of ellipsoids is also generally not an ellipsoid. The intersection can be approximated as an ellipsoid via the optimization methodology described in [74].

This research is motivated by the need for a computationally efficient method for verifying object detection for guidance planning in spacecraft RPO applications and

utilizes the approach in [74] for computing reach sets to support collision avoidance.

III. Solution Methodology

This research analyzes reach set solutions computed by different relative motion models. Each model has specific assumptions that determine its applicability to various orbits. The reach sets from each model at a range of orbit sizes and shapes will be compared with each other and analyzed for their accuracy and real-time, on-board computational feasibility. Next, two methods are combined for implementing safe, verifiable trajectories of spacecraft in relative orbit. The APF provides the means for computing the control profile required to rendezvous a deputy spacecraft with a chief spacecraft while avoiding collisions with obstacles. Reachability analysis identifies the reach set such that all obstacles within the reach set can be activated in the APF. This approach is such that the reach set can mimic spacecraft sensors detecting spacecraft on-board and in real-time while also providing a verification that the trajectory calculated by the APF is valid.

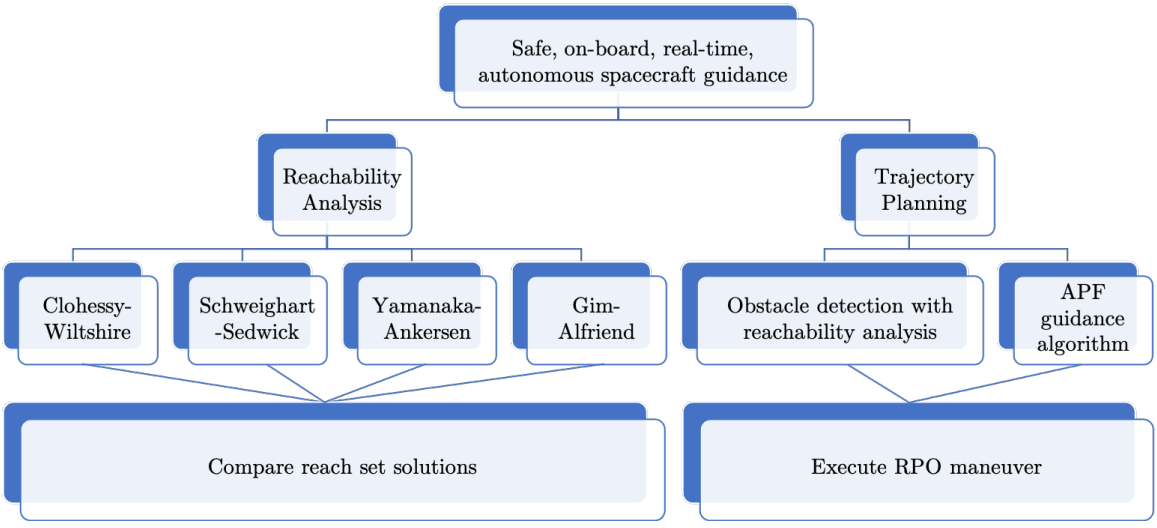

Figure 3.1. Research methodology flowchart

3.1 State Dynamics

The unforced state transition matrix form of the relative motion dynamics, which propagates the current relative state forward a predetermined time to a new state, is defined by

$$\boldsymbol{x}(t) = \boldsymbol{\Phi}(t)\boldsymbol{x}(t_0),\ \boldsymbol{x} = [x\ y\ z\ \dot{x}\ \dot{y}\ \dot{z}]^T\ . \tag{3.1}$$

In order to model the forced equations of motion using the CW state matrix form, an impulsive control $\Delta v[t]$ is added to the velocity such that the forced dynamics become

$$\begin{aligned}
\begin{bmatrix} \boldsymbol{r}[t+1] \\ \boldsymbol{v}[t+1] \end{bmatrix} &= \boldsymbol{\Phi}(\Delta t) \begin{bmatrix} \boldsymbol{r}[t] \\ \boldsymbol{v}[t] + \Delta\boldsymbol{v}[t] \end{bmatrix} \\
\begin{bmatrix} \boldsymbol{r}[t+1] \\ \boldsymbol{v}[t+1] \end{bmatrix} &= \begin{bmatrix} \boldsymbol{\Phi}_{rr} & \boldsymbol{\Phi}_{rv} \\ \boldsymbol{\Phi}_{vr} & \boldsymbol{\Phi}_{vv} \end{bmatrix} \begin{bmatrix} \boldsymbol{r}[t] \\ \boldsymbol{v}[t] + \Delta\boldsymbol{v}[t] \end{bmatrix} \\
\begin{bmatrix} \boldsymbol{r}[t+1] \\ \boldsymbol{v}[t+1] \end{bmatrix} &= \begin{bmatrix} \boldsymbol{\Phi}_{rr} & \boldsymbol{\Phi}_{rv} \\ \boldsymbol{\Phi}_{vr} & \boldsymbol{\Phi}_{vv} \end{bmatrix} \begin{bmatrix} \boldsymbol{r}[t] \\ \boldsymbol{v}[t] \end{bmatrix} + \begin{bmatrix} \boldsymbol{\Phi}_{rv} \\ \boldsymbol{\Phi}_{vv} \end{bmatrix} \Delta\boldsymbol{v}[t] \\
\boldsymbol{x}[t+1] &= \begin{bmatrix} \boldsymbol{\Phi}_{rr} & \boldsymbol{\Phi}_{rv} \\ \boldsymbol{\Phi}_{vr} & \boldsymbol{\Phi}_{vv} \end{bmatrix} \boldsymbol{x}[t] + \begin{bmatrix} \boldsymbol{\Phi}_{rv} \\ \boldsymbol{\Phi}_{vv} \end{bmatrix} \boldsymbol{u}[t] \\
\boldsymbol{x}[t+1] &= \boldsymbol{\Phi}(\Delta t)\boldsymbol{x}[t] + \boldsymbol{\Phi}(\Delta t) \begin{bmatrix} \boldsymbol{0} \\ \boldsymbol{I} \end{bmatrix} \boldsymbol{u}[t]
\end{aligned} \tag{3.2}$$

where $\boldsymbol{\Phi}(t)$ is the STM of the particular relative motion model used to transfer the states from an initial state to a final state over a specific period of time, and $\boldsymbol{\Phi}_{rr}$, $\boldsymbol{\Phi}_{rv}$, $\boldsymbol{\Phi}_{vr}$, and $\boldsymbol{\Phi}_{vv}$ are the sub-partitions of $\boldsymbol{\Phi}(t)$.

3.2 Reachability Analysis

In practical applications, all obstacles may not be known *a priori*, therefore a spacecraft may employ sensors to identify obstacles that must be avoided during a maneuver. Reachability analysis is employed as a means to identify the "field of view" for which the obstacles are defined.

Relative motion models for spacecraft can be simplified to a 4D model but 6D models can also be required. As previously mentioned, the computational complexity of computing exact reach sets via solving the HJB PDE grows exponentially and is impractical for 4D and intractable for 6D. Therefore, to avoid the computational requirements of exact reach set solutions, reach set approximation via ellipsoidal calculus is used here to compare the solutions of several linearized spacecraft relative motion models. Ellipsoidal reach set approximations inherently over-approximate the exact reach set, thereby ensuring no obstacle within the exact reach set is omitted as a result of approximation [61]. Ellipsoidal reach set approximation is based on the assumption that the reach set is approximately ellipsoidal when projected onto 3D-subspace.

From the Ellipsoidal Toolbox [61], an ellipsoid can be defined in $\boldsymbol{R}^n$ with a center q and a shape matrix Q where

$$\mathcal{E}(\boldsymbol{q}, \boldsymbol{Q}) = \{\boldsymbol{x} \in \boldsymbol{R}^n | \langle (\boldsymbol{x} - \boldsymbol{q}), \boldsymbol{Q}^{-1}(\boldsymbol{x} - \boldsymbol{q}) \rangle \leq 1\} \tag{3.3}$$

wherein $\boldsymbol{q}$ is the center of the ellipsoid and $\boldsymbol{Q}$ is a positive definite matrix that defines the size and orientation of the ellipsoid.

Reach set approximation via ellipsoidal approximation requires an initial state ellipsoid $\mathcal{E}(\boldsymbol{q}_x, \boldsymbol{Q}_x)$, control ellipsoid $\mathcal{E}(\boldsymbol{q}_{zi}, \boldsymbol{Q}_{zi})$ and $\mathcal{E}(\boldsymbol{q}_{zs}, \boldsymbol{Q}_{zs})$, system dynamics $\boldsymbol{\Phi}$, and a time step t. The reach set approximation is only valid for a single initial impulse

at the time which the reach set is computed.

3.2.1 The State Ellipsoid

For the deputy spacecraft, the center of the initial state ellipsoid $\boldsymbol{q}_x$ is defined by the initial state vector $\boldsymbol{x} = [x\ y\ z\ \dot{x}\ \dot{y}\ \dot{z}]^T$. The shape matrix $\boldsymbol{Q}_x$ is defined by a 6x6 matrix where the position error and velocity error are on the diagonal

$$\boldsymbol{Q}_x = \begin{bmatrix} \tilde{x}^2_{error} & 0 & 0 & 0 & 0 & 0 \\ 0 & \tilde{y}^2_{error} & 0 & 0 & 0 & 0 \\ 0 & 0 & \tilde{z}^2_{error} & 0 & 0 & 0 \\ 0 & 0 & 0 & \dot{\tilde{x}}^2_{error} & 0 & 0 \\ 0 & 0 & 0 & 0 & \dot{\tilde{y}}^2_{error} & 0 \\ 0 & 0 & 0 & 0 & 0 & \dot{\tilde{z}}^2_{error} \end{bmatrix}. \tag{3.4}$$

3.2.2 The Control Ellipsoid

The center of the control matrix is defined by the zero-input vector made by

$$\boldsymbol{q_{zi}} = \boldsymbol{\Phi}_{rr}(t, t_0)\boldsymbol{r}_0 + \boldsymbol{\Phi}_{rv}(t, t_0)\boldsymbol{v}_0 \tag{3.5}$$

where r is the radial and in-track states, v is the radial and in-track velocities, and $\boldsymbol{\Phi}_{rr}$ and $\boldsymbol{\Phi}_{rv}$ are two sub-partitions of $\boldsymbol{\Phi}(t)$.

The shape of the control matrix is comprised of a geometric sum of the zero-input ellipsoid and the zero-state ellipsoid. The zero-input ellipsoid is defined in Equation 3.6.

$$\boldsymbol{Q}_{zi} = \boldsymbol{A}\boldsymbol{Q}_x\boldsymbol{A}^T \tag{3.6}$$

where

$$\boldsymbol{A} = \begin{bmatrix} \boldsymbol{\Phi}_{rr}(t, t_0) & \boldsymbol{\Phi}_{rv}(t, t_0) \end{bmatrix} \tag{3.7}$$

and represents the ellipsoidal approximation of the reach set from the initial conditions but without an initial input.

The zero-state ellipsoid is defined with the center $\boldsymbol{q}_{zs}$ at the nominal initial state $\boldsymbol{x}_0$, i.e. without uncertainty, and shape matrix $\boldsymbol{Q}_{zs}$ defined as [74]

$$\begin{aligned} \boldsymbol{q}_{zs} &= \boldsymbol{q}_{zi} \\ \boldsymbol{Q}_{zs} &= \boldsymbol{\Phi}_{rv}(t, t_0) \boldsymbol{Q}_{\Delta v} \boldsymbol{\Phi}_{rv}^T(t, t_0) \end{aligned} \tag{3.8}$$

where

$$\boldsymbol{Q}_{\Delta v} = u_{max}^2 \boldsymbol{I} \tag{3.9}$$

and represents the ellipsoidal approximation of the reach set with the initial input.

3.2.3 Computing the Reach Set

For the scenario where a spacecraft cannot impart any control forces ($u_{max} = 0$), the total reach set ellipsoid $\boldsymbol{Q}_R$ is equal to the zero-input ellipsoid $\boldsymbol{Q}_{zi}$. When control forces are non-zero, the zero-state ellipsoid is added to the zero-input ellipsoid via geometric sum. The sum of two ellipsoids do not generally produce another ellipsoid, so an ellipsoidal approximation of the geometric sum is produced as described in Section 2.3. Therefore, the ellipsoidal reach set approximation for a relative motion model with an impulsive control is

$$\boldsymbol{Q}_R = \left(\langle \boldsymbol{l}, \boldsymbol{Q}_{zi} \boldsymbol{l} \rangle^{\frac{1}{2}} + \langle \boldsymbol{l}, \boldsymbol{Q}_{zs} \boldsymbol{l} \rangle^{\frac{1}{2}} \right) \left(\frac{1}{\langle \boldsymbol{l}, \boldsymbol{Q}_{zi} \boldsymbol{l} \rangle^{\frac{1}{2}}} \boldsymbol{Q}_{zi} + \frac{1}{\langle \boldsymbol{l}, \boldsymbol{Q}_{zs} \boldsymbol{l} \rangle^{\frac{1}{2}}} \boldsymbol{Q}_{zs} \right) \tag{3.10}$$

where $\boldsymbol{l}$ is the eigenvector associated with the largest eigenvalue. This direction $\boldsymbol{l}$ is chosen so that ellipsoidal approximation of the geometric sum of the state and input ellipsoids is tight along that direction, thus enabling the best possible ellipsoidal approximation of the geometric sum.

3.3 Evaluating Reach Sets With Different Relative Motion Models

This section aims towards answering the first question posed in this research from Section 1.2.1: How do relative motion models impact the reach set solution? Approximate reach set calculations are performed over a set time interval while predicting a defined number of reach sets into the future. The impact of different relative motion models on the reach set given a defined orbit is studied and quantified per the Figure of Merit defined below. The scenario studied is a spacecraft in orbit that is the origin of a relative Hill reference frame. Four relative motion models are used to model the system dynamics and are chosen based on their range of assumptions for which their solutions are valid. The Clohessy-Wiltshire, Schweighart-Sedwick, Yamanaka-Ankersen, and Gim-Alfriend models are used in the closed form STM in Equation 3.11 where $\boldsymbol{\Phi}(t, t_0)$ represents the forced STM dynamics which transfers the system from its current state $x(t_0)$ to the next state $x(t)$,

$$\boldsymbol{x}[t+1] = \boldsymbol{\Phi}(\Delta t)\boldsymbol{x}[t] + \boldsymbol{\Phi}(\Delta t) \begin{bmatrix} \boldsymbol{0} \\ \boldsymbol{I} \end{bmatrix} \boldsymbol{u}[t] \ . \tag{3.11}$$

The CW model is valid for relatively short distances, circular orbits, and does not account for any disturbances or perturbations [12]. The SS model is valid for relatively short distances, circular orbits, and accounts for J_2 perturbations [15]. The YA model is valid for relatively short distances, elliptic orbits, and does not account for disturbances or perturbations [16]. The GA model is valid for relatively short

distances, elliptic orbits, and accounts for J_2 perturbations.

Table 3.1. Assumptions of each relative motion model

Model	Range	Eccentricity	Perturbations
Clohessy-Wilshire (CW)	Short distances	Circular ($e = 0$)	None
Schweighart-Sedwick (SS)	Short distances	Circular ($e = 0$)	J_2
Yamanaka-Ankersen (YA)	Short distances	Elliptic ($0 \leq e < 1$)	None
Gim-Alfriend (GA)	Short distances	Elliptic ($0 \leq e < 1$)	J_2

Analysis of the reach sets will be conducted by comparing the size, shape, and orientation of the reach sets computed for each relative motion model. These representations of the reach sets are used as the Figure of Merit for the relative motion model reach set evaluation. The metrics presented include the Euler angle of the semi-major axis of the reach set ellipsoid, volume of the ellipsoid, and trace of the ellipsoid. With computational efficiency being necessary for on-board autonomous guidance planning, the computation time of each reach set for each relative motion model is also presented and discussed. These metrics will support conclusions for the first and third research questions posed in this work from Section 1.2.1.

3.4 Artificial Potential Function

Often, APFs act on the position of the spacecraft, $\boldsymbol{x}_d = [x_d, y_d]$, with respect to the chief's location, $\boldsymbol{x}_c = [x_c, y_c]$, and all i obstacles, $\boldsymbol{x}_{o,i} = [x_{o,i}, y_{o,i}]$ [49].

The attractive potential function serves to provide a global minimum at the target location such that the spacecraft follows the negative potential gradient towards the global minimum. A quadratic attractive potential function is used and defined as [55, 48]

$$\Phi_a(\boldsymbol{x}) = \frac{k_a}{2} \boldsymbol{r}_{cf}^T \boldsymbol{P} \boldsymbol{r}_{cf} \tag{3.12}$$

where k_a is a strictly positive constant, $\boldsymbol{r}_{cf} = \boldsymbol{x}_d - \boldsymbol{x}_c$ is the relative position between the deputy and chief spacecrafts, and $\boldsymbol{P}$ is a symmetric positive-definite weighting

matrix that shapes the potential function.

The repulsive functions serve as areas of large potential which create a positive potential gradient surrounding the obstacles to be avoided. Since the APF controller seeks to follow the negative gradient potential to reach the global minimum expeditiously, these large potential areas defined in the repulsive function are avoided. The repulsive function is defined using a Gaussian function that can accommodate N obstacles [55, 48],

$$\Phi_r(\boldsymbol{x}) = \sum_{i=1}^{N} \psi_i \exp\left[-\frac{\boldsymbol{r}_{co,i}^T \boldsymbol{N}_i \boldsymbol{r}_{co,i}}{\sigma_i}\right] \tag{3.13}$$

where $\boldsymbol{r}_{co,i} = \boldsymbol{x}_d - \boldsymbol{x}_{o,i}$ is the relative position between the deputy and the ith obstacle, ψ_i and σ_i are height and width parameters, respectively, and $\boldsymbol{N}_i$ is a symmetric positive-definite weighting matrix that shapes the ith repulsive potential [55].

The total potential function is the sum of the attractive potential function and the repulsive potential function,

$$\Phi_{tot} = \Phi_a + \Phi_r \ . \tag{3.14}$$

A continuous feedback control law is defined to provide finer control when in close proximity to the terminal state at the chief spacecraft [49, 48],

$$\boldsymbol{u}(\boldsymbol{r}_{cf}, \boldsymbol{r}_{co}, \boldsymbol{v}_{cf}) = -\boldsymbol{B}^{-1}\boldsymbol{K}_a(\boldsymbol{v}_{cf} + \Delta_x \Phi_{tot}) \ , \tag{3.15}$$

where $\boldsymbol{K}_a$ is a positive gain matrix, $\boldsymbol{v}_{cf}$ is the relative velocity between the deputy and the chief spacecrafts, $\boldsymbol{B}$, from Equation 3.2, is

$$\boldsymbol{B} = \Phi(t) \begin{bmatrix} \boldsymbol{0} \\ \boldsymbol{I} \end{bmatrix} \ , \tag{3.16}$$

and $\Delta_x \Phi_{tot}$ is the gradient of the potential function given by [48],

$$\Delta_x \Phi_{tot} = k_a \boldsymbol{P} \boldsymbol{r}_{cf} - \sum_{i=1}^{N} \frac{2\psi_i}{\sigma_i} \exp\left[-\frac{\boldsymbol{r}_{co,i}^T \boldsymbol{N}_i \boldsymbol{r}_{co,i}}{\sigma_i} \right] \boldsymbol{N}_i \boldsymbol{r}_{co,i} \ . \tag{3.17}$$

3.5 Reach/APF Algorithm

The reach/APF algorithm initiates at time t_0 and state $\boldsymbol{x}_0$ which, in this research, resides on an NMC orbit around a chief spacecraft. When the maneuver is initiated, the difference between the current location and the target is calculated, which helps define the graident of the APF $\Delta\Phi_{tot}$.

The reach set is computed via the calculations described in Chapter 3.2 utilizing the CW relative motion model.

Next, each obstacle that exists is modeled as an ellipsoid where $\boldsymbol{q}_{obs}$ is the location of the obstacle and $\boldsymbol{Q}_{obs}$ is the shape matrix defined by the radius of the obstacle,

$$\boldsymbol{Q}_{obs} = r_{obs}^2 \boldsymbol{I} \ . \tag{3.18}$$

In order to identify the relevant obstacles at this time step, each obstacle ellipsoid is checked for intersection with the reach set ellipsoid. If the obstacle intersects with the reach set ellipsoid, that obstacle's repulsive function is activated per Equation 3.13. If no intersection exists, $\Phi_{r,i} = 0$. Calculating the intersection between ellipsoids identifies which obstacles are reachable by the deputy spacecraft at that time step and are accounted for in the repulsive function portion of the artificial potential function. This intersection calculation is generally not an ellipsoid, however the intersection can be approximated by an ellipsoid via the method described in [74]. For this research, the actual shape of the intersection is not utilized, only a binary indication of an intersection with an obstacle.

With the attractive and repulsive functions calculated, the total artificial potential function can be calculated. The continuous feedback control law is then calculated from the gradient potential function $\nabla_x \Phi_{tot}$. The resulting control $\boldsymbol{u}$ is applied to the system dynamics from Equation 3.2 and the deputy spacecraft maneuvers to a new position.

This process repeats at a set time interval for a set duration or until the deputy spacecraft rendezvous with the chief.

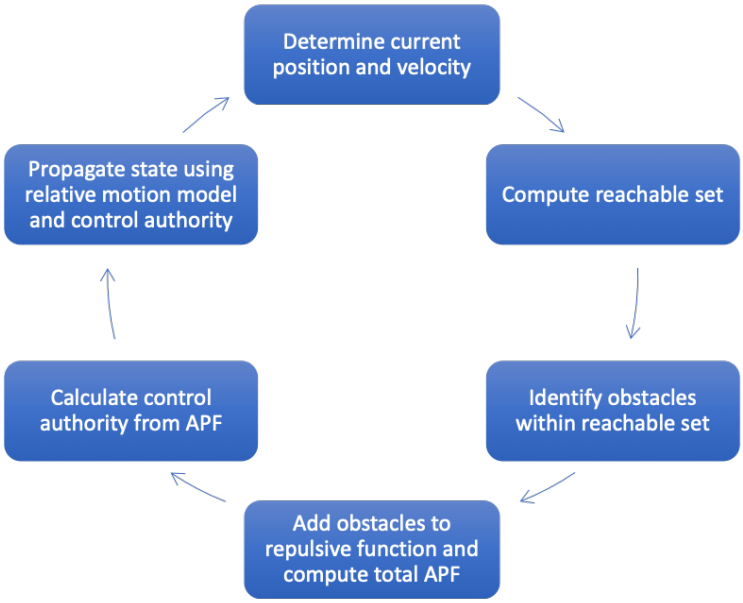

Figure 3.2. Flow chart of guidance methodology

The Figure of Merit for the Reach/APF algorithm is defined by the time series of the position histories, velocity histories, control histories, and a 2-D representation of the trajectory of the deputy spacecraft as it attempts rendezvous with the chief. Additionally, the computation time required to calculate the reach set, identify the nearest obstacles, and propagate the deputy spacecraft's position will be assessed for feasibility in an on-board autonomous guidance planning application. These metrics will support conclusions for the second and third research questions posed in this work from Section 1.2.1.

IV. Results and Analysis

This chapter details the scenarios designed to address the questions from Section 1.2.1 and the results from those experiments. The ellipsoidal reach set approximation method is applied in Section 4.1 using four relative motion models of various orbits. Section 4.2 establishes the environment for which the reach set computation is combined with the APF control method to compute the control authority required to rendezvous a deputy spacecraft with a chief spacecraft while avoiding obstacles.

4.1 Reach Set Variation Between Relative Motion Models

4.1.1 Test Instances

The orbits studied are LEO and GEO. LEO is modeled as an orbit with perigee of 700 km. GEO is modeled as an orbit with perigee of 35,786 km. The orbits are defined by the perigee radius to ensure a valid orbit around the Earth for the high eccentricity orbits. Orbital eccentricity is modeled starting at fully circular ($e = 0$) up to highly elliptical ($e = 0.7$). While not of significant influence on the variation in solutions generated by the various models, the remaining reference orbit Classical Orbital Elements (COEs) are listed in Table 4.1.

At LEO, the reach sets with time horizons of 1 minute and 10 minutes are analyzed, then the reach sets are analyzed at circular ($e = 0$) and highly elliptical ($e = 0.7$) obits for time horizons from 1 minute to 51 minutes. At GEO, the reach

Table 4.1. Classical orbital elements of the reference orbit (reach set variation)

Orbital Element	Symbol	Value	Unit
Inclination	i	45	Degrees
Right Ascension of the Ascending Node	Ω	20	Degrees
Argument of Perigee	ω	30	Degrees
Mean Anomaly	M_0	20	Degrees

sets with time horizons of 10 minutes and 100 minutes are analyzed, then the reach sets are analyzed at circular ($e = 0$) and highly elliptical ($e = 0.7$) orbits for time horizons from 1 minute to 501 minutes.

The four relative motion models analyzed are CW, SS, YA, and GA, which are discussed in more detail in Chapter II. A "true" reach set was not computed but would be a valuable addition as a benchmark for comparison. The CW model is valid for spacecraft operating in close-proximity about circular reference orbits. The SS motion model is an extension of the CW model with the addition of the J_2 perturbative force. The YA motion model provides a state transition matrix valid for all orbital eccentricities. The GA model can accurately represent relative motion with J_2 perturbations and can accurately represent the relative motion of elliptical reference orbits.

4.1.2 Reach Set Comparison at LEO

The reach set ellipsoids of each relative motion model are shown overlaid in Figures 4.1 through 4.3. Relative trajectories, propagated by each relative motion model with a random initial sample, are also shown in the figures. The shapes, volumes, and orientations of the reach set ellipsoids are analyzed using the Figures of Merit from Section 3.3, and are shown in Figures 4.4 through 4.6. The Euler angle of the semi-major axis of the reach set ellipsoid is shown in Figure 4.4. The volume of the reach set ellipsoid is shown in Figure 4.5. The trace of the reach set ellipsoid is shown in Figure 4.6.

The CW and SS models do not account for orbital eccentricity, and as such it is expected that the reach set ellipsoids do not change as the orbital eccentricity increases. The Euler angle of the semi-major axis remains constant. While the Euler angle for the SS model varies from the other models for the 1 minute interval case, the

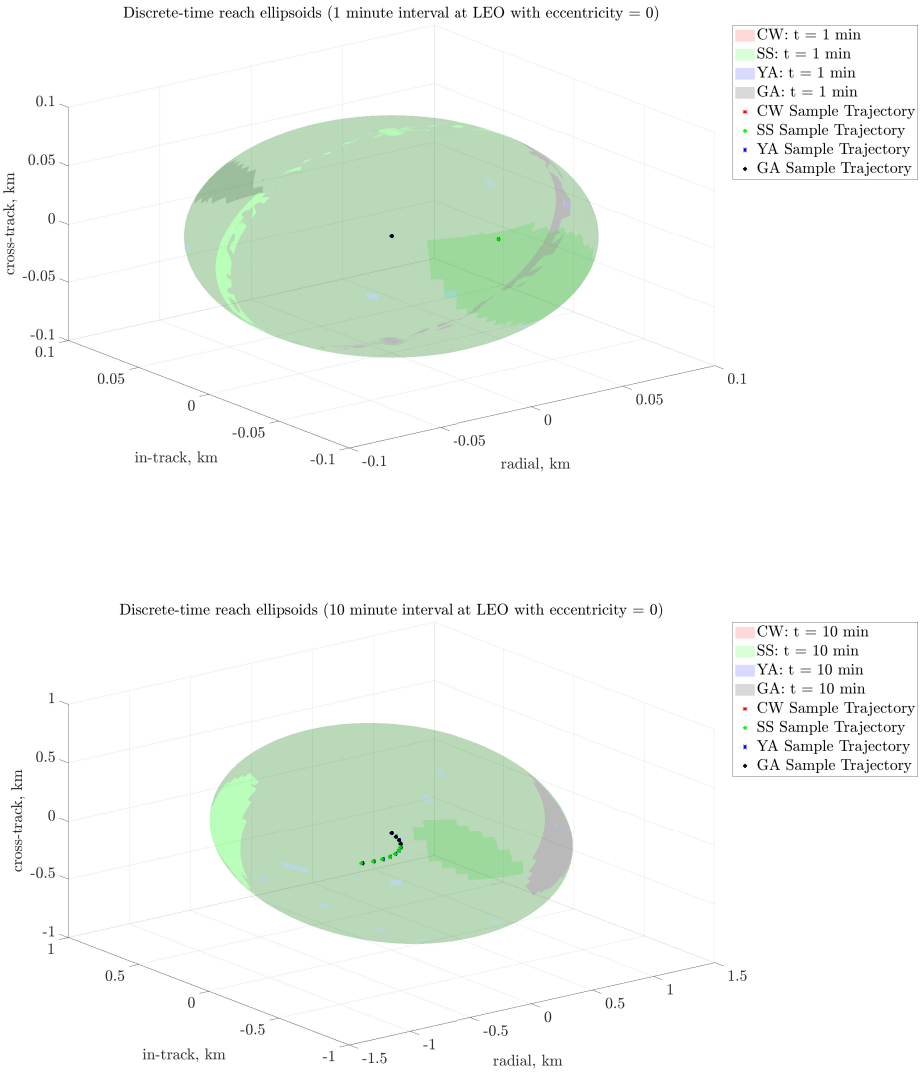

Figure 4.1. Reach set with all models overlaid in LEO ($e = 0$)
Top: 1 min interval, Bottom: 10 min interval

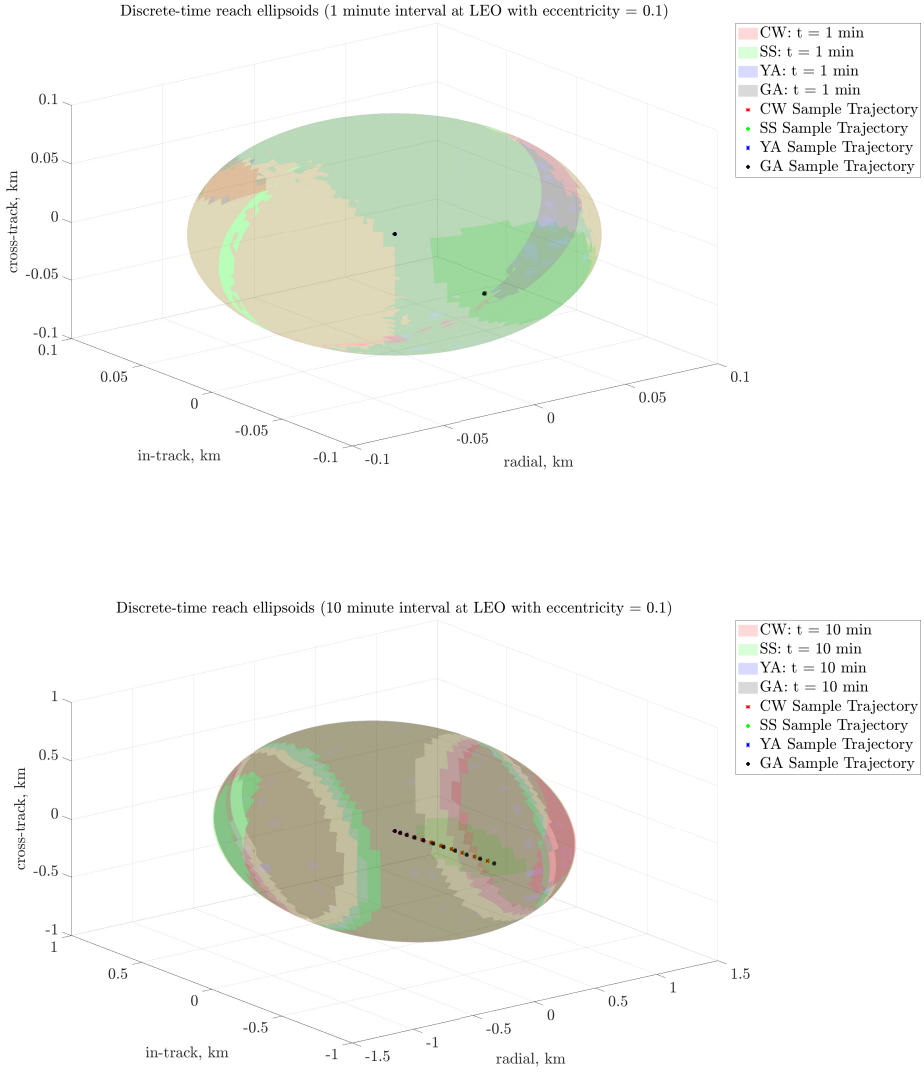

Figure 4.2. Reach set with all models overlaid in LEO ($e = 0.1$)
Top: 1 min interval, Bottom: 10 min interval

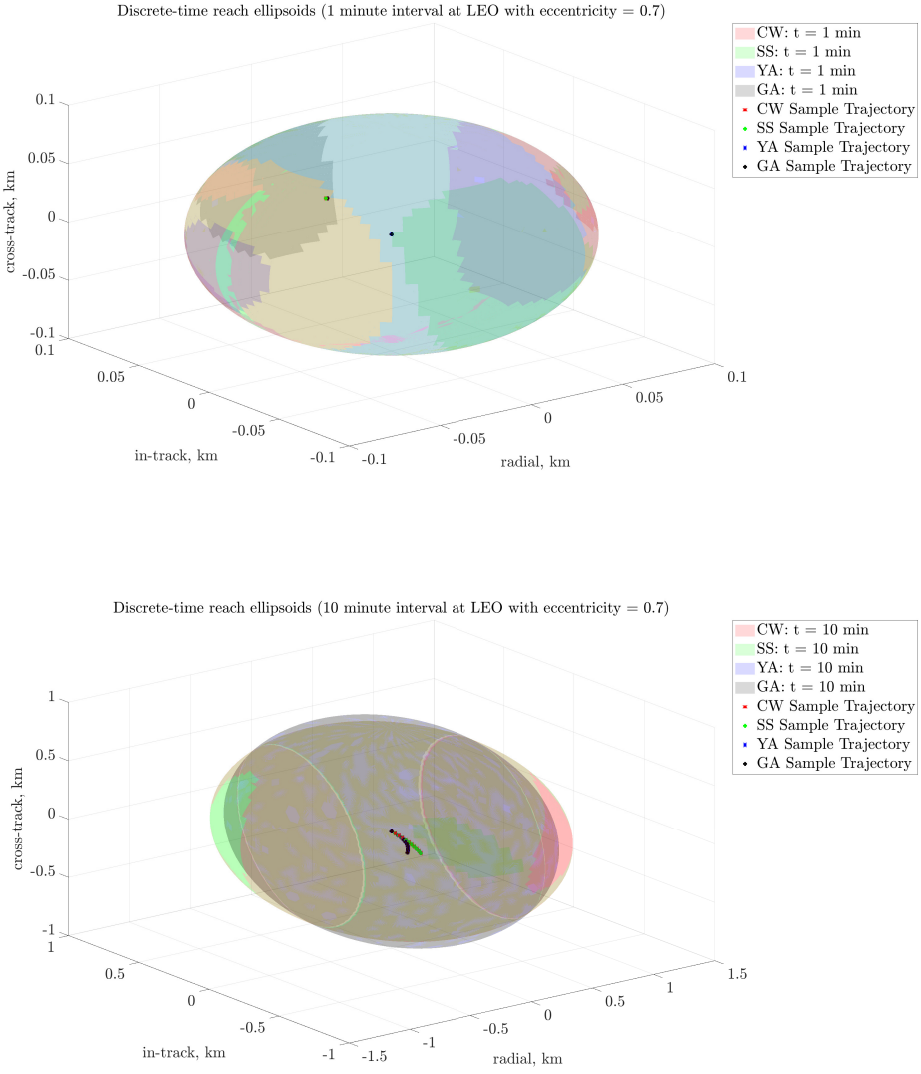

Figure 4.3. Reach set with all models overlaid in LEO ($e = 0.7$)
Top: 1 min interval, Bottom: 10 min interval

trace value is very close for all the models, indicating the overall shape of the reach sets are very similar. The volume of each model at the 1 minute interval supports that the reach sets for all four models at a 1 minute interval at LEO are very similar.

The YA and GA models can accurately model relative motion for elliptical orbits, thus the reach set ellipsoid is variate as the orbital eccentricity increases. GA, however, also accounts for J_2 perturbations. From the comparisons between the CW and SS reach sets above where the J_2 perturbation had little impact on the reach set, it can be hypothesized that the YA and GA models will have very similar reach set ellipsoids. Figures 4.4 through 4.6 support this hypothesis where the semi-major axis Euler angle, ellipsoid volume, and ellipsoid trace are nearly identical between the YA and GA models throughout all eccentricities. The semi-major axis Euler angles of the GA model deviate in Figure 4.4, however this is due to numerical precision error. Discounting the numerical precision error, the eigenvectors of the reach set ellipsoids of the YA and GA models are nearly identical for all eccentricities, and thus the Euler angles are also nearly identical.

Figure 4.7 shows the computation time required to calculate the reach set for each relative motion model at each eccentricity. All computations are performed on a Quad-Core Intel Core i5-6500 3.2 GHz processor with 16 GB 2133 MHz DDR4 memory. The computation time of the reach set for each model at both time horizons is very low, mostly on the order of milliseconds. From eccentricities 0 to 0.1, each model's computation time is slightly higher and the GA model is significantly higher, comparatively, up to 0.13 seconds. The reason for this increase is unclear and may warrant further investigation depending on mission requirements. Overall, despite the slight increases in computation time at eccentricities less than 0.1, the computation times demonstrate strong potential for use in on-board, real-time guidance applications.

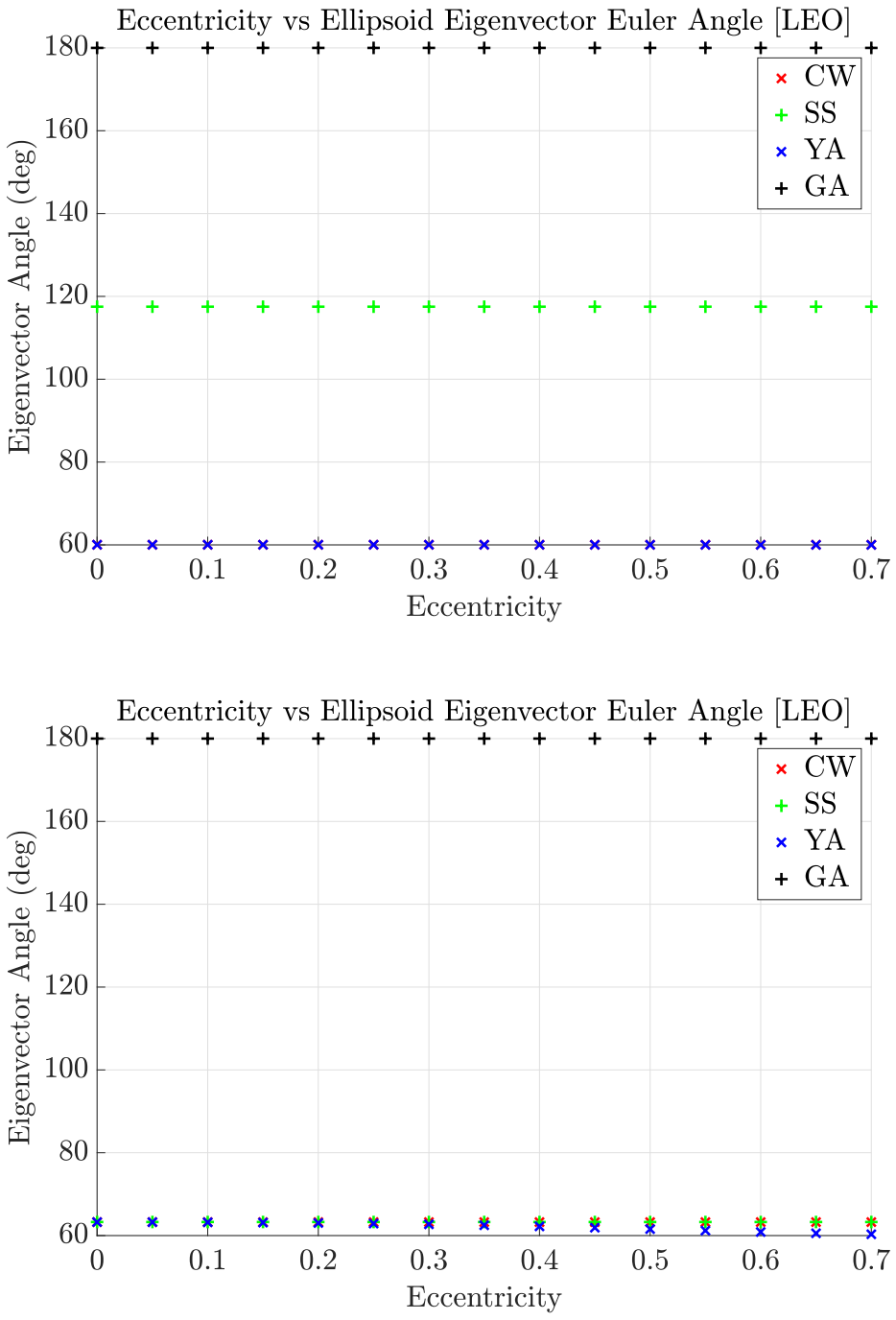

Figure 4.4. Euler angle of reach set ellipsoid semi-major axis (LEO)
Top: 1 min interval, Bottom: 10 min interval

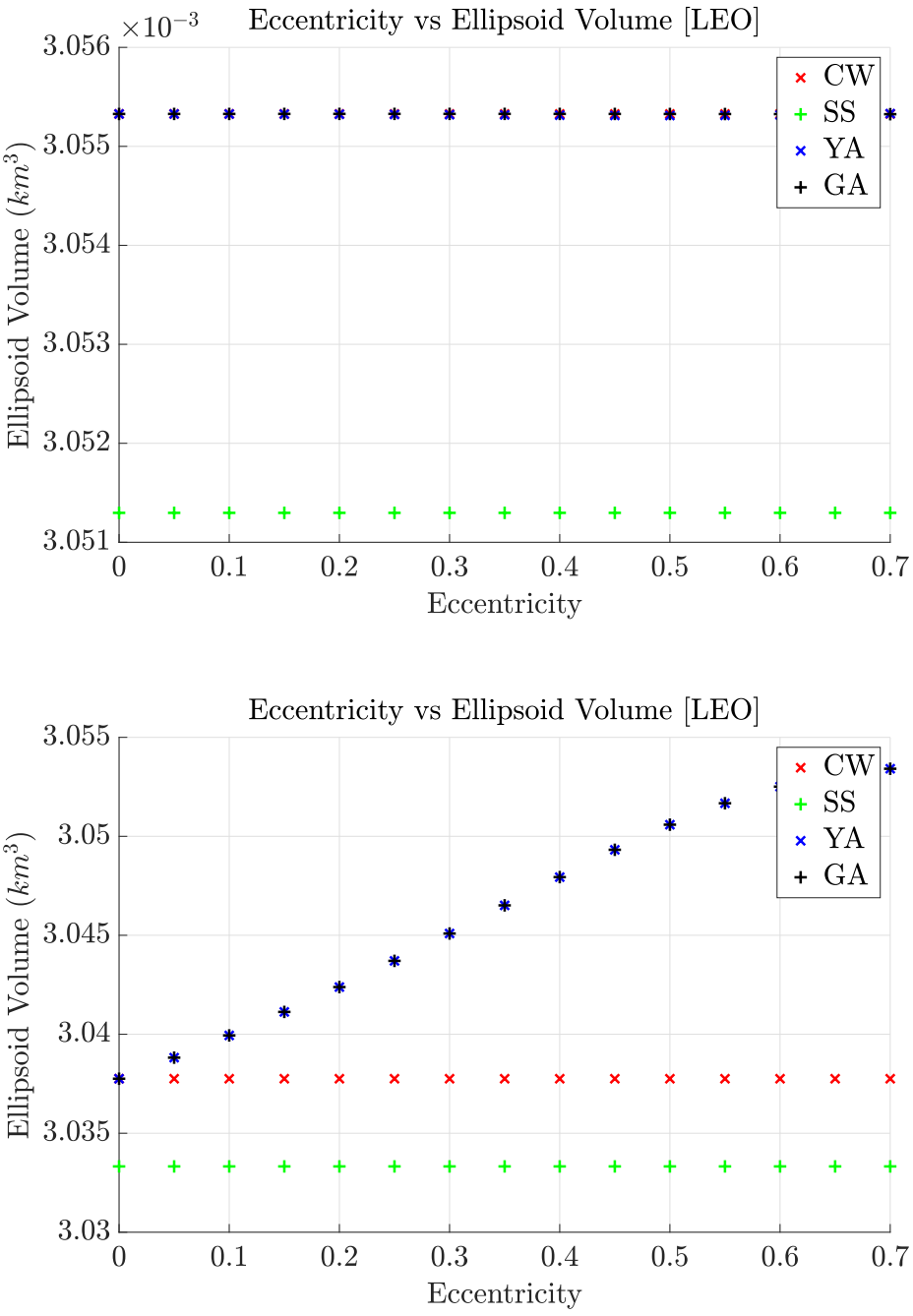

Figure 4.5. Volume of reach set ellipsoid (LEO)
Top: 1 min interval, Bottom: 10 min interval

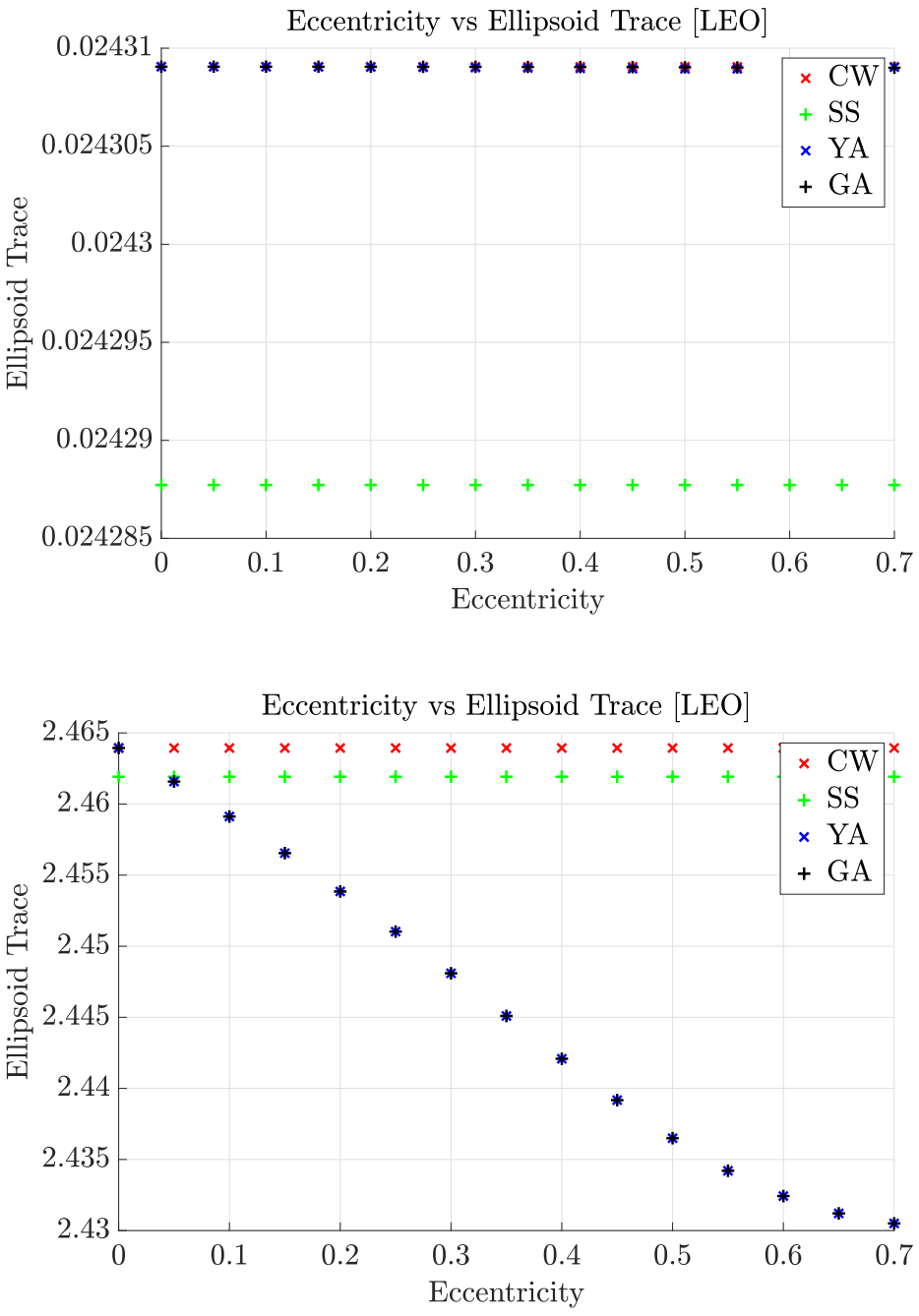

Figure 4.6. Trace of reach set ellipsoid (LEO)
Top: 1 min interval, Bottom: 10 min interval

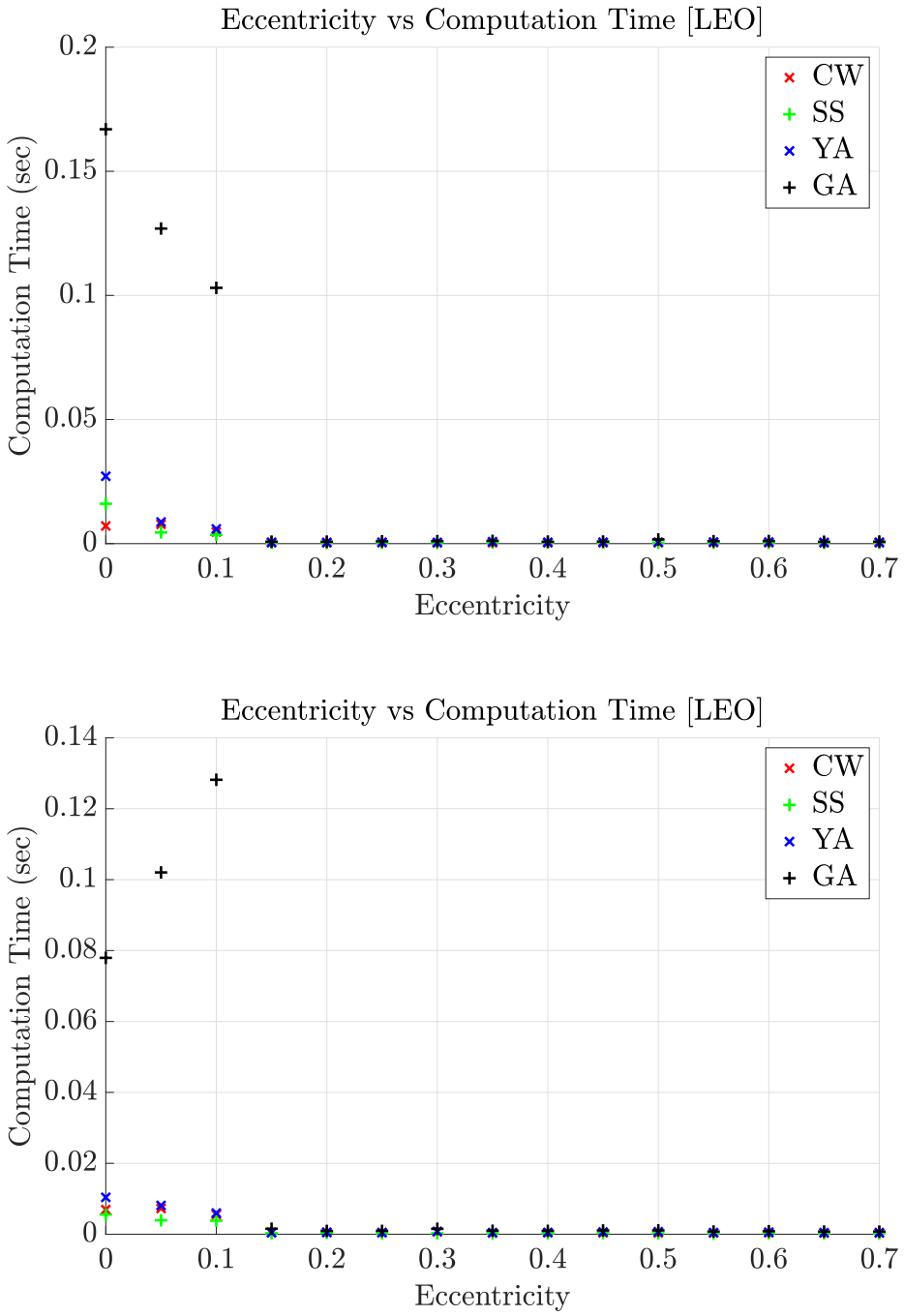

Figure 4.7. Reach set computation time (LEO)
Top: 1 min interval, Bottom: 10 min interval

Figures 4.8 through 4.11 show the reach set metrics when compared to the time horizon for circular and highly elliptical orbits. All four models are linearized to be applicable for a short time horizon, therefore it can be expected that as the time horizon grows, the modeling error should grow. This is depicted at both eccentricities, particularly beyond 30 minutes. For the highly elliptical orbit, the modeling error by the CW and SS models, due to not accounting for eccentricity, becomes dramatically apparent after 30 minutes where the CW and SS models underapproximate the reach set as compared to the YA and GA models.

Computationally speaking, each of the four models presented here show strong potential for on-board, real-time guidance application but the impact of the orbital eccentricity on the reach set demonstrates a clear need to utilize an appropriate relative motion model. The YA and GA models are valid for all eccentricities, $0 \leq e < 1$, therefore it is feasible to employ either of these models for applications in LEO for any eccentricity and the system will have a computationally efficient method for verifying object detection and control verification for guidance planning in spacecraft RPO applications.

Contrarily, the CW and SS models do not provide an accurate representation of the reach set ellipsoid for high eccentricities for longer time horizons. For short time horizons, the differences between the reach set solutions may be small enough to

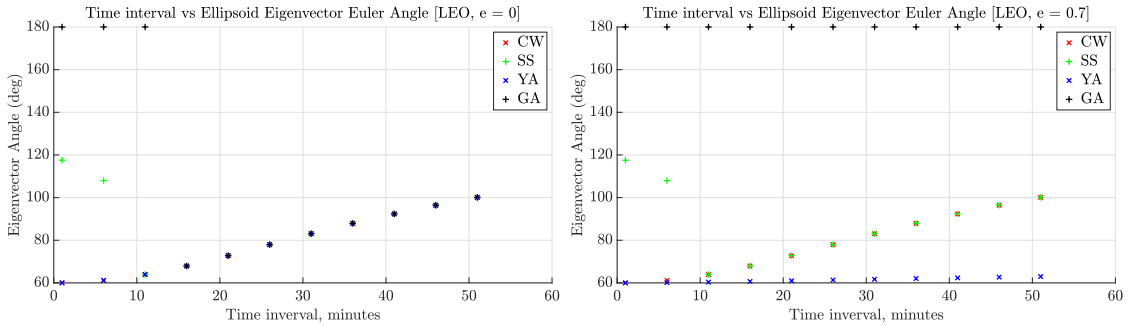

Figure 4.8. Euler angle of reach set ellipsoid semi-major axis for various time intervals (LEO) Left: $e = 0$, Right: $e = 0.7$

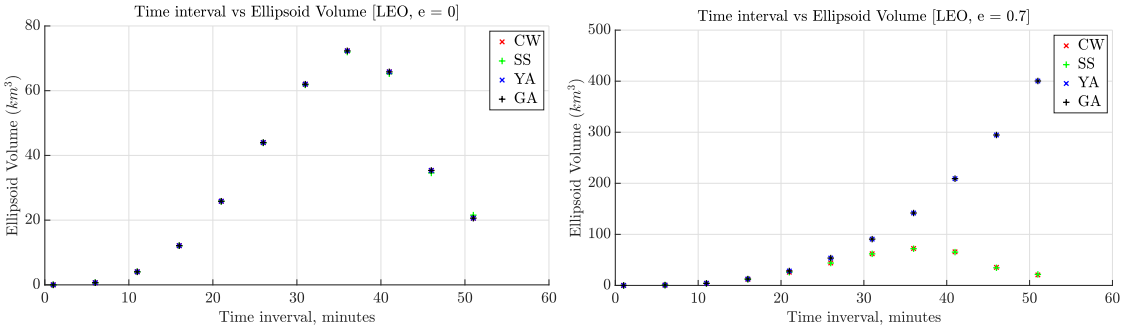

Figure 4.9. Volume of reach set ellipsoid for various time intervals (LEO)
Left: $e = 0$**, Right:** $e = 0.7$

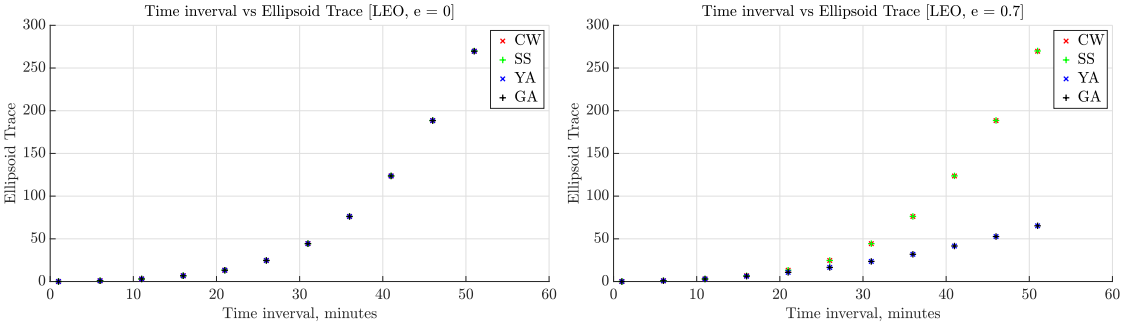

Figure 4.10. Trace of reach set ellipsoid for various time intervals (LEO)
Left: $e = 0$**, Right:** $e = 0.7$

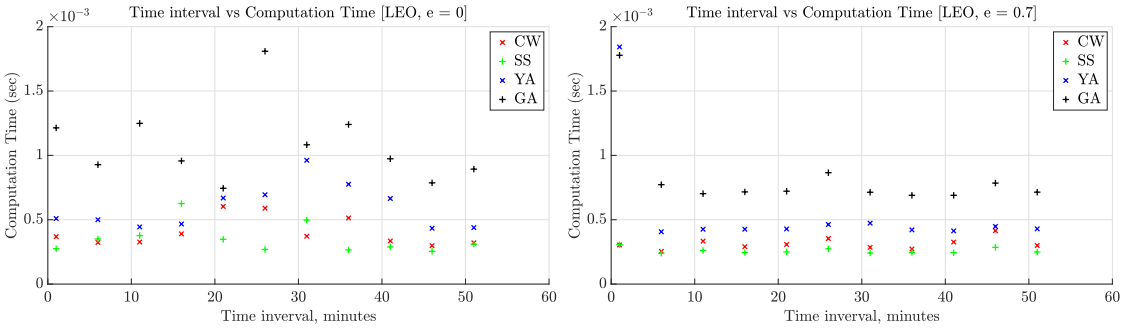

Figure 4.11. Reach set computation time for various time intervals (LEO)
Left: $e = 0$**, Right:** $e = 0.7$

be negligible, allowing for some modeling trade space if computational resources are extremely tight. At low eccentricities, the orientation of the CW and SS reach set ellipsoids may be similar enough to the YA and GA model for certain applications, but as the eccentricity increases, the orientation of the CW and SS reach set ellipsoids deviate from the YA and GA models at an eccentricity of 0.7 and grows directly with the time horizon. Although the orientation of the CW and SS reach set ellipsoids may remain similar enough at low eccentricities for some applications, the CW and SS models under-approximate the reach set compared to the YA and GA solutions by volume. In order to encompass all possible final states and ensure proper control verification or all nearby obstacles are accounted for, the reach set must be over-approximated instead of under-approximated. For these reasons, the CW and SS relative motion models are not suitable for approximating the reach set at higher eccentricities at LEO unless the time horizon is sufficiently small.

4.1.3 Reach Set Comparison at GEO

The reach set ellipsoids of each relative motion model are shown overlaid in Figures 4.12 through 4.14. Relative trajectories, propagated by each relative motion model with a random initial sample, is also shown in the figures. The shapes, volumes, and orientations of the reach set ellipsoids are analyzed using the Figures of Merit from Section 3.3, and are shown in Figures 4.15 through 4.17. The Euler angle of the semi-major axis of the reach set ellipsoid is shown in Figure 4.15. The volume of the reach set ellipsoid is shown in Figure 4.16. The trace of the reach set ellipsoid is shown in Figure 4.17.

The CW and SS models do not account for orbital eccentricity, and as such, similar to the case at LEO, it is expected that the reach set ellipsoids do not change as the orbital eccentricity increases. The Euler angle of the semi-major axis, volume, and

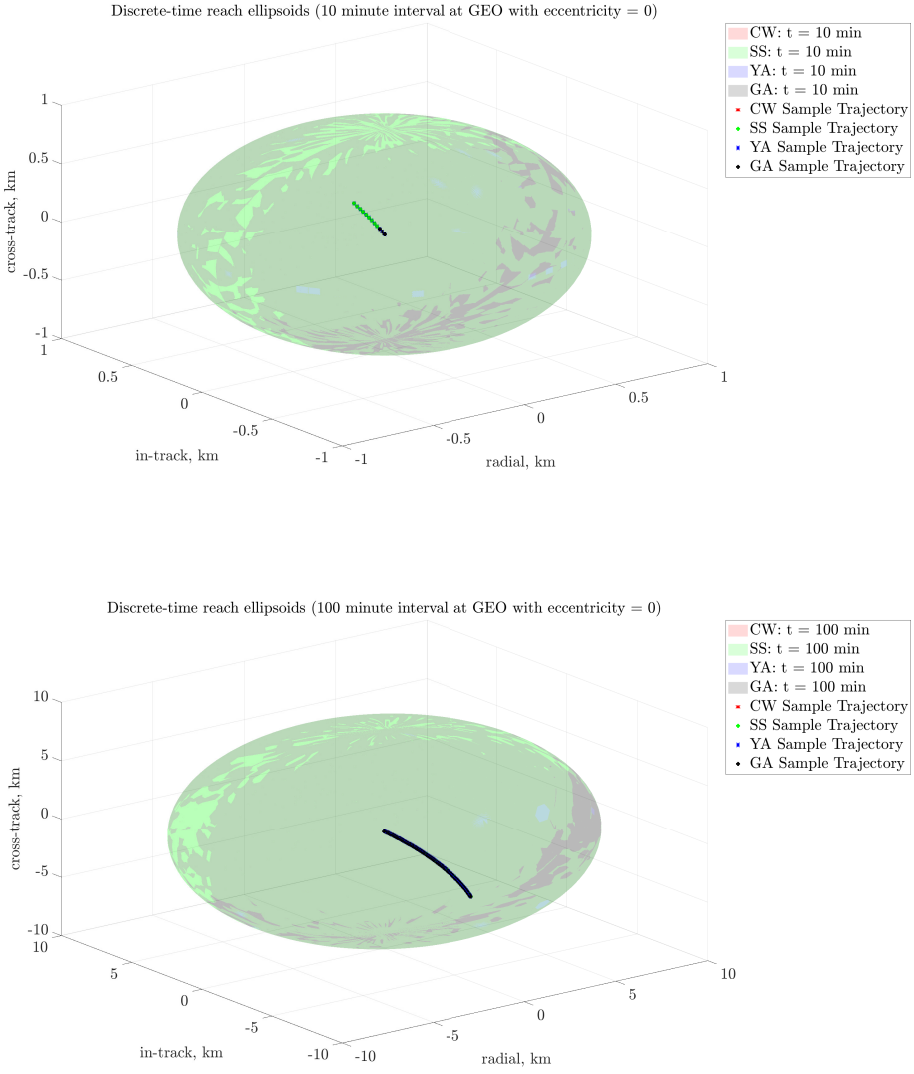

Figure 4.12. Reach set with all models overlaid in GEO ($e = 0$)
Top: 10 min interval, Bottom: 100 min interval

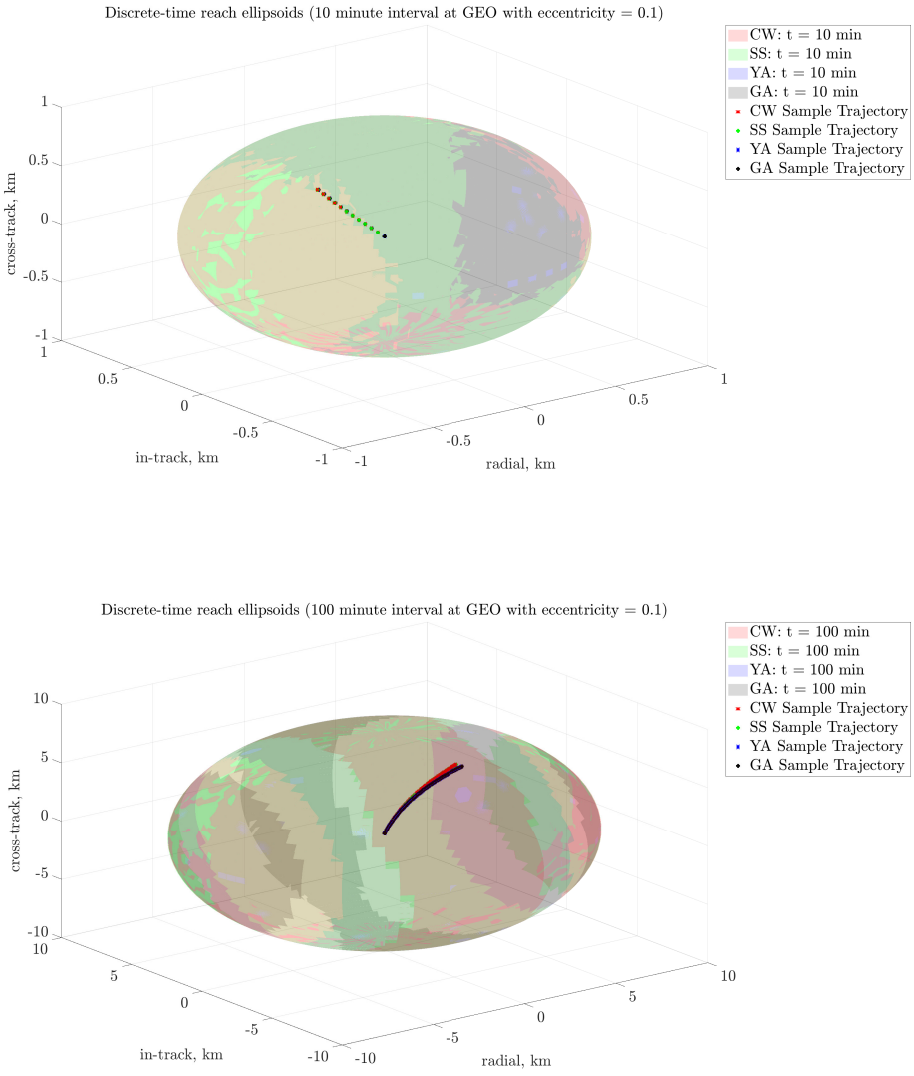

Figure 4.13. Reach set with all models overlaid in GEO ($e = 0.1$)
Top: 10 min interval, Bottom: 100 min interval

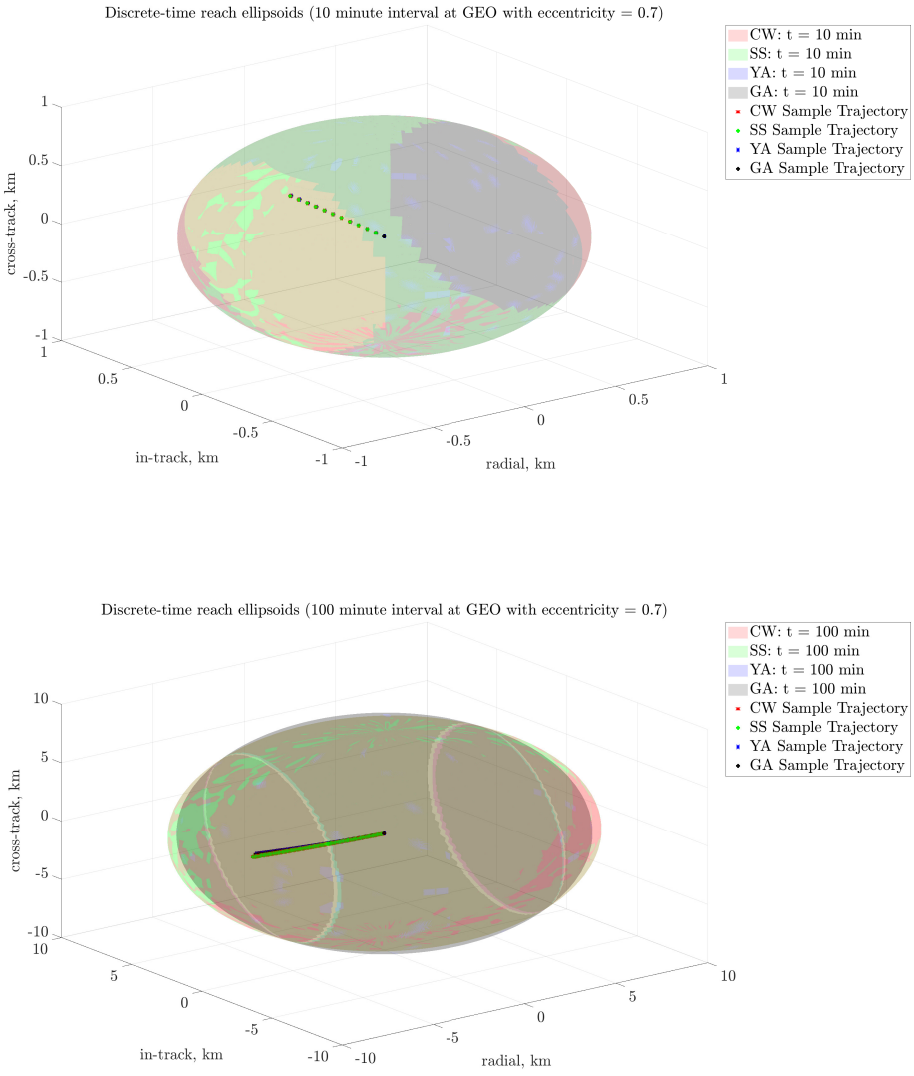

Figure 4.14. Reach set with all models overlaid in GEO ($e = 0.7$)
Top: 10 min interval, Bottom: 100 min interval

trace of the reach set ellipsoids for the CW and SS models remain constant. The differences shown in the figures between the CW and SS model reach set ellipsoids is very small, down to the third and fourth decimal. The influence of J_2 perturbations at GEO are much smaller than at LEO, therefore it is expected that the CW and SS models produce extremely similar reach set ellipsoids.

The YA and GA models can accurately model relative motion for elliptical orbits, thus the reach set ellipsoid is variate as the orbital eccentricity increases. With the influence of J_2 perturbations having been concluded to be minimal, and with J_2 perturbations being much smaller at GEO, the reach set ellipsoid YA and GA models have very similar reach set ellipsoids. Figures 4.15 through 4.17 support this hypothesis where the semi-major axis Euler angle, ellipsoid volume, and ellipsoid trace are nearly identical between the YA and GA models throughout all eccentricities. The semi-major axis Euler angles of the GA model deviate in Figure 4.15 for all eccentricities, however this is again due to numerical precision error. Discounting the numerical precision error, the eigenvectors of the reach set ellipsoids of the YA and GA models are nearly identical for all eccentricities, and thus the Euler angles are also nearly identical. When evaluated over the time horizon of 10 minutes, the reach sets of all four models are nearly identical. When calculated out to 100 minutes, the error propagations begin to show as the CW and SS models underapproximate the reach sets for higher eccentricities.

Figure 4.18 shows the computation time required to calculate the reach set for each relative motion model at each eccentricity. All computations are performed on a Quad-Core Intel Core i5-6500 3.2 GHz processor with 16 GB 2133 MHz DDR4 memory. As with the case of an orbit in LEO, the computation time of the reach set for each model is very low, mostly on the order of milliseconds. From eccentricities 0 to 0.1, each model's computation time is slightly higher and the GA model is

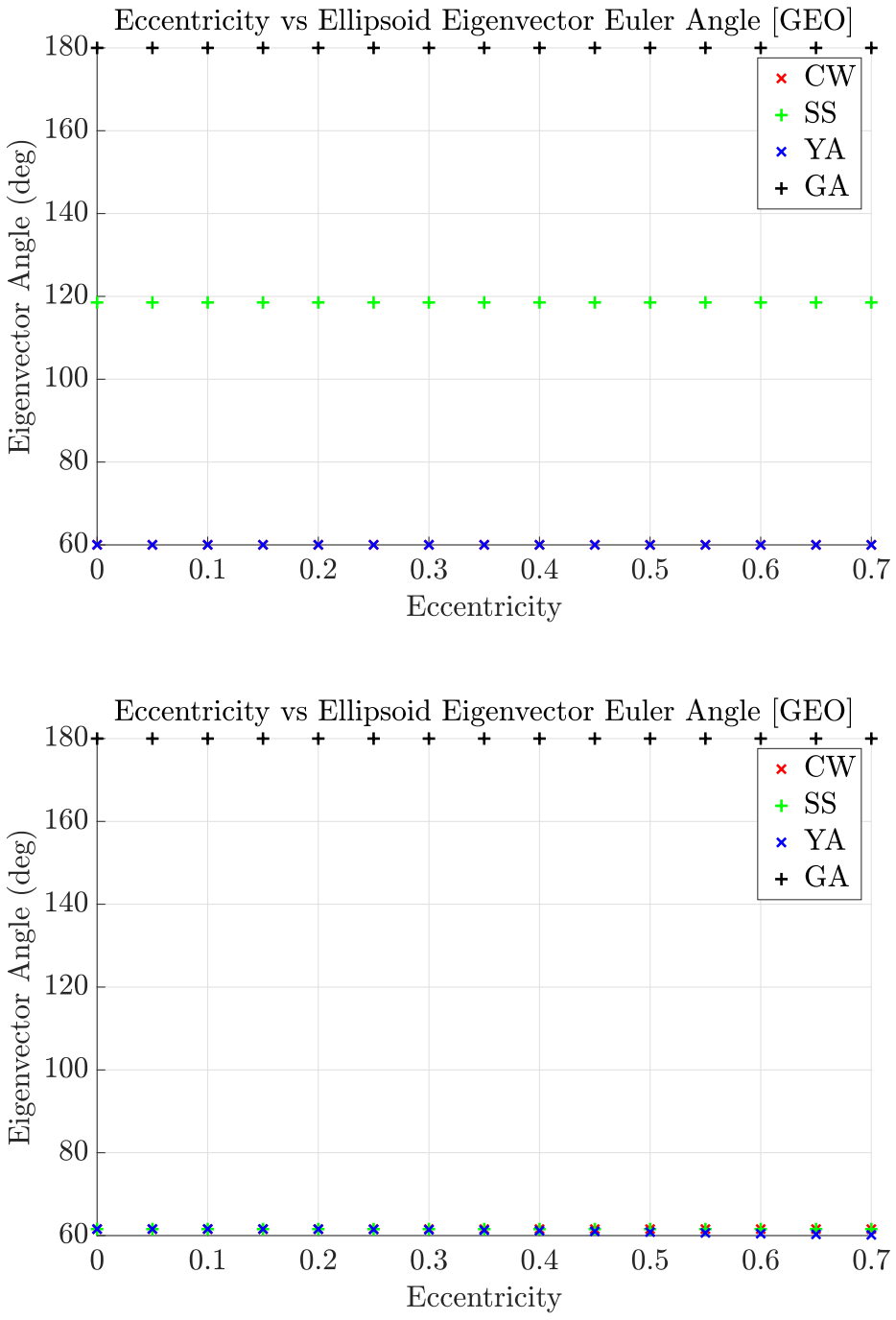

Figure 4.15. Euler angle of reach set ellipsoid semi-major axis (GEO)
Top: 10 min interval, Bottom: 100 min interval

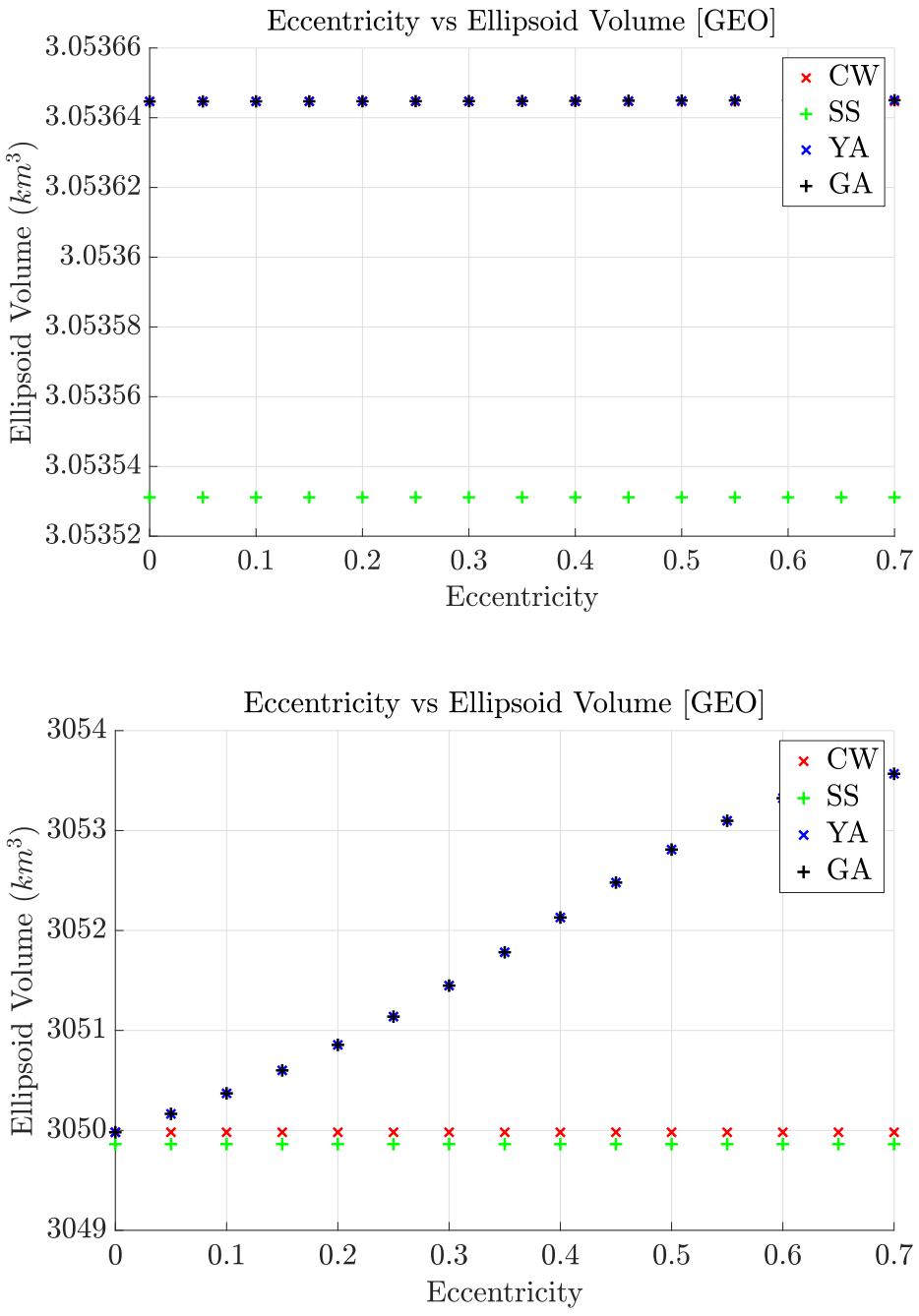

Figure 4.16. Volume of reach set ellipsoid (GEO)
Top: 10 min interval, Bottom: 100 min interval

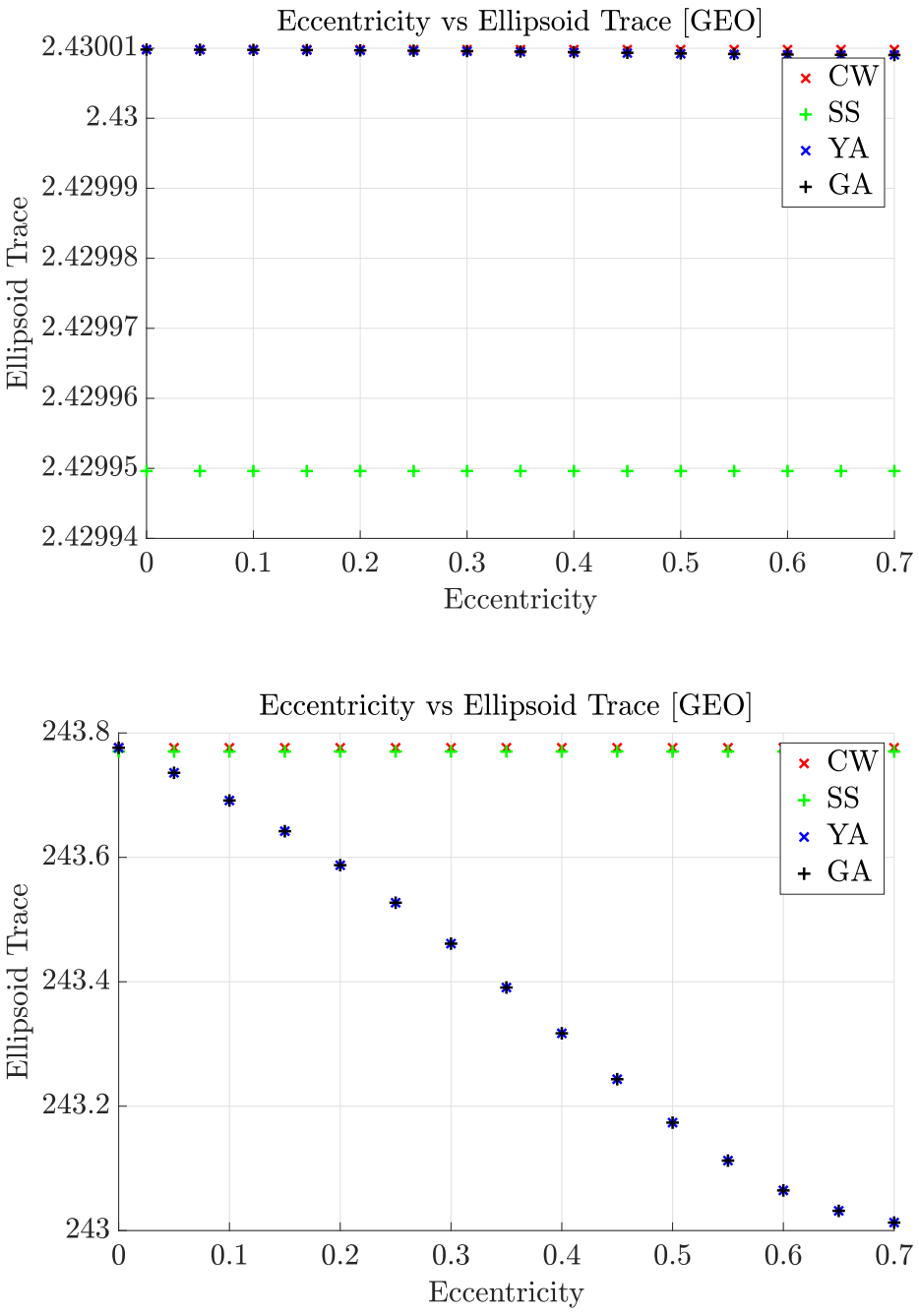

Figure 4.17. Trace of reach set ellipsoid (GEO)
Top: 10 min interval, Bottom: 100 min interval

significantly higher, comparatively, up to 0.12 seconds. Overall, despite the slight increases in computation time at eccentricities less than 0.1, the computation times demonstrate strong potential for use in on-board, real-time guidance applications.

Figures 4.19 through 4.22 show the reach set metrics when compared to the time horizon for circular and highly elliptical orbits. All four models are linearized to be applicable for a short time horizon, therefore it can be expected that as the time horizon grows, the modeling error should grow. While this error is not apparent over this time interval for the circular GEO orbit, this is depicted for the highly elliptical GEO orbit, particularly beyond 300 minutes. For the highly elliptical orbit, the modeling error by the CW and SS models due to not accounting for eccentricity becomes apparent after 300 minutes where the CW and SS models underapproximate the reach set as compared to the YA and GA models.

Similar to the case at LEO, computationally speaking, each of the four models presented here show strong potential for on-board, real-time guidance application but the impact of the orbital eccentricity on the reach set demonstrates a clear need to utilize an appropriate relative motion model. The YA and GA models are valid for all eccentricities, $0 \leq e < 1$, therefore it is feasible to employ either of these models for applications in GEO for any eccentricity and the system will have a computationally efficient method for verifying object detection and control verification for guidance planning in spacecraft RPO applications.

Also similar to the case at LEO, the CW and SS models may provide an accurate representation of the reach set ellipsoid even for high eccentricities only over shorter time horizons. Although the orientation of the CW and SS reach set ellipsoids appear to vary significantly, the volume and trace, as shown in Figures 4.16 and 4.17, vary only to third decimal across all eccentricities. These values demonstrate that the shape of the reach set ellipsoids are very similar. While the CW and SS models also

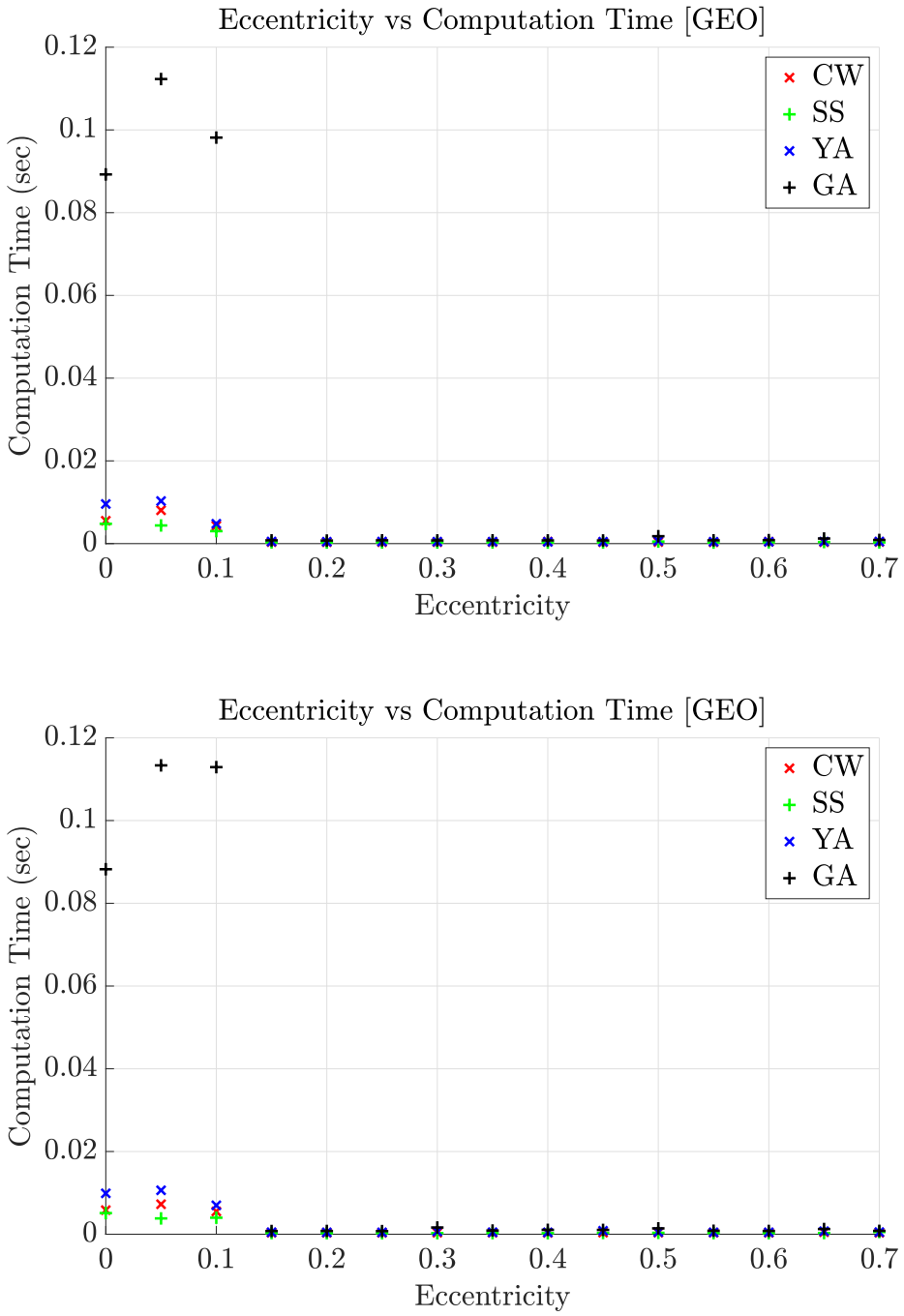

Figure 4.18. Reach set computation time (GEO)
Top: 10 min interval, Bottom: 100 min interval

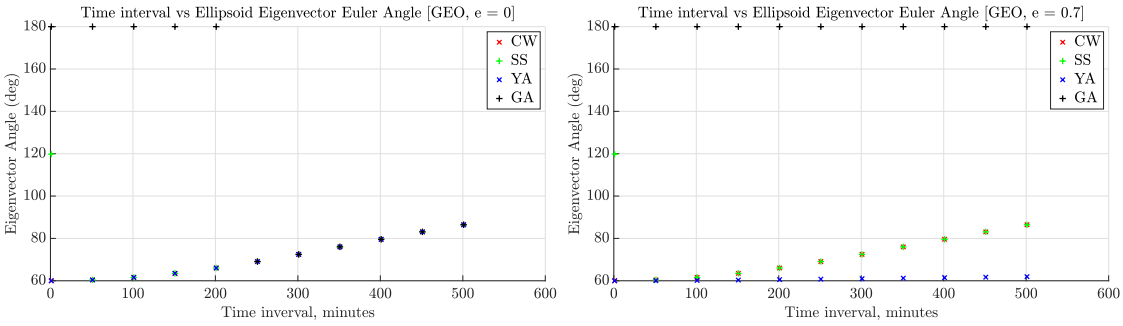

Figure 4.19. Euler angle of reach set ellipsoid semi-major axis for various time intervals (GEO) Left: $e = 0$, Right: $e = 0.7$

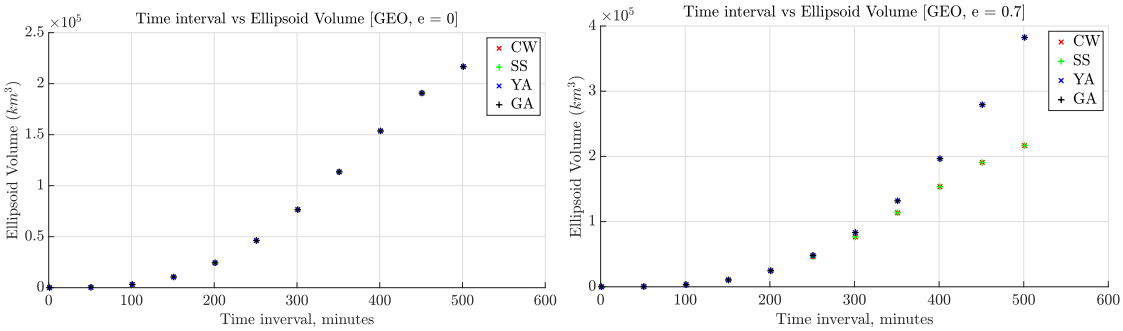

Figure 4.20. Volume of reach set ellipsoid for various time intervals (GEO) Left: $e = 0$, Right: $e = 0.7$

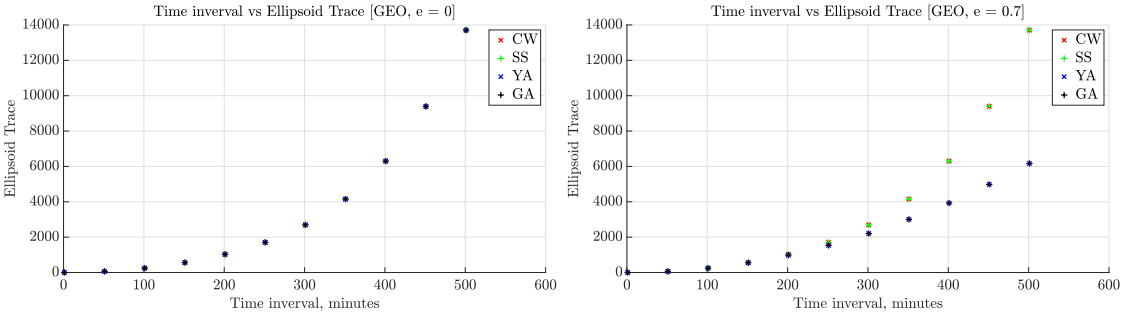

Figure 4.21. Trace of reach set ellipsoid for various time intervals (GEO) Left: $e = 0$, Right: $e = 0.7$

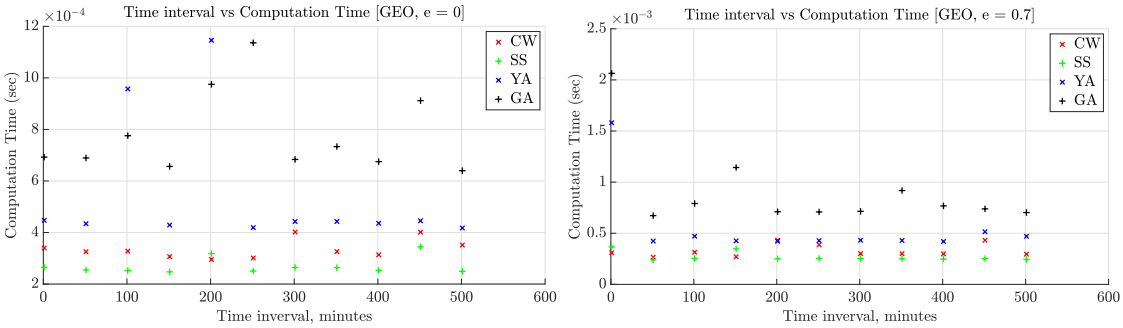

Figure 4.22. Reach set computation time for various time intervals (GEO)
Left: $e = 0$**, Right:** $e = 0.7$

underestimate the reach set compared to the YA and GA models over the 10 minute time horizon, the difference is at most approximately 0.0001 km^3 at eccentricity $e = 0.7$. The 100 minute time horizon shows greater deviation in the reach set between the models, but the capability to rapidly compute the reach set for each model would likely negate the necessity for such a large time horizon. Therefore, the CW and SS models may be suitable for approximating the reach set at higher eccentricities at GEO and provide a means for ensuring proper control verification or all nearby obstacles are accounted for.

4.2 Trajectory Planning using Reachability Analysis with APFs

4.2.1 Test Instances

Several scenarios are simulated to demonstrate the feasibility of implementing a trajectory planning algorithm that leverages reachability analysis with APFs for collision avoidance. The ellipsoidal reach set approximations are computed utilizing the CW relative motion model. While this algorithm can be applied for any target location, the target destination for each scenario is the chief spacecraft at the origin of the relative Hill reference frame. The deputy spacecraft is initiated in an NMC orbit, depending on the scenario. Circular orbits at both LEO and GEO are explored as well as the impact of the shape of the APF on the guidance solution. LEO is

defined at an altitude of 700 km above the Earth and GEO is defined at an altitude of 35786 km above the Earth. The orbital elements for both orbits are the same and summarized in Table 4.2, and are arbitrary.

The three main cases studied are:

1. A strong attractive potential function with relatively static obstacles.

2. A weak attractive potential function with relatively static obstacles.

3. Obstacles moving on an NMC orbit.

In all cases, the cross-track motion is ignored since it is decoupled from the radial and in-track motion in the CW relative motion model. Each simulation is run for a maximum duration of two periods, that is, the deputy is given a maximum of two periods to complete the rendezvous before the computation aborts. This limitation is arbitrary, and is set for the purposes of this research. In real world applications, this bound may be determined by mission constraints such as required time to rendezvous. The maximum magnitude of control is bounded at 1 m/s. The size of the obstacles is set to a diameter of 10 m and are initiated between $1/10^{\text{th}}$ and $9/10^{\text{th}}$ of the radius of the deputy's initial NMC orbit. The diameter of the obstacles serves as the keep-out zone for the deputy spacecraft to avoid during the rendezvous operation. A position error and velocity error is defined for the reachability analysis at 1 m and 0.5 m/s, respectively.

Several other independent variables include the interval between calculations of

Table 4.2. Classical orbital elements of the reference orbit (trajectory planning)

Orbital Element	Symbol	Value	Unit
Eccentricity	e	0	Unitless
Inclination	i	45	Degrees
Right Ascension of the Ascending Node	Ω	20	Degrees
Mean Anomaly	M_0	20	Degrees

the trajectory and control, the interval between calculations of the reach sets, the number of obstacles, and whether the obstacles detected are static in the relative reference frame or in an NMC orbit around the chief spacecraft. These variables are defined for each case studied in the following sections.

For defining the artificial potential function, in Equations 3.12 and 3.13, $\boldsymbol{P}$ is set per each scenario while $k_a = 0.002$, $\psi_i = 300$, $\sigma_i = 9/16 r_{obs,i}^2$, and $\boldsymbol{N}$ is set to create a circular obstacle keep-out zone with $\boldsymbol{I}_{2x2}$ [48].

All computations are performed on a Quad-Core Intel Core i5-6500 3.2 GHz processor with 16 GB 2133 MHz DDR4 memory.

4.2.2 Case 1: Strong Attractive Potential Function

A strong attractive function with respect to the repulsive function is demonstrated in GEO. The deputy spacecraft is initialized in a NMC relative orbit 100 m from the chief spacecraft. The maneuver begins at $\beta = 30°$ in the NMC orbit with nine relatively static obstacles. The interval between trajectory calculations is 1 minute. The reach set is calculated every 10^{th} calculation, or every 10 minutes.

The shape of the attractive potential function is determined by the shaping matrix $\boldsymbol{P}$. Increasing the shape matrix $\boldsymbol{P}$ increases the height of the paraboloid, creating a large paraboloid with a steep gradient.

The attractive potential shape matrix $\boldsymbol{P}$ is

$$\boldsymbol{P} = \begin{bmatrix} 2 \times 10^4 & 0 \\ 0 & 2 \times 10^4 \end{bmatrix} \tag{4.1}$$

which creates a tall attractive potential comparatively with respect to the repulsive potential function, as shown in Figures 4.23.

Figure 4.24 shows the trajectory of the deputy spacecraft as it attempts to ren-

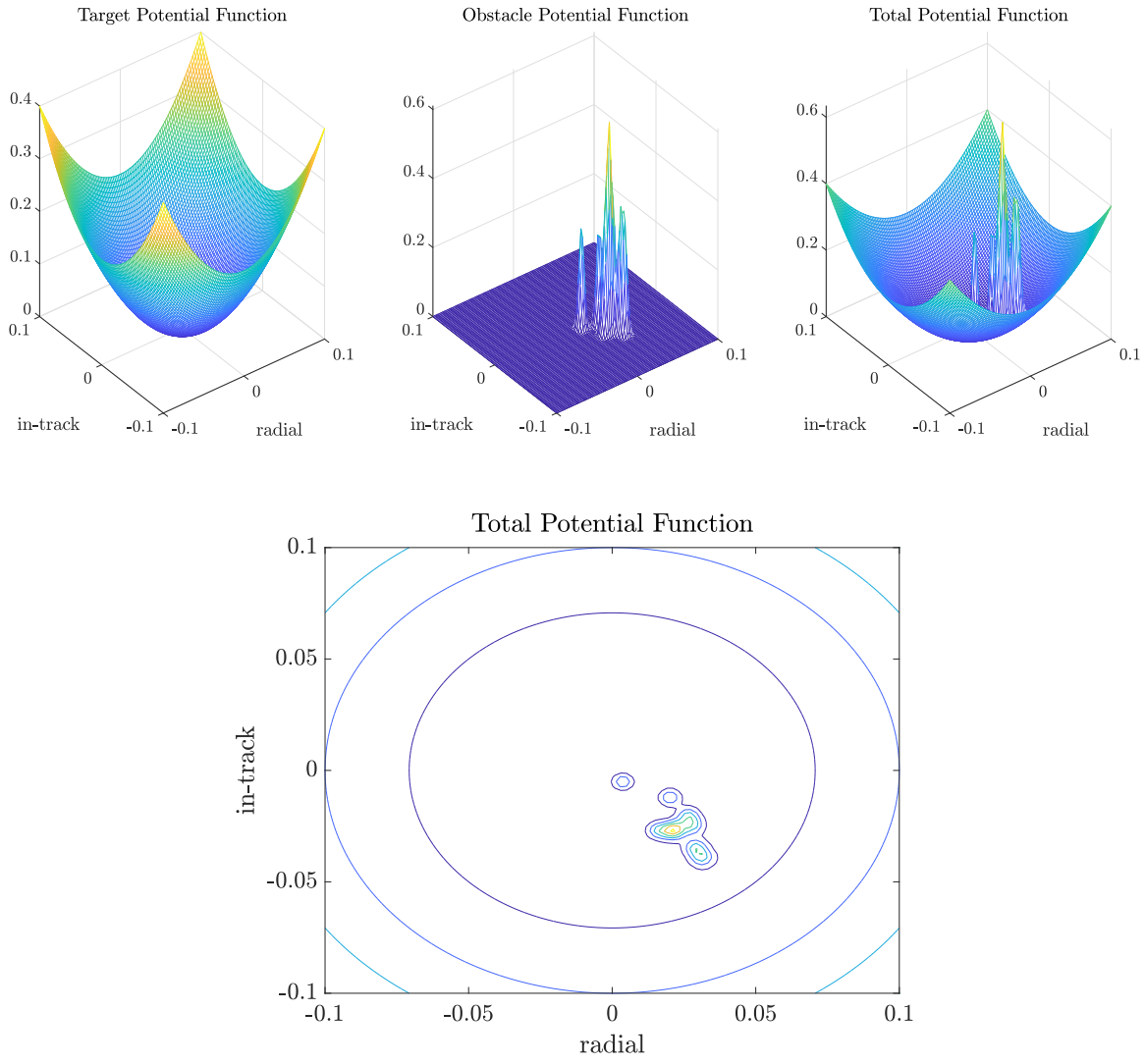

Figure 4.23. APF with a strong attractive potential

dezvous with the chief spacecraft by following the gradient of the APF. The state and control histories are shown in Figures 4.25 and 4.26. The trajectory and state history plots show the spacecraft does not rendezvous with the chief. Instead, the trajectory hops over or around the global minimum at the target destination. The algorithm is halted early because a state solution exceeded an arbitrary position bound set by the author of five times the initial starting distance from the chief spacecraft. Without this, poorly tuned APFs tended to diverge further as the APF gradient grew larger and larger the further from the origin the deputy spacecraft moved. The control his-

tories in Figure 4.26 show that these maneuvers often require close to the maximum available control input, 1 m/s, to be accomplished.

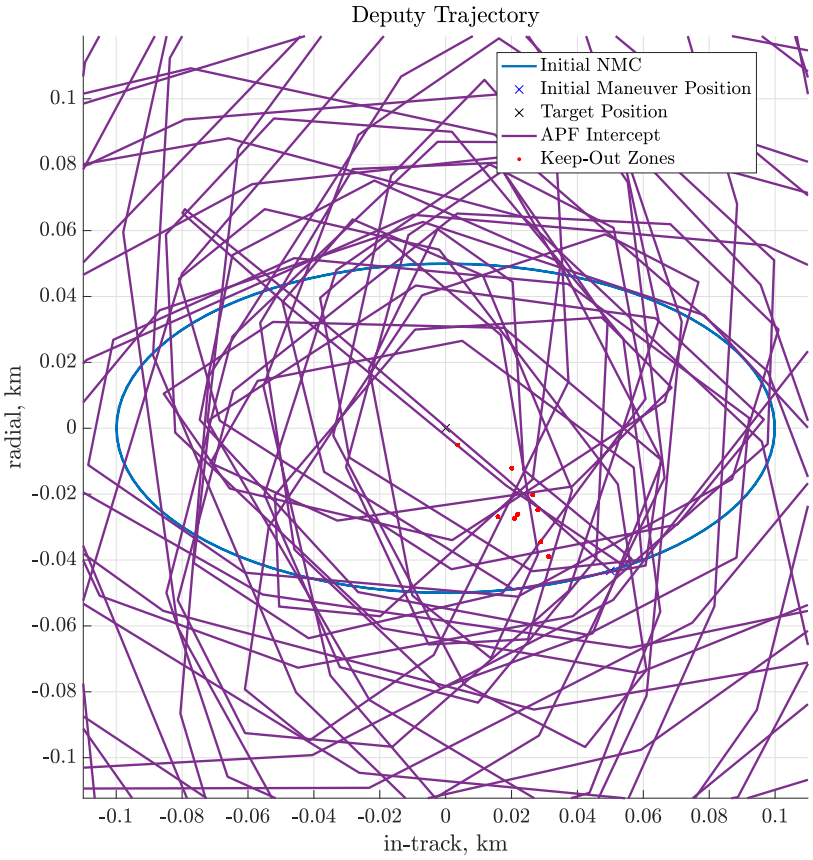

Figure 4.24. Trajectory with a strong attractive potential

Computation time is documented in Figure 4.27. To evaluate the feasibility of computing reach sets and guidance planning together autonomously and in real-time, it is required that the maneuver be calculated prior to the required maneuver time. As mentioned, the trajectory and control is computed for every minute, therefore this algorithm must be able to compute the trajectory in under 1 minute, including when the reach sets are being calculated and the obstacles are being identified.

Figure 4.27 shows all computations are feasible, with zero calculations taking longer to compute than the required one minute. The short computation times are around 10-40 microseconds and correspond to scenarios where the reach set is not

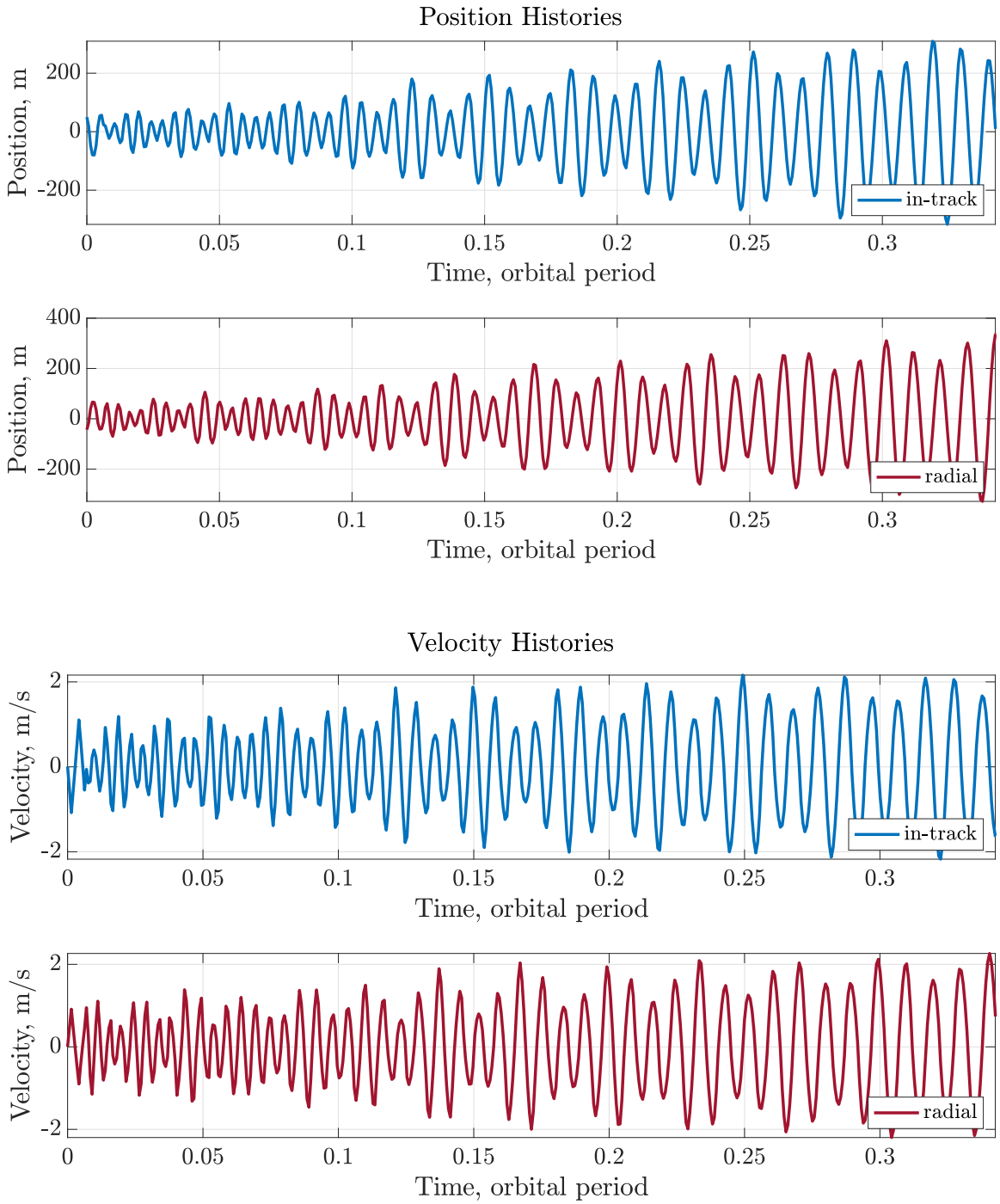

Figure 4.25. State histories with a strong attractive potential

computed. The longer computation times, around 0.75 seconds up to about 2.9 seconds, correspond to scenarios where obstacles are detected within the reach set. The reach sets computation duration is directly related to the number of obstacles

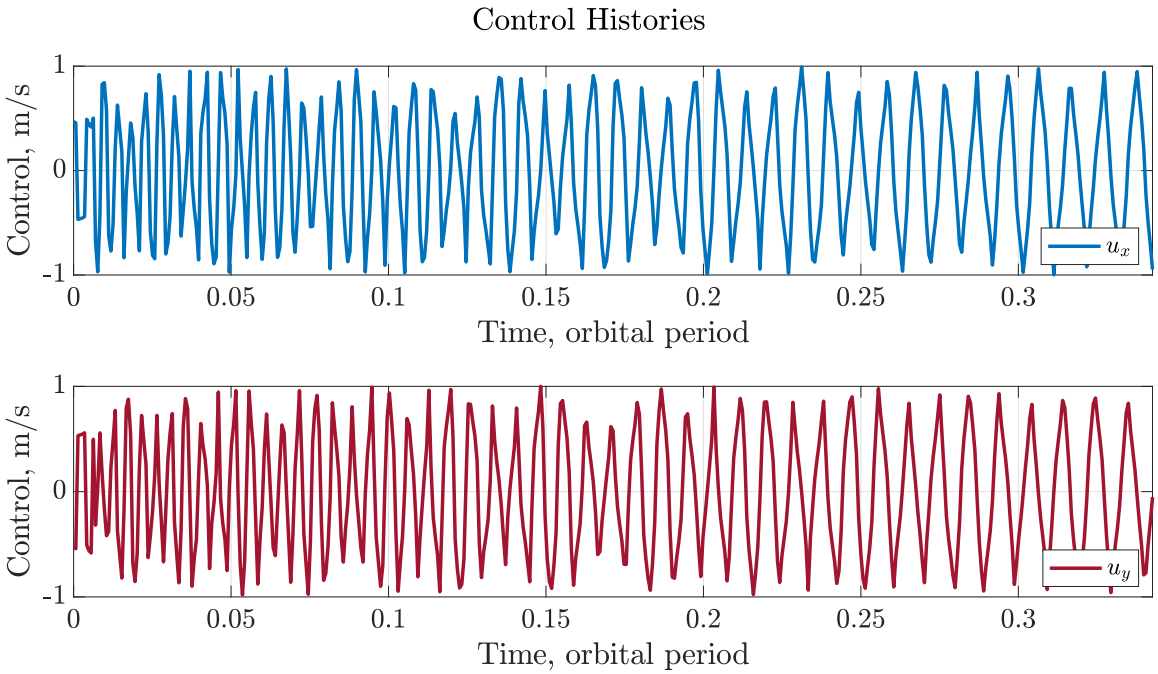

Figure 4.26. Control histories with a strong attractive potential

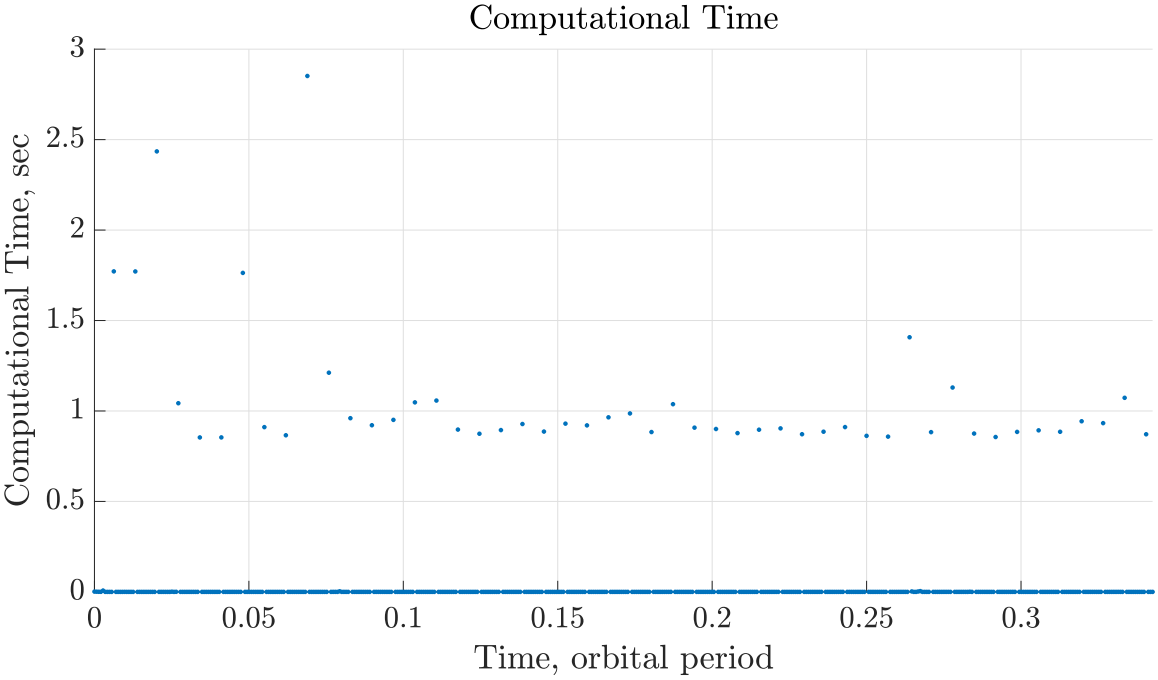

Figure 4.27. Computation time at each step with a strong attractive potential

found to be within the reach set.

This scenario demonstrates that performing reachability analysis, obstacle detec-

tion, and state propagation via APF together can be feasible given the time between computations remains longer than the computation time itself. However, while the APF in this scenario allows the deputy spacecraft to utilize its full control authority, the deputy is unable to rendezvous with the chief because its movements are too large and it bounces around the global minimum. This can be mitigated by decreasing the attractive potential by making the potential shape matrix $\boldsymbol{P}$ smaller, as shown in 4.2.3. Additionally, the duration between computations can be decreased so the deputy does not have to continually over-correct its previous move. In order to maintain the goal of being beneficial for on-board, autonomous guidance planning, this interval would remain longer than the time it takes the on-board hardware to perform the calculations. For the hardware used in this research, that period is approximately three seconds.

4.2.3 Case 2: Weak Attractive Potential Function

A weak attractive function is demonstrated in GEO. The deputy spacecraft is initialized in a NMC relative orbit 100 km from the chief spacecraft. The maneuver begins at $\beta = 30°$ in the NMC orbit with nine relatively static obstacles. The interval between trajectory calculations is 1 minute. The reach set is calculated every 10^{th} calculation, or every 10 minutes.

The shape of the attractive potential function is determined by the shaping matrix $\boldsymbol{P}$. Increasing the shape matrix $\boldsymbol{P}$ increases the height of the paraboloid, creating a large paraboloid with a steep gradient.

The attractive potential shape matrix $\boldsymbol{P}$ is

$$\boldsymbol{P} = \begin{bmatrix} 2 \times 10^{-2} & 0 \\ 0 & 2 \times 10^{-2} \end{bmatrix} \tag{4.2}$$

which creates a tall repulsive potential comparatively with respect to the attractive potential function, as shown in Figures 4.28.

The contour plot of the potential functions (second row of Figure 4.28) shows the obstacles are strongly represented by the repulsive function because the height of the repulsive function dominates the attractive potential function.

Figure 4.29 and 4.30 show the trajectory of the deputy spacecraft as it attempts to rendezvous with the chief spacecraft by following the gradient of the APF. The trajectory produced by the APF is validated by using the calculated controls with the forced NERMs, shown in Figure 4.29. The state and control histories are shown in Figures 4.30 and 4.31. The trajectory and state history plots show the spacecraft does rendezvous with the chief, however it takes two full periods. The control histories in Figure 4.31 show that these maneuvers require very small control input, often several orders of magnitude below the maximum allowable control input 1 m/s, or zero, to maneuver the spacecraft. A spike in control input occurs around 0.15 periods as the deputy spacecraft maneuvers itself around the obstacles and then back towards the chief spacecraft. Once around the obstacles, the spacecraft coasts the rest of the way to the target.

Computation time is documented in Figure 4.32. To evaluate the feasibility of computing reach sets and guidance planning together autonomously and in real-time, it is required that the maneuver be calculated prior to the required maneuver time. As mentioned, the trajectory and control is computed for every minute, therefore this algorithm must be able to compute the trajectory in under 1 minute, including when the reach sets are being calculated and the obstacles are being identified.

Figure 4.32 shows all computations are feasible, with zero calculations taking longer to compute than the required one minute. The short computation times are around 10-40 microseconds and correspond to scenarios where the reach set is not

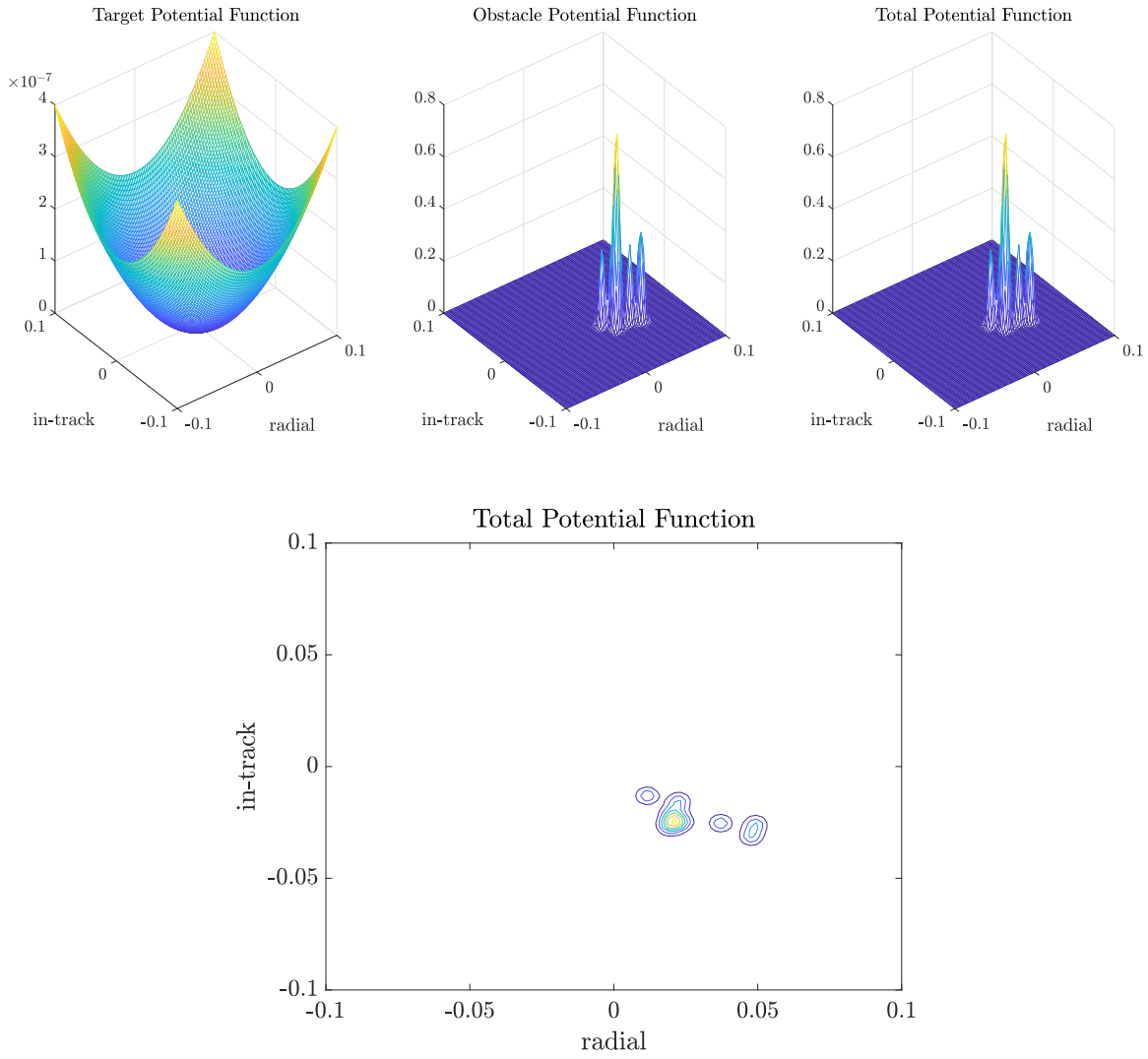

Figure 4.28. APF with a weak attractive potential

computed. The longer computation times, around 1.5 seconds up to about 2.9 seconds, correspond to scenarios where obstacles are detected within the reach set. The reach sets computation duration is directly related to the number of obstacles found to be within the reach set.

This scenario further demonstrates that performing reachability analysis, obstacle detection, and state propagation via APF together can be feasible given the time between computations remains longer than the computation time itself. However, the APF in this scenario makes the deputy expend very little control authority, thus

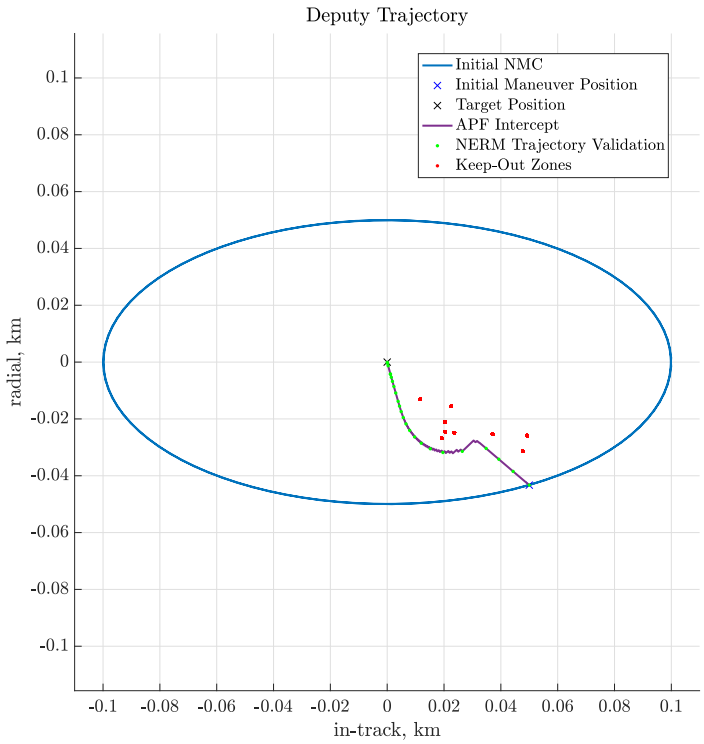

Figure 4.29. Trajectory with a weak attractive potential

it takes a very long time to reach the target. This can be mitigated by increasing the attractive potential by making the potential shape matrix $\boldsymbol{P}$ larger. Additionally, applying different potential functions or a different method of computing the continuous feedback control law, such as those developed by others and referenced in Section 2.2.3, may help improve the maneuver performance.

Lastly, because computation time is directly related to the number of obstacles found within the reach set, a deputy maneuvering through many obstacles will be limited to the frequency at which it performs its reachability analysis, obstacle detection, and state propagation compared to a scenario with fewer obstacles. Longer times between computations may result in missing the detection of an obstacle and colliding with it. If the deputy gets very near an obstacle before the next computation, it may be in a position that has a high potential from the repulsive function

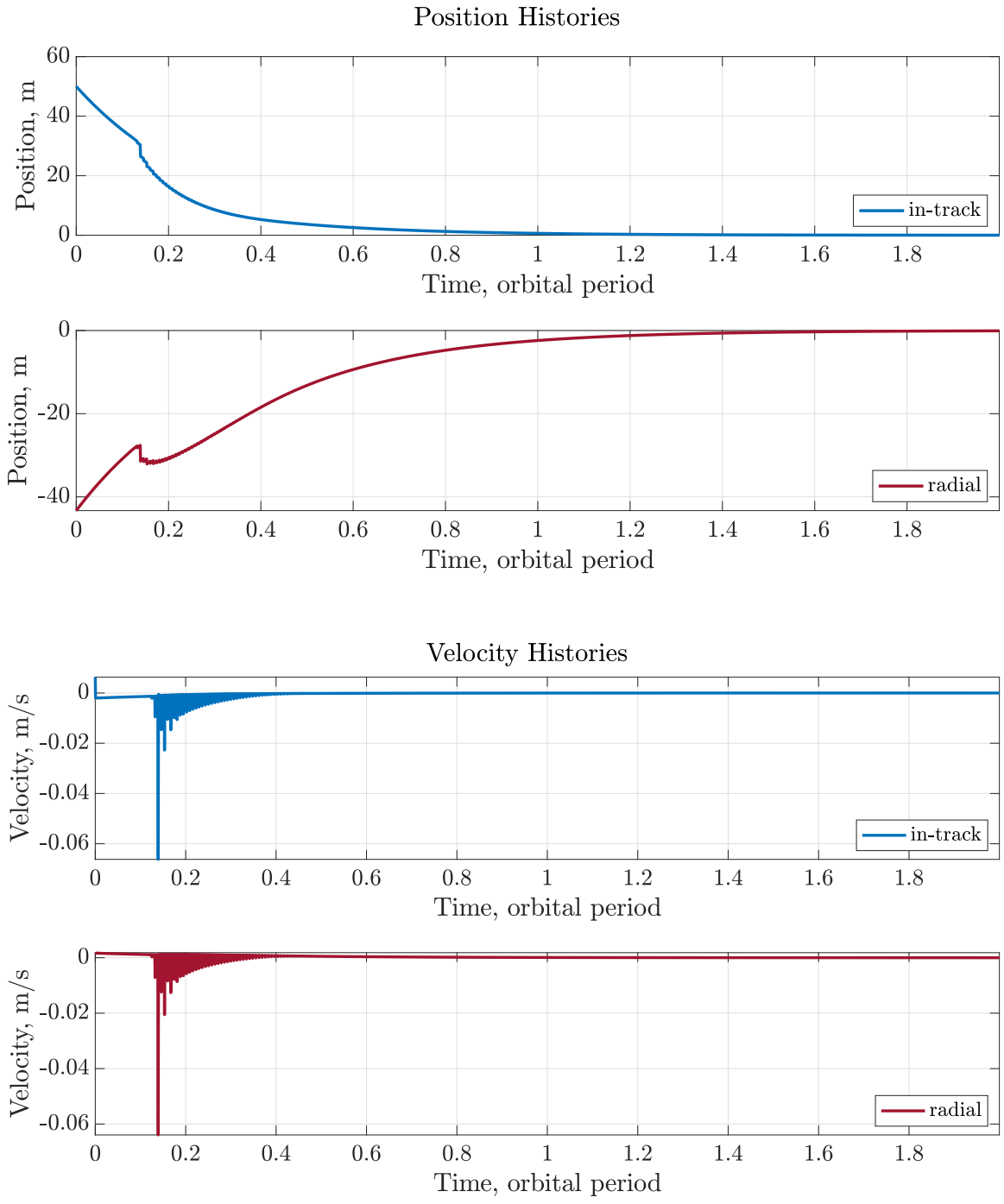

Figure 4.30. State histories with a weak attractive potential

which would veer the deputy far off course and delay or eliminate the possibility of rendezvous.

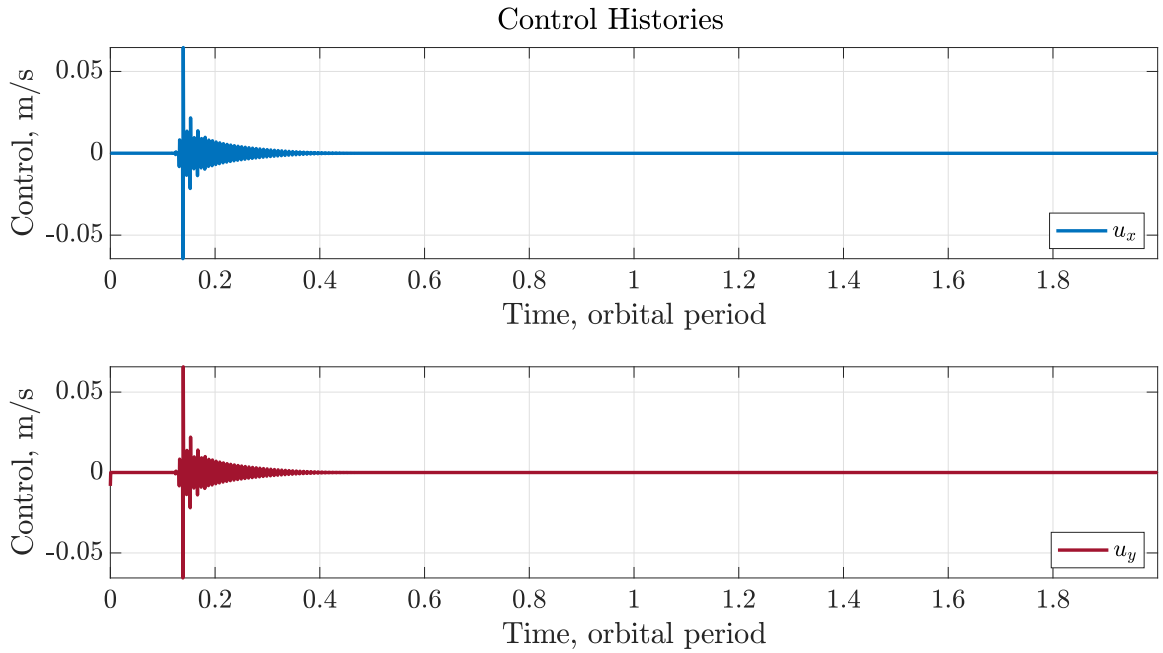

Figure 4.31. Control histories with a weak attractive potential

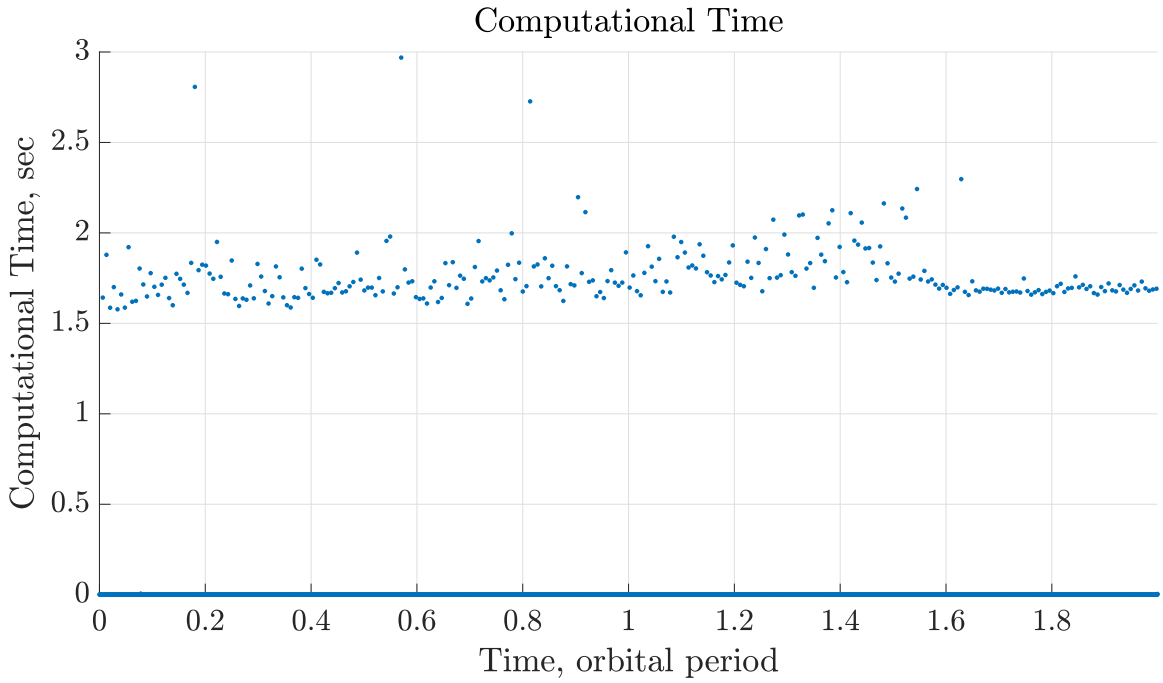

Figure 4.32. Computation time at each step with a weak attractive potential

4.2.4 Case 3: Obstacles moving on an NMC orbit

Figures 4.33 and 4.34 show failed trajectories of the deputy as it attempts to rendezvous with the chief while avoiding obstacles moving in their own NMC orbits.

Both figures show the deputy performing the rendezvous maneuver and Figure 4.34 initially shows successful avoidance of obstacles as they pass through the deputy's path toward the chief. However, both cases then show the deputy's trajectory shoot far off course due to its proximity to the obstacles. This scenario occurs because the time interval between calculations is too large to maintain sufficient collision avoidance. When the trajectories significantly veer off course, this is a result of the deputy being too close to the obstacle, and thus in an area of high potential. This is undesirable because, in a real-world scenario, this may result in a collision, near-collision, or a failed rendezvous operation.

This scenario demonstrates the significance of the time interval at which the trajectory and reach sets are computed, especially in dynamic environments. Rapid computations are necessary to enable early detection of obstacles and finer control of the deputy as it performs its rendezvous procedure.

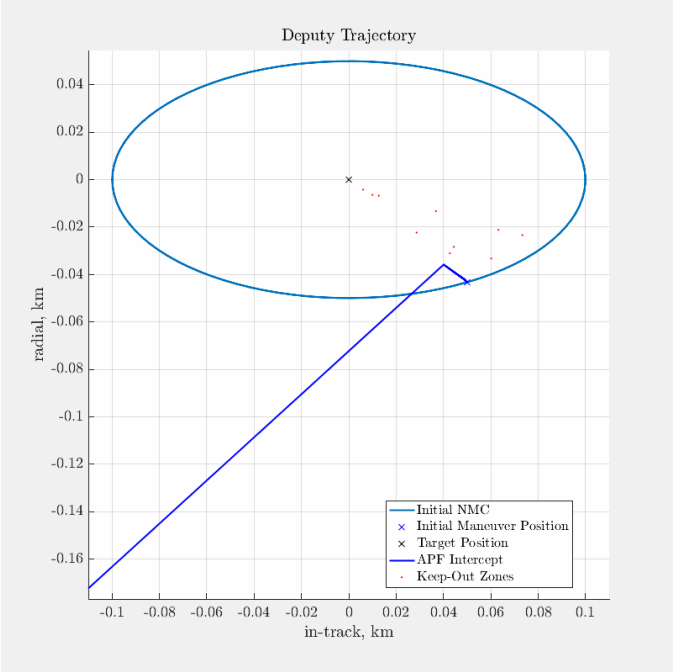

Figure 4.33. RPO attempt with 10 obstacles in NMC orbits; (10 min interval)

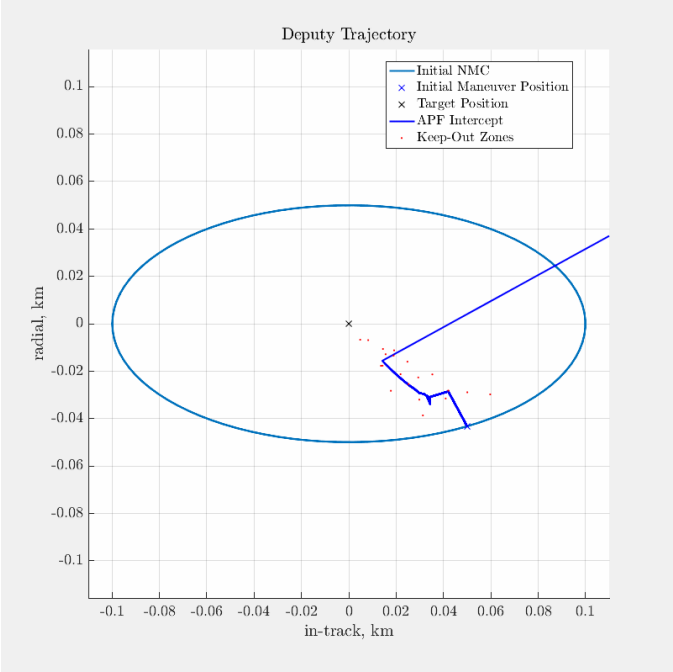

Figure 4.34. RPO attempt with 20 obstacles in NMC orbits; (60 min interval)

V. Conclusions and Recommendations

5.1 Conclusions

This research explores leveraging reachability analysis to enable a computationally efficient method for verifying object detection and control verification for guidance planning in spacecraft RPO applications. Two problems were created to address three research questions. First, several relative motion models were used to compute approximate ellipsoidal reachable sets across a range of orbit configurations. Then, ellipsoidal reachability analysis was combined with an APF controller to compute the reach set of a given state, identify obstacles within that reach set, and propagate the state towards the target location while avoiding the obstacles. The results from both problems were analyzed for feasibility on-board and in real-time, and for accuracy in providing verification of object detection and control verification for guidance planning.

The size, shape, and orientation of the CW and SS models' reach set at LEO is shown to be not suitable for elliptical orbits, but they may be sufficient over extremely short time horizons. The CW and SS models are both feasible for circular orbits, but both under-estimate the reach set at higher eccentricities and are therefore unable to encompass all possible final states and ensure collision avoidance of all reachable obstacles. The YA and GA models are shown to provide very similar reach sets across the eccentricities tested. Furthermore, computation times for calculating the reach sets are demonstrated to have strong potential for on-board, real-time guidance application. At GEO, all models produce reach sets that are suitable for all eccentricities given that the time horizons where the reach sets deviate significantly are likely beyond the necessary computation requirement.

The reach/APF algorithm show it is feasible to combine reachability analysis

and an APF controller in a computationally efficient method for on-board, real-time safe guidance planning. The APF controller is shown to be extremely sensitive to the number of obstacles, potential function tuning parameters, time horizon between computations, maneuver duration constraint, and the maximum allowable computation time constraint. However, the analytical nature of both ellipsoidal reach set approximation and APFs enable rapid computation that is promising for on-board, real-time implementation.

5.2 Recommendations for Future Work

5.2.1 Tuning via Linear Regression

Tuning the APF proved to be a challenging task. The number of obstacles, time horizon between computations, size of the attractive potential, available control authority, and maximum allowable computation time constraints make it difficult to find the right combination of parameters to guide the deputy to the chief within required mission constraints. Linear regression, gradient descent algorithms, or other machine learning techniques may be useful for determining the best combination of the many parameters available for tuning.

5.2.2 Potential Functions and Control Laws

The parabolic attractive potential implemented in this research was responsible for the variable control input based on the distance from the chief spacecraft. Other potential functions, such as a hyperboloid, as demonstrated in [54], may simplify the tuning of the attractive potential. A hyperboloid or similar function may also allow for steadier control throughout the maneuver.

Additionally, other control laws, such as those developed by Muñoz, Fields, and McCamish, may provide an improved controller based on spacecraft constraints like

its relative velocity [55, 49, 43].

5.2.3 Parallelization

The reachability analysis portion of the reach/APF controller is well suited for parallelization. At each step, a computer can be performing parallel operations to check all the obstacles for their proximity to the reach set. This can be especially beneficial for scenarios with many obstacles or those requiring rapid maneuvering, and by extension, a rapid time horizon for reach/APF computation. The parallel computing could drastically reduce the computation time at each step, further improving the feasibility of this approach for safe, on-board, autonomous mission planning.

Bibliography

1. Schaub, H., "Spacecraft relative orbit geometry description through orbit element differences," *14th US National Congress of Theoretical and Applied Mechanics, Blacksburg, VA*, 2002.

2. Lovell, T. A., Tragesser, S., and Tollefson, M., "A Practical Guidance Methodology for Relative Motion of LEO Spacecraft Based on the Clohessy-Wiltshire Equations," *American Astronautical Society*, , No. 04-252, 2004.

3. Chen, M., *High Dimensional Reachability Analysis: Addressing the Curse of Dimensionality in Formal Verification*, Ph.D. thesis, EECS Department, University of California, Berkeley, Jul 2017.

4. Woffinden, D., Geller, D., Mosher, T., and Kwong, J., "On-Orbit Satellite Rendezvous Inspection: A Concept Study and Design," *Spaceflight Mechanics 2005. Advances in the Astronautical Sciences*, 2005, pp. 849–867.

5. Lovell, T. A. and Spencer, D. A., "Relative Orbital Elements Formulation Based upon the Clohessy-Wiltshire Equations," *The Journal of the Astronautical Sciences*, Vol. 61, No. 4, 2014, pp. 341–366.

6. Polites, M., "An Assessment of the Technology of Automated Rendezvous and Capture in Space," *NASA Technical Papers*, Vol. NASA/TP-1998-208528, July 1998.

7. Butikov, E. I., "Orbital maneuvers and space rendezvous," *Advances in Space Research*, Vol. 56, No. 11, 2015, pp. 2582 – 2594.

8. Jewison, C. M., *Guidance and Control for Multi-stage Rendezvous and Docking Operations in the Presence of Uncertainty*, Ph.D. thesis, Massachusetts Institute of Technology, June 2017.

9. Lovell, T. A. and Tragesser, S., *Guidance for Relative Motion of Low Earth Orbit Spacecraft Based on Relative Orbit Elements*, 2004.

10. Zagaris, C., *Autonomous Spacecraft Rendezvous with a Tumbling Object: Applied Reachability Analysis and Guidance and Control Strategies*, Ph.D. thesis, Naval Postgraduate School, 2018.

11. Alfriend, K. T., Vadali, S. R., Gurfil, P., How, J. P., and Breger, L. S., "Chapter 2 - Fundamental Astrodynamics," *Spacecraft Formation Flying*, edited by K. T. Alfriend, S. R. Vadali, P. Gurfil, J. P. How, and L. S. Breger, Butterworth-Heinemann, Oxford, 2010, pp. 13 – 15.

12. Clohessy, W. and Wiltshire, R., "Terminal guidance system for satellite rendezvous," *Journal of the Aerospace Sciences*, Vol. 27, No. 9, 1960, pp. 653–658.

13. Alfriend, K. T., Vadali, S. R., Gurfil, P., How, J. P., and Breger, L. S., "Chapter 4 - Nonlinear Models of Relative Dynamics," *Spacecraft Formation Flying*, edited by K. T. Alfriend, S. R. Vadali, P. Gurfil, J. P. How, and L. S. Breger, Butterworth-Heinemann, Oxford, 2010, pp. 59 – 82.

14. Sullivan, J., Grimberg, S., and D'Amico, S., "Comprehensive Survey and Assessment of Spacecraft Relative Motion Dynamics Models," *Journal of Guidance, Control, and Dynamics*, Vol. 40, No. 8, 2017, pp. 1837–1859.

15. Schweighart, S. A. and Sedwick, R. J., "High-Fidelity Linearized J Model for Satellite Formation Flight," *Journal of Guidance, Control, and Dynamics*, Vol. 25, No. 6, 2002, pp. 1073–1080.

16. Yamanaka, K. and Ankersen, F., "New State Transition Matrix for Relative Motion on an Arbitrary Elliptical Orbit," *Journal of Guidance, Control, and Dynamics*, Vol. 25, No. 1, 2002, pp. 60–66.

17. Gim, D.-W. and Alfriend, K. T., "State Transition Matrix of Relative Motion for the Perturbed Noncircular Reference Orbit," *Journal of Guidance, Control, and Dynamics*, Vol. 26, No. 6, 2003, pp. 956–971.

18. Sherrill, R. E., Sinclair, A. J., and Lovell, T. A., "Virtual-Chief Generalization of Hill–Clohessy–Wiltshire to Elliptic Orbits," *Journal of Guidance, Control, and Dynamics*, Vol. 38, No. 3, 2015, pp. 523–528.

19. Chamberlin, J. A. and Rose, J. T., "Gemini rendezvous program," *Journal of Spacecraft and Rockets*, Vol. 1, No. 1, 1964, pp. 13–18.

20. Goodman, J. L., "History of Space Shuttle Rendezvous and Proximity Operations," *Journal of Spacecraft and Rockets*, Vol. 43, No. 5, 2006, pp. 944–959.

21. Cruzen, C., Lomas, J. J., and Dabney, R. W., "Test results for the automated rendezvous and capture system," *23nd Annual AAS Guidance and Control Conference, Breckenridge, CO*, 2000.

22. George, C. B., *Optimal and Robust Neural Network Controllers for Proximal Spacecraft Maneuvers*, Master's thesis, Air Force Institute of Technology, 2019.

23. Alfriend, K. T., Vadali, S. R., Gurfil, P., How, J. P., and Breger, L. S., "Chapter 5 - Linear Equations of Relative Motion," *Spacecraft Formation Flying*, edited by K. T. Alfriend, S. R. Vadali, P. Gurfil, J. P. How, and L. S. Breger, Butterworth-Heinemann, Oxford, 2010, pp. 83 – 121.

24. Schweighart, S. and Sedwick, R., "A perturbative analysis of geopotential disturbances for satellite cluster formation flying," *2001 IEEE Aerospace Conference Proceedings (Cat. No.01TH8542)*, Vol. 2, 2001, pp. 2/1001–2/1019 vol.2.

25. Yamada, K., Shima, T., and Yoshikawa, S., "Effect of J2 Perturbations on Relative Spacecraft Position in Near-Circular Orbits," *Journal of Guidance, Control, and Dynamics*, Vol. 33, No. 2, 2010, pp. 584–590.

26. Tschauner, J. and Hempel, P., "Rendezvous zu einem in elliptischer Bahn umlaufenden Ziel," *Astronautica Acta*, Vol. 11, No. 2, 1965, pp. 104–+.

27. Sinclair, A. J., Sherrill, R. E., and Lovell, T. A., "Geometric interpretation of the Tschauner–Hempel solutions for satellite relative motion," *Advances in Space Research*, Vol. 55, No. 9, 2015, pp. 2268 – 2279.

28. Willis, M., Lovell, A., and D'Amico, S., "Second-Order Analytical Solution for Relative Motion on Arbitrarily Eccentric Orbits," *AIAA/AAS Space Flight Mechanics Meeting, Ka'anapali, Maui, HI*, 2019.

29. Hess, J. A., *Osculating Relative Orbit Elements Resulting from Chief Eccentricity and J2 Perturbing Forces*, Master's thesis, 2011.

30. Di Mauro, G., Lawn, M., and Bevilacqua, R., "Survey on Guidance Navigation and Control Requirements for Spacecraft Formation-Flying Missions," *Journal of Guidance, Control, and Dynamics*, Vol. 41, No. 3, 2018, pp. 581–602.

31. Alfriend, K. T., Vadali, S. R., Gurfil, P., How, J. P., and Breger, L. S., "Chapter 1 - Introduction," *Spacecraft Formation Flying*, edited by K. T. Alfriend, S. R. Vadali, P. Gurfil, J. P. How, and L. S. Breger, Butterworth-Heinemann, Oxford, 2010, pp. 1 – 11.

32. Hohmann, W., *Die Erreichbarkeit der Himmelskörper (The Attainability of Celestial Bodies)*, R. Oldenbourg, 1925.

33. Wiesel, W. E., *Spaceflight Dynamics: Third Edition*, Createspace, 2020.

34. Wen, C., Zhao, Y., Li, B., and Shi, P., "Solving the relative Lambert's problem and accounting for its singularities," *Acta Astronautica*, Vol. 97, 2014, pp. 122–129.

35. Kelly, M., "An introduction to trajectory optimization: How to do your own direct collocation," *SIAM Review*, Vol. 59, No. 4, 2017, pp. 849–904.

36. Walsh, M. T. and Peck, M. A., "Survey of Methods for Calculating Impulsive ΔV-Minimizing Orbit Transfer Maneuvers," *AIAA Scitech 2020 Forum*.

37. Lawden, D. F., "Minimal Rocket Trajectories," *Journal of the American Rocket Society*, Vol. 23, No. 6, 1953, pp. 360–367.

38. Prussing, J. E., *Optimal multiple-impulse orbital rendezvous.*, Ph.D. thesis, Massachusetts Institute of Technology, 1967.

39. Palmer, P., "Optimal Relocation of Satellites Flying in Near-Circular-Orbit Formations," *Journal of Guidance, Control, and Dynamics*, Vol. 29, No. 3, 2006, pp. 519–526.

40. Ortolano, N. G., *Autonomous Trajectory Planning for Satellite RPO and Safety of Flight Using Convex Optimization*, Ph.D. thesis, Utah State University, 2018.

41. David Johnathan Irvin, J., *Optimal Control Strategies for Constrained Relative Orbits*, Ph.D. thesis, Air Force Institute of Technology, 2007.

42. Ogata, K., *Modern Control Engineering*, Pearson, USA, 5th ed., 2009.

43. McCamish, S. B., "Distributed autonomous control of multiple spacecraft during close proximity operations," 2007.

44. Beatty, S., "Comparison of PD and LQR Methods for Spacecraft Attitude Control Using Star Trackers," *2006 World Automation Congress*, 2006, pp. 1–6.

45. Bevilacqua, R., Lehmann, T., and Romano, M., "Development and experimentation of LQR/APF guidance and control for autonomous proximity maneuvers of multiple spacecraft," *Acta Astronautica*, Vol. 68, No. 7, 2011, pp. 1260 – 1275.

46. Guarnaccia, L., Bevilacqua, R., and Pastorelli, S. P., "Suboptimal LQR-based spacecraft full motion control: Theory and experimentation," *Acta Astronautica*, Vol. 122, 2016, pp. 114 – 136.

47. Khatib, O., "Real-time obstacle avoidance for manipulators and mobile robots," *Proceedings. 1985 IEEE International Conference on Robotics and Automation*, Vol. 2, 1985, pp. 500–505.

48. Zappulla, Richard Salvatore, I., "Experimental evaluation methodology for spacecraft proximity maneuvers in a dynamic environment," 2017.

49. Fields, A. R., *Continuous Control Artificial Potential Function Methods and Optimal Control*, Master's thesis, Air Force Institute of Technology, 2014.

50. Lopez, I. and Mclnnes, C. R., "Autonomous rendezvous using artificial potential function guidance," *Journal of Guidance, Control, and Dynamics*, Vol. 18, No. 2, 1995, pp. 237–241.

51. Newman, W. and Hogan, N., "High speed robot control and obstacle avoidance using dynamic potential functions," *Proceedings. 1987 IEEE International Conference on Robotics and Automation*, Vol. 4, 1987, pp. 14–24.

52. Vadakkepat, P., Kay Chen Tan, and Wang Ming-Liang, "Evolutionary artificial potential fields and their application in real time robot path planning," *Proceedings of the 2000 Congress on Evolutionary Computation. CEC00 (Cat. No.00TH8512)*, Vol. 1, 2000, pp. 256–263 vol.1.

53. Ahsun, U. and Miller, D. W., "Dynamics and control of electromagnetic satellite formations," *2006 American Control Conference*, 2006, pp. 6 pp.–.

54. Badawy, A. and McInnes, C. R., "Robot motion planning using hyperboloid potential functions," *World Congress on Engineering 2007*, 2007.

55. Munoz, J. D., *Rapid path-planning algorithms for autonomous proximity operations of satellites*, Ph.D. thesis, University of Florida, Jan. 2011.

56. Maler, O., "Computing Reachable Sets : An Introduction," 2008.

57. Holzinger, M. and Scheeres, D., "Reachability Analysis Applied to Space Situational Awareness," 09 2009, pp. 11.

58. Mitchell, I. M., Bayen, A. M., and Tomlin, C. J., "A time-dependent Hamilton-Jacobi formulation of reachable sets for continuous dynamic games," *IEEE Transactions on Automatic Control*, Vol. 50, No. 7, 2005, pp. 947–957.

59. Bajcsy, A., Bansal, S., Bronstein, E., Tolani, V., and Tomlin, C. J., "An Efficient Reachability-Based Framework for Provably Safe Autonomous Navigation in Unknown Environments," 2019.

60. Devonport, A., Khaled, M., Arcak, M., and Zamani, M., "PIRK: Scalable Interval Reachability Analysis for High-Dimensional Nonlinear Systems," 2020.

61. Kurzhanskiy, A. A. and Varaiya, P., *Ellipsoidal Toolbox Manual*, 2006-2008.

62. Greenstreet, M. R. and Mitchell, I., "Reachability Analysis Using Polygonal Projections," *Hybrid Systems: Computation and Control*, edited by F. W. Vaandrager and J. H. van Schuppen, Springer Berlin Heidelberg, Berlin, Heidelberg, 1999, pp. 103–116.

63. Bajcsy, A., Bansal, S., Bronstein, E., Tolani, V., and Tomlin, C., "An Efficient Reachability-Based Framework for Provably Safe Autonomous Navigation in Unknown Environments," 05 2019.

64. Herbert, S. L., Ghosh, S., Bansal, S., and Tomlin, C. J., "Reachability-Based Safety Guarantees using Efficient Initializations," 2019.

65. Jiang, F., Chou, G., Chen, M., and Tomlin, C. J., "Using Neural Networks to Compute Approximate and Guaranteed Feasible Hamilton-Jacobi-Bellman PDE Solutions," 2017.

66. Li, A., Sun, L., Zhan, W., Tomizuka, M., and Chen, M., "Prediction-Based Reachability for Collision Avoidance in Autonomous Driving," 2020.

67. Chen, M., Hu, Q., Fisac, J. F., Akametalu, K., Mackin, C., and Tomlin, C. J., "Reachability-Based Safety and Goal Satisfaction of Unmanned Aerial Platoons on Air Highways," *Journal of Guidance, Control, and Dynamics*, Vol. 40, No. 6, 2017, pp. 1360–1373.

68. Aguilar Marsillach, D. and Holzinger, M. J., "Spacecraft Custody Maintenance and Maneuver Detection Using Robotic Telescopes and Reachable Sets," *Journal of Guidance, Control, and Dynamics*, Vol. 0, No. 0, 0, pp. 1–17.

69. Allen, R. E., Clark, A. A., Starek, J. A., and Pavone, M., "A machine learning approach for real-time reachability analysis," *2014 IEEE/RSJ International Conference on Intelligent Robots and Systems*, 2014, pp. 2202–2208.

70. Holzinger, M. and Scheeres, D., *Applied Reachability for Space Situational Awareness and Safety in Spacecraft Proximity Operations*.

71. Zagaris, C. and Romano, M., "Reachability Analysis of Planar Spacecraft Docking with Rotating Body in Close Proximity," *Journal of Guidance, Control, and Dynamics*, Vol. 41, No. 6, 2018, pp. 1416–1422.

72. Zagaris, C. and Romano, M., *Applied Reachability Analysis for Spacecraft Rendezvous and Docking with a Tumbling Object*.

73. Lesser, K., Oishi, M., and Erwin, R. S., "Stochastic reachability for control of spacecraft relative motion," *52nd IEEE Conference on Decision and Control*, 2013, pp. 4705–4712.

74. Zagaris, C. and Hess, J. A., "Rapid Reachability Analysis of Single Impulse Spacecraft Relative Motion Maneuvers," No. 20-468, 2020.

75. Kurzhanski, A. B., "Ellipsoidal Calculus for Estimation and Feedback Control," *Systems and Control in the Twenty-First Century*, edited by C. I. Byrnes, B. N. Datta, C. F. Martin, and D. S. Gilliam, Birkhäuser Boston, Boston, MA, 1997, pp. 229–243.

REPORT DOCUMENTATION PAGE

Form Approved
OMB No. 0704–0188

1. REPORT DATE *(DD–MM–YYYY)*	2. REPORT TYPE	3. DATES COVERED *(From — To)*
25–03–2021	Master's Thesis	Sep 2019 — Mar 2021

4. TITLE AND SUBTITLE

Safe Spacecraft Rendezvous and Proximity Operations via Reachability Analysis

5a. CONTRACT NUMBER

5b. GRANT NUMBER

5c. PROGRAM ELEMENT NUMBER

6. AUTHOR(S)

Grossi, Paul A., Capt, USSF

5d. PROJECT NUMBER

5e. TASK NUMBER

5f. WORK UNIT NUMBER

7. PERFORMING ORGANIZATION NAME(S) AND ADDRESS(ES)

Air Force Institute of Technology
Graduate School of Engineering and Management (AFIT/EN)
2950 Hobson Way
WPAFB OH 45433-7765

8. PERFORMING ORGANIZATION REPORT NUMBER

AFIT-ENY-MS-21-M-302

9. SPONSORING / MONITORING AGENCY NAME(S) AND ADDRESS(ES)

Intentionally Left Blank

10. SPONSOR/MONITOR'S ACRONYM(S)

11. SPONSOR/MONITOR'S REPORT NUMBER(S)

12. DISTRIBUTION / AVAILABILITY STATEMENT

Approval for public release; distribution is unlimited.

13. SUPPLEMENTARY NOTES

14. ABSTRACT

The rapid expansion of the utilization of space by nations and industry has presented new challenges and opportunities to operate efficiently and responsibly. Reachability analysis is the process of computing the set of states that can be reached given all admissible controls and can be a valuable component in an autonomous mission planning system if conducted efficiently. In the current research, reachability analysis is used with several relative motion models to show that all ranges of orbits can be computed in milliseconds, and that it is a feasible approach for on-board autonomous mission planning. Reachability analysis is then combined with an Artificial Potential Function (APF) derived guidance control law to conduct safe spacecraft rendezvous between a deputy in a Natural Motion Circumnavigation (NMC) relative orbit around a chief while avoiding obstacles. While the APF employed in this research requires improvements for trajectory computation, this research demonstrates the feasibility of combining reachability analysis with an APF for safe, on-board, autonomous mission planning.

15. SUBJECT TERMS

rendezvous and proximity operations, reachability analysis, artificial potential functions, relative motion models

16. SECURITY CLASSIFICATION OF:			17. LIMITATION OF ABSTRACT	18. NUMBER OF PAGES	19a. NAME OF RESPONSIBLE PERSON
a. REPORT	b. ABSTRACT	c. THIS PAGE			Maj Costantinos Zagaris, AFIT/ENY
U	U	U	UU	109	19b. TELEPHONE NUMBER *(include area code)* (937) 255-3636, x4774; costantinos.zagaris@afit.edu